

SEARCH FOR SUPERSYMMETRY WITH
B-QUARK JETS AND MISSING TRANSVERSE
ENERGY IN PP COLLISIONS AT $\sqrt{s} = 7$ TEV

A Dissertation

Presented to the Faculty of the Graduate School
of Cornell University

in Partial Fulfillment of the Requirements for the Degree of
Doctor of Philosophy

by

Wee Don Teo

January 2013

© 2013 Wee Don Teo
ALL RIGHTS RESERVED

SEARCH FOR SUPERSYMMETRY WITH B-QUARK JETS AND MISSING
TRANSVERSE ENERGY IN PP COLLISIONS AT $\sqrt{s} = 7$ TEV

Wee Don Teo, Ph.D.

Cornell University 2013

We present a search for supersymmetry in events with large E_T^{miss} , no leptons, at least three jets, and one or more b -quark jets. We use a data sample corresponding to 4.98 fb^{-1} of proton-proton collisions at $\sqrt{s} = 7$ TeV collected by the CMS experiment in 2011. The primary sources of standard model background are evaluated using data-driven techniques. We find good agreement between the data and the sum of the background predictions. The results are used to constrain the cross sections for the production of b -quark-enriched final states in the context of supersymmetric models.

BIOGRAPHICAL SKETCH

Teo Wee Don was born in Kuala Lumpur, Malaysia in 1984. He moved to Toronto, Canada with his family in the spring of 1988 and spent the next 19 years in the Ontario capital. He graduated from Sir John A. MacDonald Collegiate Institute in 2002 and from the University of Toronto in 2007, majoring in physics and mathematics. He started graduate school at Cornell in the fall of 2007 and has lived in Ithaca, with occasional extended stays in Saint Genis-Pouilly, France (near CERN) over the past $5\frac{1}{2}$ years.

The choice to pursue an education in physics was always a natural one for Don. His strong interest in the fundamental understanding of nature led him to the field of particle physics. Moreover, his time spent on the CDF and T2K experiments during his undergraduate years helped to fuel his interest in experimental physics and data analysis. He has spent his graduate career working as part of the CMS collaboration, where he has been involved in the data quality monitoring of the trigger system, the measurement of the top-quark pair production cross section, and the search for new physics. He feels very fortunate to have worked on this historic experiment with so many dedicated scientists.

After graduation, he intends to apply the practical skills and knowledge he has gained from his studies to tackle global issues in the energy and environmental sector.

To my family.

ACKNOWLEDGEMENTS

I owe a tremendous debt of gratitude to the many people who have shaped my graduate career. I am especially thankful to my advisor, Peter Wittich, for being a wonderful mentor and for always offering his time and support. I am grateful as well to my other committee members, Anders Ryd and Maxim Perelstein, from whom I have learned much throughout my graduate studies.

I thank Lorenzo Agostino for introducing me to the CMS detector, the world of data quality monitoring and triggering, and the CMS software framework. I would also like to thank Jorge Trocóniz for his guidance on the DTFD DQM project, and Hwidong Yoo and Jean-Roch Vlimant for their support during our time on the muon HLT DQM software.

I am very grateful to the members of the SMT gang - Ken Bloom, Helena Malbouisson, Tuula Mäki, Jason Keller, Maxwell Gregoire, Jeff Temple, and Aaron Dominguez - for the wonderful experience on my first CMS analysis. I thank Ken especially for being an excellent mentor and group leader.

My deepest gratitude goes to the entire RA2b group for all their hard work and creativity in bringing to fruition the analysis presented in this thesis. I thank in particular Sezen Sekmen for sharing the load on our trigger work, Keith Ulmer and Alessandro Gaz for their tireless efforts and their patience in answering all my questions, Owen Long for his invaluable creativity, and Bill Gary, Bill Ford, Jim Smith, Harrison Prosper, and Jeff Richman for their insight and leadership. I am especially indebted to the Cornell RA2b members - Julia Thom, Anders Ryd, Peter Wittich, fellow students Ben Kreis and Gala Kaufman, and post-docs Josh Thompson and Luke Winstrom - for the countless discussions and for their immense contributions to this analysis. I am particularly grateful to Josh for being, in my opinion, the backbone of our analysis group and a

tremendous mentor to me.

I want to extend my appreciation to the rest of the Cornell CMS group for the extremely enriching experience during my time here. It has been a great joy to be a part of such a kind and knowledgeable group of people.

No analysis would be possible without the unimaginable amount of work put into the design, construction, and operation of the LHC accelerator and CMS experiment. My humble thanks to the countless people who have been involved over the past several decades in this historic achievement .

Finally, I owe everything to my family and friends for sharing with me their love, laughter, and support. To my parents, Teng Teo and Kwee Choo Lee, to my brother Jerry, and to Vanessa - I am extremely fortunate to have you.

TABLE OF CONTENTS

Biographical Sketch	iii
Dedication	iv
Acknowledgements	v
Table of Contents	vii
List of Tables	x
List of Figures	xiv
1 Introduction	1
2 Physics beyond the standard model	3
2.1 The standard model	4
2.2 Beyond the standard model	7
2.2.1 The TeV scale	8
2.2.2 Supersymmetry	9
2.2.3 The Minimal Supersymmetric Standard Model	12
2.2.4 Natural SUSY	18
2.2.5 Gluino and squark production	19
2.2.6 Simplified model spectra	21
3 Accelerator and Detector	24
3.1 The Large Hadron Collider	24
3.2 The Compact Muon Solenoid Detector	28
3.2.1 Solenoid magnet	30
3.2.2 Tracker systems	30
3.2.3 Calorimeter systems	33
3.2.4 Muon systems	41
3.2.5 Trigger and DAQ system	44
4 Event Reconstruction	48
4.1 Tracks and vertices	48
4.1.1 Tracks	48
4.1.2 Vertices	50
4.2 Muons	51
4.3 Electrons	53
4.4 Particle-flow reconstruction	55
4.5 Jets	56
4.6 E_T^{miss}	58
4.7 b jet identification	58

5	Search for supersymmetry in events with b-quark jets and E_T^{miss}	63
5.1	Introduction	63
5.2	Data and Monte Carlo samples	65
5.3	Event selection	70
5.3.1	Selection regions and nomenclature	73
5.3.2	Suppressing SM background with b jets	74
5.4	Trigger efficiency	77
5.5	QCD background	80
5.5.1	Construction of $\Delta\hat{\phi}_{\text{min}}$ variable	80
5.5.2	QCD-background method	85
5.5.3	QCD control samples	85
5.5.4	Closure test of QCD prediction	87
5.5.5	QCD prediction results	89
5.5.6	Systematic uncertainties on QCD prediction	91
5.6	$Z \rightarrow \nu\bar{\nu}$ background	93
5.6.1	$Z \rightarrow \nu\bar{\nu}$ control sample	93
5.6.2	Acceptance and efficiencies	94
5.6.3	b jet extrapolation factor	98
5.6.4	$Z \rightarrow l^+l^-$ purity	100
5.6.5	$Z \rightarrow \nu\bar{\nu}$ background method	102
5.6.6	Closure test of $Z \rightarrow \nu\bar{\nu}$ prediction	103
5.6.7	Systematic uncertainties on $Z \rightarrow \nu\bar{\nu}$ prediction	105
5.6.8	$Z \rightarrow \nu\bar{\nu}$ prediction results	107
5.7	Top and W +jets background	112
5.7.1	top + W control sample	114
5.7.2	Closure test of top + W prediction	115
5.7.3	Systematic uncertainties on top + W prediction	117
5.7.4	top + W prediction results	119
5.8	Results and interpretation	121
5.8.1	Summary of background estimates	121
5.8.2	Signal efficiency	122
5.8.3	Global likelihood	132
5.8.4	Hypothesis testing	135
5.8.5	Likelihood results	137
5.8.6	Event display of highest- E_T^{miss} 3B event	143
6	Conclusion	145
A	Dataset, Trigger, and Event Selection details	146
A.1	List of datasets	146
A.2	List of triggers	146
A.3	Systematic uncertainty on trigger efficiency	149
A.4	Anomalous E_T^{miss} filters	153

B	Data-based corrections to the MC simulation	155
C	Background estimate details	158
	C.1 QCD SB estimate	158
	C.2 $Z \rightarrow \nu\bar{\nu}$ SB estimate	159
D	Differences with respect to published result	162
E	Data Quality Monitoring for the Drift Tube Track Finder	164
	E.1 Drift Tube Track Finder system	164
	E.2 Data Quality Monitoring system	165
	E.3 DTF DQM	167
	Bibliography	171

LIST OF TABLES

2.1	The matter field content of the SM along with the representation under the gauge group and the weak-hypercharge assignments. The index i runs over the three generations of quarks and leptons. The doublet/singlet notation in the second column shows the field decomposition under $SU(2)_L$	5
2.2	The gauge field content of the SM along with their gauge quantum numbers.	5
2.3	The matter superfield content of the MSSM. In the last two columns for leptons and quarks, we show the first family of fields only.	14
2.4	The gauge superfield content of the MSSM.	14
3.1	LHC beam parameters at design performance and at the end of 2011.	27
5.1	MC sample information for background processes. The last column shows the equivalent integrated luminosity of the sample, which is a measure of the total number of events generated. For example, for the $t\bar{t}$ sample, $\sigma \cdot L_{\text{equiv}} \sim 60 \times 10^6$ events were generated. For the $W \rightarrow l\nu$ and $Z \rightarrow l^+l^-$ processes, $l = e, \mu$, and τ combined.	68
5.2	MC sample information for signal processes. For a given gluino (or top-squark) mass, the LSP is constrained kinematically to satisfy $m_{\text{LSP}} < m_{\tilde{g}}$ (or $m_{\text{LSP}} < m_{\tilde{t}}$).	69
5.3	Selection criteria for analysis objects. For the case of electrons, η_{sc} refers to the measurement of the pseudorapidity of the corresponding supercluster.	72
5.4	Search regions definitions. Common selection requirements for all search regions include the criteria described in Sec. 5.3.	74
5.5	Relationship between the search region (SIG) and the corresponding control regions. Common selection requirements for all regions include the criteria described in Sec. 5.3. The variable $\Delta\hat{\phi}_{\text{min}}$ is defined in Sec. 5.5. For the regions that require one or two leptons, a lepton means an e or μ . For the SIG-DL and SB-DL control regions, the threshold on the b -tag discriminant is lowered to $d_{CSV} \geq 0.244$ (see Sec. 5.6).	75
5.6	Expected selection yield in 4.98 fb^{-1} from MC simulation. For $\tilde{g}\tilde{g} \rightarrow bbbb$, we use the benchmark point of $m_{\tilde{g}} = 925 \text{ GeV}$ and $m_{\text{LSP}} = 100 \text{ GeV}$. The Pre- b selection corresponds to the selection requirements of the 1BL region, except with no requirement on the number of b jets. The last column gives the signal-to-background ratio. The uncertainties are statistical only.	76

5.7	Overall H_T^{miss} efficiencies for various offline selections used in the analysis. The 0-lepton (1- e/μ) selection refers to the requirement of zero leptons (one electron/muon) in the evaluation of the efficiency. For all selections, the cuts $H_T \geq 400$ GeV and $\Delta\hat{\phi}_{\text{min}} > 4$ have been applied. Errors shown are statistical only.	79
5.8	Closure test of the QCD background method in QCD MC. The closure is expressed in %.	90
5.9	QCD background prediction in the SIG region. $N_{\text{SIG-LDP}}^{\text{top+EW}}$ is the total non-QCD contamination in the SIG-LDP region. Errors are statistical only.	91
5.10	Systematic uncertainties on the QCD estimate in the SIG region, in %. The total uncertainty is the sum in quadrature of all sources of systematic error. For the 1BT selection, the nominal estimate is zero, so the percent changes due to varying the non-QCD contamination and trigger efficiency are ill-defined. The prediction for this selection is $N_{\text{SIG}}^{\text{QCD}} = 0.1$ when the non-QCD component is reduced by 40%.	92
5.11	MC closure test of the $Z \rightarrow \nu\nu$ prediction method. Errors shown are statistical only. As in Sec. 5.5, we define the closure as the difference between the predicted and true yields, relative to the predicted yield. The closure is expressed in %.	106
5.12	Systematic uncertainties (in %) for the $Z \rightarrow \nu\bar{\nu}$ background prediction.	108
5.13	Purity, acceptance, and efficiencies used for the $Z \rightarrow \nu\nu$ background estimate. The errors shown are statistical only. As discussed in Sec. 5.6.2, the value of the acceptance depends on the choice of offline kinematic cuts. We show the measured values from MC for each selection.	109
5.14	Results for the $Z \rightarrow \nu\bar{\nu}$ background prediction from the $Z \rightarrow e^+e^-$ and $Z \rightarrow \mu^+\mu^-$ control samples separately. Errors are statistical only.	110
5.15	Combined prediction of the $Z \rightarrow \nu\nu$ background. Both statistical and systematic errors are included.	111
5.16	Relative contribution of the $t\bar{t}$ background categories, from MC, for the 1BL selection. In the decay mode of the W , l refers to e or μ , and τ_l (τ_h) refers to the leptonic (hadronic) decay of the τ	112
5.17	Closure test of the top + W prediction method in top + W MC, for each selection. Errors shown are statistical only. As in Secs. 5.5 and 5.6, we define the closure as the difference between the predicted and true yields, relative to the predicted yield. The closure is expressed in %	117
5.18	Systematic uncertainties on the top + W background prediction, expressed in %.	119

5.19	Predicted top + W background yields for each search selection. $N_{\text{SIG}}^{\text{top+W}}$ is corrected for the trigger efficiency in the SIG region. Errors shown are statistical only.	120
5.20	Summary of the SM background estimates and observed data yields. The first (second) error gives the statistical (systematic) uncertainty.	122
5.21	Summary of the systematic uncertainties (in %) on the signal efficiency for the $\tilde{g}\tilde{g} \rightarrow bbbb$ model with $m_{\tilde{g}} = 925$ GeV and $m_{\text{LSP}} = 100$ GeV.	128
5.22	Expected number of events n_i for each of the 11 observables, expressed in terms of the expected yield μ_i^X from each process X . The parameter ε_i is the trigger efficiency in region i . The parameters C_i^X are included to account for the systematic uncertainty on the yield for process X in region i . The factor \mathcal{P}_l ($l = e, \mu$) denotes the $Z \rightarrow l^+l^-$ purity of the sample.	133
A.1	Breakdown of the HT dataset used in the analysis, along with the corresponding run ranges and integrated luminosities. A similar breakdown applies for other datasets used in the analysis for background estimation and efficiency measurements.	146
A.2	Triggers for signal event selection, along with the total integrated luminosity collected with each trigger.	147
A.3	Triggers for the collection of the $Z \rightarrow e^+e^-$ control sample.	148
A.4	Triggers used for the collection of the $Z \rightarrow \mu^+\mu^-$ control sample	149
A.5	Fractional sample composition of two regions in which the $H_{\text{T}}^{\text{miss}}$ efficiencies are measured. The efficiencies measured in these regions are used in the SB and SB-LDP regions of the analysis.	151
A.6	Fractional sample composition of the regions in which the $H_{\text{T}}^{\text{miss}}$ efficiencies are used. The $E_{\text{T}}^{\text{miss}}$ and $\Delta\hat{\phi}_{\text{min}}$ cuts are specified by the first column, while all other offline cuts correspond to the selections denoted in the second column.	151
A.7	$H_{\text{T}}^{\text{miss}}$ efficiency measured in control samples enriched in either top, V+jets, or QCD events. A common selection criteria of $\{150 < E_{\text{T}}^{\text{miss}} < 250, H_{\text{T}} \geq 400$ GeV, no leptons $\}$ is applied.	152
C.1	Closure test of the QCD background method in QCD MC for the SB region. Closure results are reported in %.	158
C.2	QCD-background prediction in the SB region. $N_{\text{SB-LDP}}^{\text{top+W}}$ is the total non-QCD contamination in the SB-LDP region. Errors are statistical only.	159
C.3	Systematic uncertainties (in %) on the QCD prediction in the SB region.	159
C.4	Systematic uncertainties (in %) for $Z \rightarrow \nu\bar{\nu}$ background prediction in SB region.	160

C.5	Results for the $Z \rightarrow \nu\bar{\nu}$ background prediction in the SB region. Errors are statistical only.	161
C.6	Combined prediction for the $Z \rightarrow \nu\bar{\nu}$ background in the SB re- gion. Both statistical and systematic errors are included.	161

LIST OF FIGURES

2.1	Leading order Feynman diagrams for gluino-pair production in hadron collisions.	19
2.2	Leading order Feynman diagrams for squark-pair production in hadron collisions.	20
2.3	Gluino-pair (left) and top-squark-pair (right) production cross section at $\sqrt{s} = 7$ TeV as a function of $m_{\tilde{g}}$ and $m_{\tilde{t}}$, respectively [7]. The green lines give the computed central value and total uncertainty. Also shown in the plots are the cross section values and uncertainties when computed using two different sets of parton distribution functions (CTEQ and MSTW).	21
2.4	Simplified model of gluino-pair production with $BR(\tilde{g} \rightarrow b\bar{b}\tilde{\chi}_1^0) = 100\%$ (left) or $BR(\tilde{g} \rightarrow t\bar{t}\tilde{\chi}_1^0) = 100\%$ (right) [9]. We denote the left model as $\tilde{g}\tilde{g} \rightarrow b\bar{b}b\bar{b}$ and the right model as $\tilde{g}\tilde{g} \rightarrow t\bar{t}t\bar{t}$	23
2.5	Simplified model of top-squark-pair production with $BR(\tilde{t} \rightarrow t\tilde{\chi}_1^0) = 100\%$ [9]. We denote this model as $\tilde{t}\tilde{t} \rightarrow tt$	23
3.1	The CERN accelerator complex (not to scale) [12]. Shown on the LHC ring are the four main experiments: ATLAS, CMS, ALICE, and LHCb.	25
3.2	Perspective view of the CMS detector.[13]	29
3.3	Perspective view of pixel tracker [14]. Each rectangular unit in the barrel layers is a pixel module.	32
3.4	Schematic (r - z) view of the pixel and silicon strip tracker systems [15].	34
3.5	Layout of the CMS electromagnetic calorimeter [16]. Shown are the supermodules of the barrel region, the Dees of the endcap regions, and the preshower detectors. The division of the supermodules into 4 modules and the crystals within a supermodule/Dee are also shown.	35
3.6	Quarter-slice view (in the r - z plane) of the CMS hadronic calorimeter [18]. The lines in η delimit the HCAL towers. "FEE" refers to the location of the Front End Electronics. The different colors indicate the grouping of scintillator layers in the longitudinal readout.	38
3.7	Cross-sectional view of CMS detector (originally from [11]). The drift-tube chambers are shaded in light blue, while the magnet solenoid and iron yoke is shown in gray.	42
3.8	Quarter slice view of the CMS muon detectors [21]. Three of the five wheels of the DT system are shown in green. CSC chambers from each of the eight rings are shown in blue. The position of the RPC detectors are highlighted in red.	43
3.9	Schematic of CMS trigger and data acquisition system [22].	45

5.1	The integrated luminosity collected in 2011 [35]. Of the 5.55 fb^{-1} recorded by the experiment, 4.98 fb^{-1} were recorded with all detectors in a good condition.	66
5.2	Efficiency for the $H_T > 350 \text{ GeV}$ condition (left) and the $H_T^{\text{miss}} > 110 \text{ GeV}$ condition (right) of the tightest trigger. For the H_T^{miss} efficiency, the 0-lepton offline cuts described in Table 5.7 have been applied.	78
5.3	Illustration of the quantities used in the computation of $\Delta\hat{\phi}_{\text{min}}$. The gray (black) arrows indicate the true (measured) magnitude of the momentum of each jet. In this case, jet i is largely mismeasured, inducing a large value of E_T^{miss} in its vicinity.	81
5.4	Distribution of $\Delta\phi_{\text{min}}$ (left) and $\Delta\hat{\phi}_{\text{min}}$ (right) in bins of E_T^{miss} in the QCD MC. The shape of the distribution is largely independent of E_T^{miss} for the case of $\Delta\hat{\phi}_{\text{min}}$	83
5.5	The pass-fail ratio for $\Delta\phi_{\text{min}}$ (top-left) and $\Delta\hat{\phi}_{\text{min}}$ (top-right) in bins of E_T^{miss} for the 1BL selection. A strong dependence on E_T^{miss} is shown for the case of $\Delta\phi_{\text{min}}$, while the pass-fail ratio is largely constant for $E_T^{\text{miss}} \gtrsim 50 \text{ GeV}$ for the case of $\Delta\hat{\phi}_{\text{min}}$. The bottom plot shows the pass-fail ratio for $\Delta\hat{\phi}_{\text{min}}$ in the same selection, except for a $0b$ requirement.	84
5.6	Schematic diagram of the QCD estimate procedure and the relevant regions. The lower E_T^{miss} boundary of the signal region in this diagram corresponds to the 1BL, 2BL, and 3B selections.	86
5.7	Data-MC comparison of $\Delta\hat{\phi}_{\text{min}}$ in the SB and SB-LDP regions for the 1BL (top-left), 2BT (top-right), and 3B (bottom) selections. The hashed area gives the total statistical uncertainty on the MC.	87
5.8	Data-MC comparison of E_T^{miss} (top-left), $\Delta\hat{\phi}_{\text{min}}$ (top-right), and the number of jets (bottom) distributions for events in the LSB region of the 1BL selection, except for the requirement on the variable that is plotted. The hashed area gives the total statistical uncertainty on the MC.	88
5.9	Pass-fail ratio in data collected with the inclusive- H_T sample for $H_T > 400 \text{ GeV}$ (top-left), $H_T > 500 \text{ GeV}$ (top-right), and $H_T > 600 \text{ GeV}$ (bottom) selections. The green histogram shows the non-QCD SM contribution stacked on top of the QCD contribution.	89
5.10	Data-MC comparison of the invariant mass of the two leptons (top row) and E_T^{miss} distributions (bottom row) of the SIG-DL region. The $Z \rightarrow e^+e^-$ ($Z \rightarrow \mu^+\mu^-$) selection is shown on the left (right) plots. In the invariant mass distributions, a cut of $E_T^{\text{miss}} > 150 \text{ GeV}$ is applied. The hashed area gives the total statistical uncertainty on the MC.	95

5.11	Invariant mass distribution of the lepton pairs used for the measurement of ε_{sel} . The top (bottom) plots show the distribution for electron (muon) pairs. The left (right) plots show the distribution of pairs for which the “probe” lepton passes (fails) the lepton selection of the SIG-DL region. The dashed line shows the fit result for the background component (i.e. fake lepton pairs).	97
5.12	$\mathcal{F}(n)$ vs $E_{\text{T}}^{\text{miss}}$ for $Z \rightarrow e^+e^-$ (left) and $Z \rightarrow \mu^+\mu^-$ (right) events in the $\geq 1 b$ (top) and $\geq 2 b$ (bottom) selections. The black (blue) points show the measured values from the data (MC). The red points show the corresponding values from the $Z \rightarrow \nu\nu$ MC.	99
5.13	$\mathcal{F}(n)$ vs H_{T} for $Z \rightarrow e^+e^-$ (left) and $Z \rightarrow \mu^+\mu^-$ (right) events in the $\geq 1 b$ (top) and $\geq 2 b$ (bottom) selections, with $E_{\text{T}}^{\text{miss}} > 150$ GeV. The black (blue) points show the measured values from the data (MC). The red points show the corresponding values from the $Z \rightarrow \nu\nu$ MC.	100
5.14	Distribution of the b jet discriminant in the $Z \rightarrow e^+e^-$ (left) and $Z \rightarrow \mu^+\mu^-$ (right) selection in the data (top row) and the MC (center row). The corresponding distribution from the $Z \rightarrow \nu\nu$ MC is shown in the bottom plot . The black (colored) points correspond to the selection for the SIG-DL (LSB'-DL) regions for the top two rows, and the selection for the SIG (LSB') regions for the bottom row.	101
5.15	Invariant mass distribution in the pure $Z \rightarrow l^+l^-$ sample (top) and the SIG-DL region (bottom) for the $Z \rightarrow e^+e^-$ (left) and $Z \rightarrow \mu^+\mu^-$ (right) selection. The background is fitted with a linear function.	102
5.16	Comparison of the $E_{\text{T}}^{\text{miss}}$ (top) and $\Delta\hat{\phi}_{\text{min}}$ (bottom) distributions between $Z \rightarrow \nu\nu$ MC and $Z \rightarrow l^+l^-$ events in both data and MC, for the $Z \rightarrow e^+e^-$ (left) and $Z \rightarrow \mu^+\mu^-$ (right) selections. The distributions are normalized to unit area. All other nominal 1BL selection cuts are applied, with the exception of a $E_{\text{T}}^{\text{miss}} > 150$ GeV requirement for the bottom plots.	104
5.17	Schematic diagram of the top+W estimate procedure and the relevant regions. The lower $E_{\text{T}}^{\text{miss}}$ boundary of the signal region in this diagram corresponds to the 1BL, 2BL, and 3B selections.	114
5.18	Comparison between the data and MC of the $E_{\text{T}}^{\text{miss}}$ distribution in the SL control sample for the 1BL (top-left), 2BT (top-right), and 3B (bottom) selections. The hashed area gives the total statistical uncertainty on the MC.	115
5.19	Comparison of the $E_{\text{T}}^{\text{miss}}$ distribution for top + W events between the SL region (red) and the nominal region (blue) for the 1BL (top-left), 2BT (top-right), and 3B (bottom) selections. The plots below the main figures give the ratio of the blue and red distributions. We find very good agreement between the two regions.	116

5.20	Comparison of the E_T^{miss} distribution between the data and the SM background predictions for the 1BL (top-left), 2BT (top-right), and 3B (bottom) selections. The background predictions are estimated in each bin of E_T^{miss} . The hashed area gives the total uncertainty on the predictions, which is correlated between bins. The open histograms give the expected yield from the $\tilde{g}\tilde{g} \rightarrow bbbb$ and $\tilde{g}\tilde{g} \rightarrow tttt$ models with $m_{\tilde{g}} = 925$ GeV and $m_{\text{LSP}} = 100$ GeV, normalized to the reference cross section.	123
5.21	Signal efficiency (in %) for the $\tilde{g}\tilde{g} \rightarrow bbbb$ model in the 1BL (top-left), 2BT (top-right), and 3B (bottom) selections. The gray cells indicate mass points that are not considered due to their sensitivity to ISR.	124
5.22	Signal efficiency (in %) for the $\tilde{g}\tilde{g} \rightarrow tttt$ model in the 1BL (top-left), 2BT (top-right), and 3B (bottom) selections.	125
5.23	Signal efficiency (in %) for the $\tilde{t}\tilde{t} \rightarrow tt$ model in the 1BT (left) and 2BL (right) selections. The gray cells indicate mass points that are not considered due to their sensitivity to ISR.	125
5.24	Relative systematic uncertainty (in %) on the signal efficiency in the 1BL (top-left), 2BT (top-right), and 3B (bottom) selections for the $\tilde{g}\tilde{g} \rightarrow bbbb$ model. The gray cells indicate mass points that are not considered due to their sensitivity to ISR.	129
5.25	Relative systematic uncertainty (in %) on the signal efficiency in the 1BL (top-left), 2BT (top-right), and 3B (bottom) selections for the $\tilde{g}\tilde{g} \rightarrow tttt$ model.	130
5.26	Relative systematic uncertainty (in %) on the signal efficiency in the 1BT (left) and 2BL (right) selections for the $\tilde{t}\tilde{t} \rightarrow tt$ model. The gray cells indicate mass points that are not considered due to their sensitivity to ISR.	131
5.27	The selection that gives the lowest expected upper limit at each mass point in the $\tilde{g}\tilde{g} \rightarrow bbbb$ (top-left), $\tilde{g}\tilde{g} \rightarrow tttt$ (top-right), and $\tilde{t}\tilde{t} \rightarrow tt$ (bottom) models. The gray cells indicate mass points that are not considered due to their sensitivity to ISR.	138
5.28	Observed 95% C.L. upper limit on the cross section for the $\tilde{g}\tilde{g} \rightarrow bbbb$ model with the selection at each mass point given in Fig. 5.27. The black (violet) curve shows the observed (expected) exclusion region using the reference $\tilde{g}\tilde{g}$ production cross section. Mass points below the curve are excluded. The experimental uncertainty on the expected limit corresponds to the total uncertainty on the background estimate, while the theory uncertainty on the observed limit is the uncertainty on the reference cross section.	139

5.29	Observed 95% C.L. upper limit on the cross section for the $\tilde{g}\tilde{g} \rightarrow tttt$ model with the selection at each mass point given in Fig. 5.27. The black (violet) curve shows the observed (expected) exclusion region using the reference $\tilde{g}\tilde{g}$ production cross section. Mass points below the curve are excluded. The experimental uncertainty on the expected limit corresponds to the total uncertainty on the background estimate, while the theory uncertainty on the observed limit is the uncertainty on the reference cross section.	140
5.30	Observed 95% C.L. upper limit on the cross section for the $\tilde{t}\tilde{t} \rightarrow tt$ model with the selection at each mass point given in Fig. 5.27. We do not exclude any mass points using the reference $\tilde{t}\tilde{t}$ production cross section.	141
5.31	Observed (solid red curve) and expected (dashed blue curve) 95% C.L. upper limit on the cross section for the $\tilde{t}\tilde{t} \rightarrow tt$ model at $m_{\text{LSP}} = 50 \text{ GeV}$ with the 1BT selection. The experimental uncertainty on the expected limit corresponds to the total uncertainty on the background estimate. The black curve gives the reference $\tilde{t}\tilde{t}$ production cross section, with its associated uncertainty in the yellow band.	142
5.32	A $\rho - \phi$ view of the event with the highest value of $E_{\text{T}}^{\text{miss}}$ in 3B selection. The inner green lines show the reconstructed tracks, while the red (blue) bars emanating from the central circle show the size of the ECAL (HCAL) deposits. The yellow lines give the direction of each reconstructed jet.	143
5.33	A $\rho - z$ view of the event with highest value of $E_{\text{T}}^{\text{miss}}$ in 3B selection. The inner green lines show the reconstructed tracks, while the red (blue) bars emanating from the central rectangle show the size of the ECAL (HCAL) deposits. The yellow lines give the direction of each reconstructed jet.	144
E.1	Schematic of the DTF system [61]. For the purposes of track-finding, the central wheel is logically divided into two halves.	165
E.2	Schematic of the two stages of the DQM workflow [62].	166
E.3	Distribution of the track occupancy in $\eta - \phi$ space (left) and divided into the DT sectors vs. wheels (right). The low occupancy of wheel N0 is visible and arises from the fact that the wheel is responsible only for reconstructing tracks that exit the central wheel from the negative side.	168
E.4	Distributions of track η (top-left), ϕ (top-right), p_{T} (bottom-left), and charge (bottom-right). The cracks between DT sectors can be seen in the track- ϕ distribution.	169

E.5	Track quality information. The left plot gives the distribution of track quality codes in each wheel. The seven quality codes on the y-axis are arranged in order of increasing quality. The right plot gives the fraction of tracks with quality code > 3 (corresponding to "T12/13/14" on the left plot) for each sector of each wheel.	169
E.6	Distribution of the bunch crossing assignment of tracks for each wheel. In this run, most tracks are assigned the correct bunch crossing (BX=0).	170
E.7	Information on the communication between the DTTF and GMT. The left plot shows the fraction of tracks that have matching GMT tracks. The right plot gives the fraction of DTTF tracks without a GMT match per sector and wheel. The increase in deleted tracks in the external wheels is clearly visible.	170

CHAPTER 1

INTRODUCTION

A theory describing the basic structure of nature has been forged over the past several decades. This theory, called the standard model of particle physics, has been successful in describing a fantastic variety of phenomena with remarkable precision. However, there remain several key questions that are left unanswered by the standard model and it is expected that a more fundamental theory will emerge as one begins to probe length scales smaller than 10^{-17} cm or, equivalently, energy scales larger than 1 TeV.

The Large Hadron Collider (LHC) at CERN was built to explore this uncharted energy regime. Colliding protons at an unprecedented center-of-mass energy of 7 TeV in 2011, the LHC hopes to reveal any signs of new physics at this scale. With the Compact Muon Solenoid (CMS) detector, one can measure in great detail the properties of the particles produced from the proton collisions. Over many collisions, the production of new, heavy particles can then be statistically inferred. One possible source of new particles arises in theories that contain a symmetry called *supersymmetry*. In such a theory, one expects to observe the presence of these new, heavy states through their decay into jets — collimated streams of energetic hadrons. Moreover, these decays are expected to produce new weakly interacting particles, which, like neutrinos, escape the detector unobserved. This typically results in events with a large momentum imbalance in the plane transverse to the beamline, a quantity denoted as E_T^{miss} . Finally, many models of supersymmetry predict relatively strong couplings to heavy flavor quarks, leading to events with a final state signature containing multiple *b*-quarks.

The subject of this thesis is the search for new physics in events containing large E_T^{miss} , no leptons, at least three jets, and one or more b jets. This thesis is organized as follows. We begin in Chapter 2 with a brief review of the standard model and a discussion of the motivation for a more fundamental theory. We then review the basic formalism and phenomenology of supersymmetry. In Chapter 3, we give an overview of the LHC accelerator and the CMS detector. In Chapter 4, we describe the techniques used to reconstruct the particles produced from a collision event. The rest of the thesis, beginning in Chapter 5, describes the analysis. After a description of the event selection and the various search regions, we discuss in detail the estimation of each of the major background components. Finally, the results of the search are interpreted in the context of supersymmetric models. Chapter 6 concludes with a summary of the analysis. Further details of the analysis can be found in the Appendices.

CHAPTER 2

PHYSICS BEYOND THE STANDARD MODEL

The standard model (SM) of particle physics is a theory describing the known fundamental interactions of nature. As a culmination of many theoretical advances and experimental discoveries over the past several decades, the SM has proven to be tremendously successful in describing a vast range of phenomena. The *Review of Particle Physics* [1], a 1500-page compendium of all experimental measurements in particles physics performed to date, serves as a testament to the triumph of the theory. Nevertheless, there are significant reasons to believe that the SM acts as a low-energy effective theory to a more fundamental theory. It is the search for new phenomena revealing this underlying theory that drives the research in the field of particle physics today.

We begin this chapter with a terse review of the standard model. We then discuss the existing shortcomings of the theory and provide a motivation for a new underlying symmetry in nature called supersymmetry (SUSY). After a rudimentary description of the formulation of a supersymmetric theory, we review the simplest supersymmetric extension of the standard model. Finally, we discuss the particle phenomenology of this extension, with a focus on processes giving rise to topologies enriched with b -quarks. Much of the discussion in this chapter follows that of References [2]-[3].

2.1 The standard model

The standard model of particle physics is a quantum field theory describing the electromagnetic, weak, and strong interactions. The underlying local gauge symmetry of the theory is $SU(3)_C \times SU(2)_L \times U(1)_Y$, where $SU(3)_C$ describes the strong interaction of colored particles, $SU(2)_L$ the weak-isospin, and $U(1)_Y$ the weak-hypercharge. The SM consists of a single scalar field and three copies (called “families” or “generations”) of five fermion fields. The matter field content of the SM is summarized in Table 2.1. Interactions between the matter fields are mediated through a set of vector fields determined by the gauge symmetry. The vector fields are listed in Table 2.2. The SM Lagrangian is given by

$$\begin{aligned}
\mathcal{L}_{\text{SM}} = & -\frac{1}{4}G_{A\mu\nu}G_A^{\mu\nu} - \frac{1}{4}F_{a\mu\nu}F_a^{\mu\nu} - \frac{1}{4}B_{\mu\nu}B^{\mu\nu} \\
& + \bar{Q}_i \gamma^\mu (i\partial_\mu - \frac{1}{2}g_s G_{A\mu} \lambda_A - \frac{1}{2}g W_{a\mu} \tau_a - g' B_\mu Y) Q_i \\
& + \bar{L}_i \gamma^\mu (i\partial_\mu - \frac{1}{2}g W_{a\mu} \tau_a - g' B_\mu Y) L_i \\
& + \bar{U}_i \gamma^\mu (i\partial_\mu + \frac{1}{2}g_s G_{A\mu} \lambda_A^* - g' B_\mu Y) U_i \\
& + \bar{D}_i \gamma^\mu (i\partial_\mu + \frac{1}{2}g_s G_{A\mu} \lambda_A^* - g' B_\mu Y) D_i \\
& + \bar{E}_i \gamma^\mu (i\partial_\mu - g' B_\mu Y) E_i \\
& + |(i\partial_\mu - \frac{1}{2}g W_{a\mu} \tau_a - g' B_\mu Y) H|^2 - \lambda \left(H^\dagger H - \frac{1}{2}v^2 \right)^2 \\
& - (y_{jk}^L \bar{L}_j H E_k + y_{jk}^D \bar{Q}_j H D_k + y_{jk}^U \bar{Q}_{\alpha j} \epsilon^{\alpha\beta} H_\beta^\dagger U_k + h.c.), \tag{2.1}
\end{aligned}$$

where the index A runs over the eight color gauge fields, the index a over the three weak gauge fields, the indices $\{i, j, k\}$ run over the three generations of quarks and leptons, the indices $\{\alpha, \beta\}$ run over the $SU(2)_L$ doublet, and where $\epsilon_{\alpha\beta}$ is the totally antisymmetric tensor. In Eq. 2.1, the kinetic energies and self-interactions of the gauge fields are shown in the first line, the kinetic energies and gauge-interaction terms of the left-handed quarks and leptons in the second

and third lines, the corresponding terms for the right-handed fields in the fourth to sixth lines, the Higgs kinetic and potential terms in the eighth line, and the lepton and quark Yukawa interactions in the last line. The generators T_a of the $SU(2)_L$ group are given explicitly in their representation form — for example, as Pauli matrices τ_a for the case of $SU(2)_L$ doublets. Similarly, the generators of the $SU(3)_C$ group are given by the Gell-Mann matrices λ_A for the quark fields. The hypercharges Y for the fields have the values listed in Tables 2.1 and 2.2.

Table 2.1: The matter field content of the SM along with the representation under the gauge group and the weak-hypercharge assignments. The index i runs over the three generations of quarks and leptons. The doublet/singlet notation in the second column shows the field decomposition under $SU(2)_L$.

Name	Field	$SU(3)_C, SU(2)_L, U(1)_Y$
Leptons	$L_i = \begin{pmatrix} \nu_{eL} \\ e_L \end{pmatrix}, \begin{pmatrix} \nu_{\mu L} \\ \mu_L \end{pmatrix}, \begin{pmatrix} \nu_{\tau L} \\ \tau_L \end{pmatrix}$	$(\mathbf{1}, \mathbf{2}, -\frac{1}{2})$
	$E_i = e_R, \mu_R, \tau_R$	$(\mathbf{1}, \mathbf{1}, -1)$
Quarks	$Q_i = \begin{pmatrix} u_L \\ d_L \end{pmatrix}, \begin{pmatrix} c_L \\ s_L \end{pmatrix}, \begin{pmatrix} t_L \\ b_L \end{pmatrix}$	$(\mathbf{3}, \mathbf{2}, \frac{1}{6})$
	$U_i = u_R, c_R, t_R$	$(\bar{\mathbf{3}}, \mathbf{1}, \frac{2}{3})$
	$D_i = d_R, s_R, b_R$	$(\bar{\mathbf{3}}, \mathbf{1}, -\frac{1}{3})$
Higgs	$H = \begin{pmatrix} h^+ \\ h^0 \end{pmatrix}$	$(\mathbf{1}, \mathbf{2}, \frac{1}{2})$

Table 2.2: The gauge field content of the SM along with their gauge quantum numbers.

Name	Field	$SU(3)_C, SU(2)_L, U(1)_Y$
Gluons	$G^A, A = 1, \dots, 8$	$(\mathbf{8}, \mathbf{1}, 0)$
W bosons	$W^a, a = 1, 2, 3$	$(\mathbf{1}, \mathbf{3}, 0)$
B boson	B	$(\mathbf{1}, \mathbf{1}, 0)$

Explicit mass terms in \mathcal{L} for the fermions and gauge bosons are forbidden by

the local gauge symmetry of the theory. Instead, mass terms in the Lagrangian are generated through the Higgs field H acquiring a non-zero vacuum expectation value (vev). The reformulation of the Higgs field about a particular non-zero ground state with vev v hides the manifest electroweak symmetry of the theory and leaves a single combination of the generators of $SU(2)_L \times U(1)_Y$ invariant, namely $Q = T_3 + Y$. The group generated by Q is denoted as $U(1)_{em}$ and corresponds to the electric charge of the fields. This process is referred to as the spontaneous symmetry breaking of the electroweak gauge group: $SU(2)_L \times U(1)_Y \rightarrow U(1)_{em}$. Through this mechanism, the charged W bosons and neutral Z boson, expressed as

$$\begin{aligned} W_\mu^\pm &= \frac{1}{\sqrt{2}} (W_\mu^1 \mp iW_\mu^2) \\ Z_\mu &= \frac{1}{\sqrt{g^2 + g'^2}} (gW_\mu^3 - g'B_\mu), \end{aligned} \quad (2.2)$$

acquire masses of $m_W = gv/2$ and $m_Z = \sqrt{g^2 + g'^2}v/2$, respectively. Meanwhile, the photon, given by

$$A_\mu = \frac{1}{\sqrt{g^2 + g'^2}} (g'W_\mu^3 + gB_\mu), \quad (2.3)$$

and identified as the gauge field of the unbroken $U(1)_{em}$ symmetry, remains massless. The mass eigenstates Z_μ and A_μ can be viewed as a rotation of the W_μ^3 and B_μ fields by an angle θ_W , where $\tan \theta_W = g/g'$. Finally, a massive neutral scalar Higgs boson remains from the symmetry breaking. In addition to providing mass terms for the W^\pm and Z gauge bosons, the Higgs field creates mass terms for fermions through the Yukawa interaction terms of Eq. 2.1.

The SM consists of 19 free parameters; 6 parameters arise from the masses of the quarks, 3 from the charged lepton masses, 4 from the quark mixing matrix, 3 from the gauge couplings (g_s, g, g'), 2 from the Higgs terms (λ, v), and an additional term arises from the strong interaction. Of these parameters, the single

energy scale of the SM is the Higgs vacuum expectation value v . This parameter can be computed through the measurement of the Fermi constant of muon decay ($G_F = 1/\sqrt{2}v^2$) and has a value of $v \sim 246$ GeV.

The SM accounts for a wide variety of phenomena and has been tested to a remarkable level of precision [1]. Despite its success, however, there are several reasons, from both experimental observations and theoretical considerations, to believe that the SM is an incomplete theory of nature.

2.2 Beyond the standard model

The major questions raised by experimental observations that the SM cannot answer include the following:

- Given the observation of neutrino oscillations, what is the correct way to incorporate massive neutrinos into the SM, and why are neutrino masses so much smaller than the other particles of the theory?
- What is the particle nature of the dark matter evident from astronomical measurements? Moreover, cosmological observations suggest that the vast majority of the energy in the Universe exists in an unknown form called “dark energy”. What is the nature of dark energy?
- What is the mechanism responsible for the matter/antimatter asymmetry observed in the Universe?
- What is the fundamental interaction responsible for gravity?

From a theoretical perspective, one might also inquire as to the reason for the SM to have 19 parameters, three generations of quarks and leptons, and the particular choice of the gauge symmetry group. It is widely believed that a more fundamental theory is needed to explain this complicated structure. At what scale might one expect to see the emergence of an underlying theory? There exists one particular argument involving the scalar Higgs field that suggests a specific energy scale, which we discuss below.

2.2.1 The TeV scale

If one were to compute the higher order corrections to the mass of the Higgs boson within the SM, one would find that the corrections are quadratically dependent on the momentum-scale cut-off:

$$m_H^2(\text{physical}) \sim m_H^2 - c\Lambda^2, \quad (2.4)$$

where m_H is the bare Higgs mass of the SM Lagrangian, Λ the cut-off scale, and c a coefficient whose form depends on the various coupling parameters. We can interpret Λ to be the scale above which the SM is no longer valid. Measurements of the weak interactions have restricted the physical Higgs boson mass to be less than a few hundred GeV. If Λ were to be much larger than $O(\text{TeV})$, then the bare mass m_H would need to be tuned such that the physical Higgs mass remains below its expected upper bound. For example, assuming that the SM is valid up to the scale of grand unified theories ($\Lambda \sim 10^{16} \text{ GeV}$) implies that m_H would need to be tuned to 1 part in 10^{26} . While it may indeed be the case that nature has chosen the value of m_H to such an extreme level of precision, it is usually interpreted as an indication that the assumption that the SM is valid to

such a high energy scale is incorrect. This “fine-tuning” problem suggests that the actual cut-off should be around the TeV scale. If this is true, then there must be some new physics at this scale that can remove the quadratic divergence.

Several ideas have been developed to accommodate this problem. One class of models, under the name of technicolor, avoid the fine-tuning problem by proposing that the Higgs field is not an elementary scalar, but instead a bound state of fermions. Another proposal is that there are extra spatial dimensions with TeV length scales. These extra dimensions would account for the apparent weakness of gravity and would bring the cut-off Λ down from the traditional Planck scale to the TeV scale, above which effects from gravity become important.

If instead we assume that the Higgs is a fundamental scalar particle and that there is indeed a more fundamental theory at a much higher energy scale, then there must be some mechanism at the TeV scale that can tame the above quadratic divergence. Since the sign of the coefficient c in Eq. 2.4 depends on whether the higher-order correction involves a boson or fermion, one might hope to achieve a fortuitous cancellation of the divergence if there existed new particles of a half-integer spin difference to the SM particles at the TeV scale. Such a cancellation would necessarily be the result of an underlying symmetry between fermions and bosons, which is called a supersymmetry (SUSY).

2.2.2 Supersymmetry

To establish a symmetry between fermions and bosons, we consider the notion of a “superfield” that groups a spin- $\frac{1}{2}$ field f and a spin-0 field \tilde{f} into a single

entity:

$$\hat{F} = (\tilde{f}, f) \tag{2.5}$$

An infinitesimal transformation that mixes f and \tilde{f} can be constructed by allowing the infinitesimal parameter ϵ of the transformation to be itself a spinor field. An example of such a transformation is given by

$$\begin{aligned} \delta\tilde{f} &= 2\bar{\epsilon}f \\ \delta f &= -i\gamma^\mu\epsilon(\partial_\mu\tilde{f}). \end{aligned} \tag{2.6}$$

This transformation leaves invariant (up to a total derivative) the combination of the free Klein-Gordon Lagrangian of \tilde{f} and the free Dirac Lagrangian of f , provided that the two fields share the same mass. Of particular interest (for the purpose of constructing a supersymmetric extension of the SM) are superfields for which the fermion component is left-handed

$$\hat{F}_L = (f_L, \tilde{f}), \tag{2.7}$$

which we refer to as left-chiral superfields. Similarly, a gauge superfield is formed by joining a spin-1 field G_μ with a spin- $\frac{1}{2}$ counterpart \tilde{g} :

$$\hat{G} = (\tilde{g}, G_\mu). \tag{2.8}$$

In the above description, we have been intentionally cavalier in the treatment of superfields. Special care must be taken when forming multiplets of fields with different spin, since the fields behave differently under Lorentz transformations. Formally, fermion and boson fields are grouped together by introducing a spinor coordinate θ whose four components θ_i are anti-commuting numbers. A superfield is then constructed as a linear combination of fermion and boson fields in the space spanned by products of the θ_i components.

Supersymmetry is an extension of the usual spacetime symmetries. In contrast to the Lorentz and translation transformations, however, the generator of a supersymmetry transformation is a spin- $\frac{1}{2}$ Majorana spinor Q_a , where a is the spinor index. If the supersymmetry “charge” specified by Q_a is conserved, then it must satisfy $[Q_a, P^0] = 0$, where $P^0 = H$ is the Hamiltonian. More generally, we have the relation

$$[Q_a, P^\mu] = 0. \quad (2.9)$$

In addition, the generator satisfies the following anti-commutation relation:

$$\{Q_a, \bar{Q}_b\} = 2(\gamma^\mu)_{ab} P_\mu. \quad (2.10)$$

How does one construct a supersymmetric Lagrangian? In an ordinary field theory with spin- $\frac{1}{2}$ and spin-0 fields, the Lagrangian is determined by the choice of the scalar potential. Similarly, a supersymmetric Lagrangian of left-chiral superfields \hat{F}_{Li} is specified by the so-called Kähler potential and superpotential functions. The Kähler potential contributes terms that include the conventional kinetic energies of the fields ($\mathcal{L} = (\partial_\mu \tilde{f}_i)^\dagger (\partial^\mu \tilde{f}_i) + \frac{i}{2} \tilde{f}_i \partial_\mu \gamma^\mu f_i$), while the superpotential is defined as a polynomial $V(\hat{F}_{Li})$ of left-chiral superfields. A supersymmetric Lagrangian of scalar and spinor fields has the generic form:

$$\mathcal{L}_{\text{SUSY}} = (\partial_\mu \tilde{f}_i)^\dagger (\partial^\mu \tilde{f}_i) + \frac{i}{2} \tilde{f}_i \partial_\mu \gamma^\mu f_i - \left. \frac{\partial V}{\partial \hat{F}_{Li}} \right|_{\hat{F}_L = \tilde{f}}^2 - \frac{1}{2} \left(\left. \frac{\partial^2 V}{\partial \hat{F}_{Li} \partial \hat{F}_{Lj}} \right|_{\hat{F}_L = \tilde{f}} \tilde{f}_i f_{Lj} + h.c. \right), \quad (2.11)$$

where a sum over all superfields i is implied, and where the notation $\hat{F}_L = \tilde{f}$ means that after the derivative is evaluated, the superfields are set to their scalar field components. The third term in this expression gives the scalar potential of the Lagrangian, while the last term provides the masses and interactions. To ensure that the supersymmetric theory also preserves the local gauge symmetry required by the standard model, one must insert covariant derivatives

as well as gauge kinetic and gauge-scalar-fermion interaction terms into $\mathcal{L}_{\text{SUSY}}$, analogous to what is done in the SM. This will introduce several new terms to Eq. 2.11, the expressions for which can be found in Reference [2].

Eq. 2.9 implies that supersymmetric partners must have the same mass. Indeed, for a given bosonic eigenstate, we have (with $P^0 = H$)

$$H(Q | \mathcal{B}\rangle) = QH | \mathcal{B}\rangle = E_B Q | \mathcal{B}\rangle, \quad (2.12)$$

so that the fermionic state $| \mathcal{F}\rangle = Q | \mathcal{B}\rangle$ has the same energy. Of course, SUSY must be a broken symmetry, since we would otherwise have long found a boson with the same mass and charge as the electron. Therefore, SUSY-breaking terms must be included in any SUSY Lagrangian attempting to provide a description of nature. However, one must be careful to include only SUSY-breaking terms that preserve the cancellation of quadratic divergences between the scalar and fermion components. Such terms are said to break SUSY “softly”. We will illustrate the form of soft SUSY-breaking terms in the next section. The addition of soft SUSY-breaking terms to the Lagrangian is to be interpreted as a stopgap; they provide an effective Lagrangian that captures the phenomenological impact of SUSY breaking without requiring knowledge of the fundamental mechanism by which SUSY is broken.

2.2.3 The Minimal Supersymmetric Standard Model

The simplest extension of the standard model that includes supersymmetry is referred to as the Minimal Supersymmetric Standard Model (MSSM). The theory contains the smallest number of new particles and assumes the same local gauge symmetry as the SM. Following the prescription of the previous section,

the matter and gauge fields are promoted to left-chiral and gauge superfields, respectively. To express the usual right-handed fields of the SM in terms of left-chiral superfields, we take the charge-conjugate of those fields. Particles that correspond to the superpartner fields are referred to as sparticles. The scalar superpartners of quarks and leptons are called squarks and sleptons, while the fermion superpartners of the gauge fields are called gauginos. Similarly, the fermion superpartner of the Higgs scalar is called the higgsino. Superpartner fields have the same gauge quantum numbers as their SM field counterpart. Tables 2.3 and 2.4 summarize the matter and gauge field content, respectively, of the MSSM. The subscripts L and R on the scalar superpartner fields refer to the chirality of their spin- $\frac{1}{2}$ counterpart.

The Higgs sector of the MSSM is expanded to have two left-chiral superfields with hypercharges $Y = \pm\frac{1}{2}$. A second Higgs superfield is needed to impart mass to the down-type quarks and charged leptons in a manner allowed by the superpotential and to cancel unwanted anomalies introduced by the addition of a higgsino from the first Higgs superfield.

The superpotential of the MSSM is given by

$$V = \mu \hat{H}_u^\alpha \hat{H}_{d\alpha} + (\mathbf{f}_u)_{ij} \epsilon_{\alpha\beta} \hat{Q}_i^\alpha \hat{H}_u^\beta \hat{U}_j^c + (\mathbf{f}_d)_{ij} \hat{Q}_i^\alpha \hat{H}_d^\alpha \hat{D}_j^c + (\mathbf{f}_e)_{ij} \hat{L}_i^\alpha \hat{H}_d^\alpha \hat{E}_j^c \quad (2.13)$$

where $(\mathbf{f}_{u/d/e})_{ij}$ are the Yukawa interaction matrices and $\{i, j\}$ the generation indices. It is apparent from the expression of the superpotential that V is invariant under the parity defined such that quark and lepton superfields are odd, while gauge and Higgs superfields are even. This leads to the notion of the R -parity of a component field, defined as:

$$R = (-1)^{3B+L+2s}, \quad (2.14)$$

Table 2.3: The matter superfield content of the MSSM. In the last two columns for leptons and quarks, we show the first family of fields only.

Name	Superfield	spin-0	spin- $\frac{1}{2}$
Leptons, Sleptons	$\hat{L}_i = \begin{pmatrix} \hat{\nu}_e \\ \hat{e} \end{pmatrix}, \begin{pmatrix} \hat{\nu}_\mu \\ \hat{\mu} \end{pmatrix}, \begin{pmatrix} \hat{\nu}_\tau \\ \hat{\tau} \end{pmatrix}$ $\hat{E}_i^c = \hat{e}^c, \hat{\mu}^c, \hat{\tau}^c$	$\tilde{\nu}_L, \tilde{e}_L$ \tilde{e}_R^\dagger	ν_L, e_L e_L^c
Quarks, Squarks	$\hat{Q}_i = \begin{pmatrix} \hat{u} \\ \hat{d} \end{pmatrix}, \begin{pmatrix} \hat{c} \\ \hat{s} \end{pmatrix}, \begin{pmatrix} \hat{t} \\ \hat{b} \end{pmatrix}$ $\hat{U}_i^c = \hat{u}^c, \hat{c}^c, \hat{t}^c$ $\hat{D}_i^c = \hat{d}^c, \hat{s}^c, \hat{b}^c$	\tilde{u}_L, \tilde{d}_L \tilde{u}_R^\dagger \tilde{d}_R^\dagger	u_L, d_L u_L^c d_L^c
Higgs, Higgsinos	$\hat{H}_u = \begin{pmatrix} \hat{h}_u^+ \\ \hat{h}_u^0 \end{pmatrix}$ $\hat{H}_d = \begin{pmatrix} \hat{h}_d^- \\ \hat{h}_d^0 \end{pmatrix}$	h_u^+, h_u^0 h_d^-, h_d^0	$\tilde{h}_u^+, \tilde{h}_u^0$ $\tilde{h}_d^-, \tilde{h}_d^0$

Table 2.4: The gauge superfield content of the MSSM.

Name	Superfield	spin-1	spin- $\frac{1}{2}$
Gluons, Gluinos	$\hat{G}^A, A = 1, \dots, 8$	G_μ^A	\tilde{g}^A
W bosons, Winos	$\hat{W}^a, a = 1, 2, 3$	W_μ^a	\tilde{W}^a
B boson, Bino	\hat{B}	B_μ	\tilde{B}

where B and L are the usual baryon and lepton number for the field, and s is the spin of the field. All SM particles have even R -parity ($R = +1$), while all superpartners have odd R -parity ($R = -1$). The conservation of R -parity has important phenomenological implications, including the property that the lightest supersymmetric particle (LSP) is stable. In fact, the presence of a stable LSP is one of the attractive features of R -parity-conserving SUSY models as the LSP is considered a good candidate for dark matter. We note here that the addition of baryon- and lepton-number-violating terms to the superpotential would break

R -parity symmetry. Since B - and L -violating terms can lead to processes such as proton decay ($p \rightarrow \pi^0 e^+$) or $\mu \rightarrow 3e$, which have very tight experimental constraints, these terms must be strongly suppressed. In the MSSM, such terms are forbidden entirely by imposing R -parity symmetry.

The terms of the MSSM Lagrangian that give rise to soft SUSY breaking are given by

$$\begin{aligned}
\mathcal{L}_{\text{soft}} = & -\left(\tilde{X}_i^\dagger \mathbf{m}_{Xij}^2 \tilde{X}_j + m_{H_u}^2 |H_u|^2 + m_{H_d}^2 |H_d|^2\right) \\
& -\frac{1}{2}\left(M_1 \tilde{B}\tilde{B} + M_2 \tilde{W}^a \tilde{W}^a + M_3 \tilde{g}^A \tilde{g}^A + h.c.\right) \\
& + \mathbf{a}_{xij} \epsilon_{\alpha\beta} \tilde{X}_i^\alpha H_u^\beta \tilde{x}_{Rj}^\dagger + h.c. \\
& + b H_u^\alpha H_d^\alpha + h.c., \tag{2.15}
\end{aligned}$$

where X denotes all squark and slepton fields, \mathbf{m}_X^2 the corresponding mass matrix, $M_{1,2,3}$ the gaugino masses, and \mathbf{a}_x the electroweak trilinear coupling matrices. The full MSSM Lagrangian is thus given by $\mathcal{L}_{\text{MSSM}} = \mathcal{L}_{\text{SUSY}} + \mathcal{L}_{\text{soft}}$, where $\mathcal{L}_{\text{SUSY}}$ is the locally gauge invariant extension of Eq. 2.11.

The MSSM contains 9 parameters in the gauge sector, 5 parameters in the Higgs sector, and a whopping 110 parameters from the soft SUSY breaking component of the Lagrangian, giving a total of 124 parameters to the theory. It is hoped that once the underlying mechanism of SUSY breaking is understood, the large number of parameters can be significantly reduced.

The spontaneous symmetry breaking of the electroweak gauge group proceeds in a manner similar to that in the SM. In the MSSM, the minimum of the scalar potential is defined by terms in the Kähler potential, superpotential, and the soft SUSY-breaking components of the Lagrangian. Vacuum expectation values v_u and v_d are acquired by the neutral components of H_u and H_d , respec-

tively. The SM expressions for the mass of the W and Z bosons can be simply cast in terms of these vev's via the relation $v = \sqrt{v_u^2 + v_d^2}$. An important phenomenological quantity is the ratio of the vacuum expectation values, defined as $\tan\beta = v_u/v_d$. The two Higgs doublets of the MSSM contain eight real degrees of freedom, three of which are absorbed into the W^\pm and Z bosons. The remaining five become massive Higgs bosons. Three of the five (denoted h^0 , H^0 , and A) are electrically neutral, while the remaining two are charge conjugates H^\pm . The MSSM predicts several important bounds on the masses of the Higgs bosons. In particular, the mass of lightest Higgs boson h^0 is expected to be less than about 130 GeV.

The terms resulting from electroweak symmetry breaking and from the soft SUSY-breaking component give rise to mixing between the gaugino and higgsinos. The 4 neutral mass eigenstates of the mixing matrix are called neutralinos and are denoted as $\tilde{\chi}_i^0$, while the two charged mass eigenstates are called charginos and denoted as $\tilde{\chi}_i^\pm$.

The gluino mass arises solely from the soft SUSY-breaking term $m_{\tilde{g}} = |M_3|$, whereas squark masses are generated from the Kähler potential, superpotential, and soft SUSY-breaking terms. A significant amount of mixing occurs with the top squarks \tilde{t}_L and \tilde{t}_R , as the off-diagonal elements of the mass matrix are proportional to m_t . Moreover, the diagonal terms of the mass matrix are smaller for top squarks than for other squarks due to effects from the renormalization group equations. As a result, top squarks are expected to be the lightest of all squarks. Their mass eigenstates are denoted as $\tilde{t}_{1,2}$. Similarly, bottom squarks are typically lighter than the squarks of the first two generations. For bottom squarks, the size of the mixing, and hence the masses of $\tilde{b}_{1,2}$, are determined by

the value of $\tan\beta$. If $\tan\beta \lesssim 10$, then only a small amount of mixing occurs and $\tilde{b}_{L,R}$ are close to their mass eigenstates. If $\tan\beta$ is large, then the Yukawa and trilinear coupling terms $\{f_b, a_b\}$, which appear in the off-diagonal elements of the mass matrix, become large and cause \tilde{b}_1 to be much lighter than the first and second generation squarks.

It is customary to reduce the MSSM to a smaller set of parameters by making a few simplifying assumptions. One assumption, motivated by constraints in flavor-changing neutral currents and CP-violation, is the universality in the SUSY-breaking masses and trilinear couplings

$$\mathbf{m}_X^2 = m_X^2 \mathbf{1}, \quad \mathbf{a}_x = A_x \mathbf{f}_x, \quad (2.16)$$

where X denotes each quark and lepton field separately. In addition, a remarkable feature of the MSSM is that the gauge couplings g_i of the strong, weak, and electromagnetic interactions, when computed as a function of the energy scale via the renormalization group equations, unify at the scale of grand unified theories, $E_{\text{GUT}} \sim 10^{16}$ GeV. This unification suggests that the MSSM provides a description of nature up to E_{GUT} . Thus, it is useful to consider the set of “boundary” conditions at the scale E_{GUT} given by:

$$\begin{aligned} g_{\text{GUT}} &\equiv g_1 = g_2 = g_3, \\ m_{1/2} &\equiv M_1 = M_2 = M_3, \\ m_0^2 &\equiv m_X^2 = m_{H_u}^2 = m_{H_d}^2, \\ A_0 &\equiv A_t = A_b = A_\tau. \end{aligned} \quad (2.17)$$

A model of MSSM that includes the above assumptions is referred to as an mSUGRA model. These models can be more easily parameterized by the vastly reduced set of variables $\{m_0, m_{1/2}, A_0, \tan\beta, \text{sign}(\mu)\}$, where μ is the superpotential

parameter in Eq. 2.13. While this simplification is often useful for studying a specific realization of the MSSM, we will instead be considering models with even simpler phenomenologies. The reason for this will be clear in Sec. 2.2.6, where we introduce the simplified model spectra.

2.2.4 Natural SUSY

With the inclusion of supersymmetric particles, the quadratically divergent nature of the corrections to the Higgs mass is removed. However, the SUSY-breaking mass terms can affect this cancellation and re-introduce a certain amount of fine-tuning to the corrections. One can ask how large the sparticle masses can be in order to sufficiently satisfy the “no-fine-tuning” condition. The necessary conditions become [4–6]:

- $m_{\tilde{t}_1, \tilde{t}_2, \tilde{b}_L} \sim 500 \text{ GeV}$
- $m_{\tilde{g}} \lesssim 1.5 \text{ TeV}$
- $\mu \lesssim 250 \text{ GeV}$

The last condition translates to an upper bound of $\sim 350 \text{ GeV}$ on a subset of the neutralinos and charginos. Models that satisfy this set of constraints are referred to as “natural” SUSY models. It is clear that gluinos and third-generation squarks therefore provide a direct measure of the level of fine-tuning needed if the MSSM is realized in nature. Of primary experimental interest in a natural SUSY scenario is the presence of collision events with multiple b -quarks produced from the decay of the gluinos and third-generation squarks. We discuss this feature in the next section.

2.2.5 Gluino and squark production

The production of gluinos and squarks occur, at a hadron collider, predominantly through the strong interactions. Their rate of production can therefore be very large compared to sparticles that are produced only through the electroweak interactions. Due to R -parity conservation, squarks and gluinos are produced in pairs. Gluino-pair production occurs via the leading order Feynman diagrams shown in Fig. 2.1, while squark-pair production occurs through the diagrams in Fig. 2.2. The relative production rates of $\tilde{g}\tilde{g}$ and $\tilde{q}\tilde{q}$ depend on the ratio of masses of the gluino and squarks. In addition, the associated production of a gluino with a squark can also be significant. Fig. 2.3 shows the next-to-leading order cross sections at $\sqrt{s} = 7$ TeV for gluino-pair production in a “simplified” model (discussed below) where the squarks have been decoupled ($m_{\tilde{q}} \gg m_{\tilde{g}}$). The cross section for $\tilde{g}\tilde{g}$ production is on the order of 0.01 pb in this model. Fig. 2.3 also shows the top-squark-pair production cross section in a model with the gluino and all other squarks decoupled. In the top-squark mass range shown, $\tilde{t}\tilde{t}$ pairs are produced with a cross section of about 0.01 to 0.1 pb.

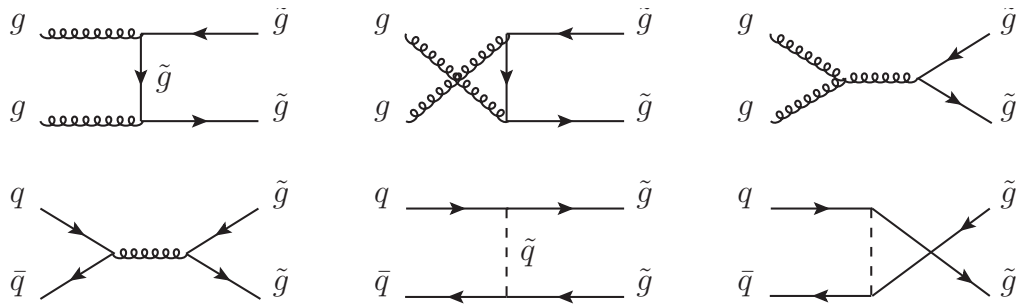


Figure 2.1: Leading order Feynman diagrams for gluino-pair production in hadron collisions.

The gluino, if sufficiently heavy, will predominantly decay to a squark-quark pair $\tilde{g} \rightarrow \tilde{q}q_{L/R}$. For third-generation squarks, the gluino decays to the corre-

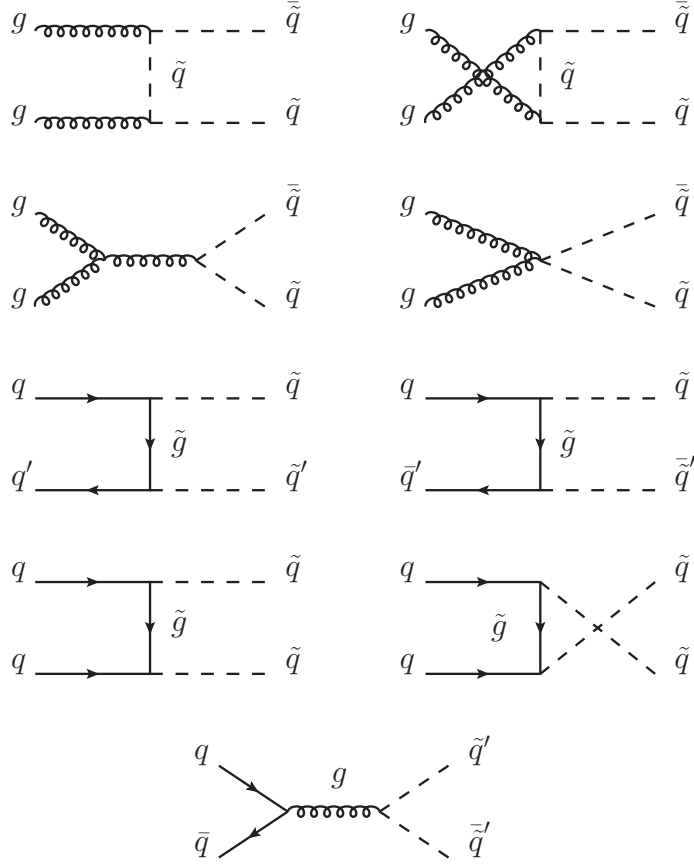


Figure 2.2: Leading order Feynman diagrams for squark-pair production in hadron collisions.

sponding mass eigenstates $\tilde{g} \rightarrow \tilde{t}_{1,2}$ and $\tilde{g} \rightarrow \tilde{b}_{1,2}$. If the squarks are heavier than the gluino, then the dominant decay mode would be the three-body decay $\tilde{g} \rightarrow q\bar{q}\tilde{\chi}_i^0$ or $\tilde{g} \rightarrow qq'\tilde{\chi}_i^\pm$ via a virtual squark. Squarks decay predominantly to a gluino-quark pair $\tilde{q} \rightarrow \tilde{g}q$, if it is kinematically accessible. Otherwise, squarks will decay via $\tilde{q} \rightarrow q\tilde{\chi}_i^0$ or $\tilde{q} \rightarrow q'\tilde{\chi}_i^\pm$. Third-generation squarks may have large Yukawa interaction terms and thus several other possible decay modes. For example, decays to Higgs bosons $\tilde{b}_{1,2} \rightarrow H^-\tilde{t}_{1,2}$ or $\tilde{b}_2 \rightarrow \{h^0, H^0, A\}\tilde{b}_1$ can occur if accessible. In addition, because of their large mixing, both mass eigenstates of the third-generation squarks can decay to charginos and W bosons. This is in contrast to the other two generations, where right-handed squarks have no

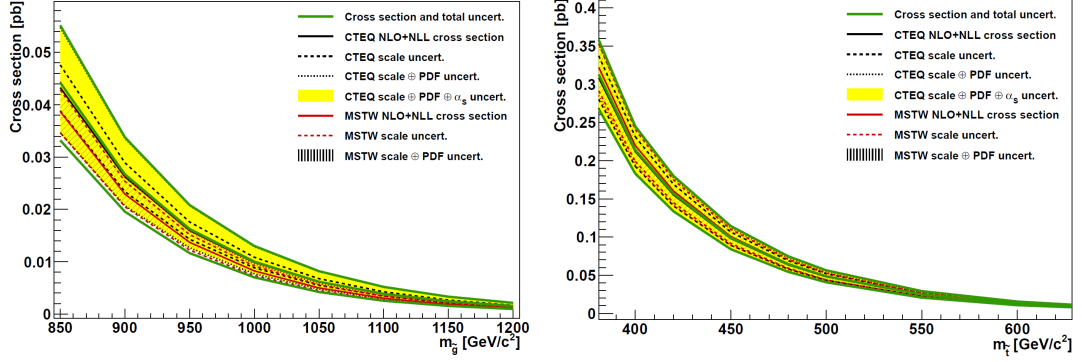


Figure 2.3: Gluino-pair (left) and top-squark-pair (right) production cross section at $\sqrt{s} = 7$ TeV as a function of $m_{\tilde{g}}$ and $m_{\tilde{t}}$, respectively [7]. The green lines give the computed central value and total uncertainty. Also shown in the plots are the cross section values and uncertainties when computed using two different sets of parton distribution functions (CTEQ and MSTW).

couplings to charginos. In the case of top squarks, if the above modes are all kinematically forbidden, the suppressed modes $\tilde{t}_1 \rightarrow c\tilde{\chi}_1^0$ or $\tilde{t} \rightarrow bf\tilde{f}'\tilde{\chi}_1^0$ may dominate, where f are light SM fermions that couple to the W boson. Since these modes are strongly suppressed, the decay would be relatively slow, which would make the top squark quasi-stable from the point of view of a collider signature.

2.2.6 Simplified model spectra

A specific realization of the MSSM can contain a large number of accessible sparticle production and decay modes, giving rise to a multitude of experimental topologies. Since there exists a very large parameter space of models within the MSSM (even for the more constrained mSUGRA models), it is often difficult to make generic statements about the results of a particular search based on the interpretation from a single model. Therefore, we introduce a set of sim-

plified model spectra (SMS) [8], each of which consists of a small number of kinematically accessible sparticles and a fixed sequence of sparticle production and decay. These models offer the advantage of establishing the sensitivity of a search towards a specific feature of new physics and providing a straightforward interpretation without being overly model-dependent. The first two simplified models we consider consist exclusively of gluino-pair production, where the squarks in the model are decoupled ($m_{\tilde{q}} \gg m_{\tilde{g}}$). We impose that the gluinos decay exclusively via $\tilde{g} \rightarrow b\bar{b}\tilde{\chi}_1^0$ in the first model and $\tilde{g} \rightarrow t\bar{t}\tilde{\chi}_1^0$ in the second model, as illustrated in Fig. 2.4. We will use the short-hand notation $\tilde{g}\tilde{g} \rightarrow bbbb$ and $\tilde{g}\tilde{g} \rightarrow tttt$ (omitting the LSP's) when referring to these models. We consider a third simplified model consisting of top-squark-pair production, where the top-squark decays exclusively to $\tilde{t} \rightarrow t\tilde{\chi}_1^0$. In this model, the gluino and all other squarks are effectively decoupled. An illustration of this process is shown in Fig. 2.5. We will use the notation $\tilde{t}\tilde{t} \rightarrow tt$ for this model.

In events with pair-produced gluinos or squarks, one expects to find as decay products high-momentum quarks, which form hadronic jets (Sec. 4.5). Moreover, in the above simplified models, many (if not all) of the quarks will be b -quarks. Finally, the pair of stable LSP's, which in many scenarios are weakly-interacting neutralinos, will escape detection and manifest themselves as an apparent momentum imbalance in a collision event. Hence, in the $\tilde{g}\tilde{g} \rightarrow bbbb$, $\tilde{g}\tilde{g} \rightarrow tttt$, and $\tilde{t}\tilde{t} \rightarrow tt$ models, one expects to find events with a large amount of visible energy, a large number of b -quarks, and a significant momentum imbalance. This observation forms the basis of the selection of events in the search presented in Chapter 5.

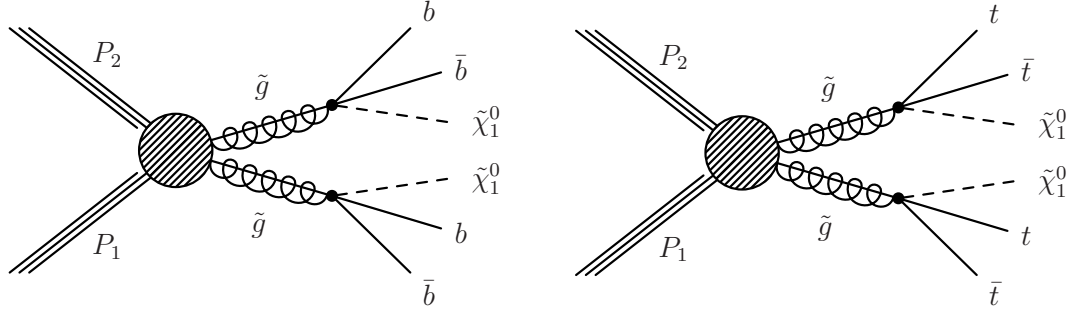


Figure 2.4: Simplified model of gluino-pair production with $BR(\tilde{g} \rightarrow b\bar{b}\tilde{\chi}_1^0) = 100\%$ (left) or $BR(\tilde{g} \rightarrow t\bar{t}\tilde{\chi}_1^0) = 100\%$ (right) [9]. We denote the left model as $\tilde{g}\tilde{g} \rightarrow b\bar{b}b\bar{b}$ and the right model as $\tilde{g}\tilde{g} \rightarrow t\bar{t}t\bar{t}$.

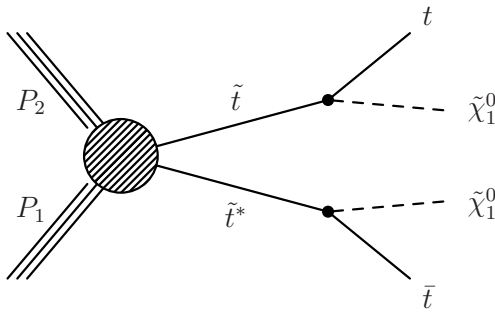


Figure 2.5: Simplified model of top-squark-pair production with $BR(\tilde{t} \rightarrow t\tilde{\chi}_1^0) = 100\%$ [9]. We denote this model as $\tilde{t}\tilde{t} \rightarrow tt$.

CHAPTER 3

ACCELERATOR AND DETECTOR

The Large Hadron Collider (LHC) [10] is the largest particle accelerator to date. Located in a 27-km-circumference tunnel under the French-Swiss border at CERN, the LHC is designed to collide protons at a center-of-mass energy of $\sqrt{s} = 14 \text{ TeV}$, a seven-fold increase in energy with respect to previous hadron colliders. Two large-scale, general-purpose detectors have been built to observe and record the collisions. One of them is the Compact Muon Solenoid (CMS) detector [11], located in Cessy, France, at the northern end of the LHC tunnel. In this chapter, we review the basic properties of the LHC and give an overview of the CMS detector.

3.1 The Large Hadron Collider

The LHC consists of two counter-rotating proton beams housed in a single magnet system. The superconducting dipole magnets provide a B -field of up to 8.3 T to keep the path of 7 TeV protons within the circular tunnel. A total of 1 232 dipole magnets are placed along the tunnel. In addition, there are 392 quadrupole magnets that focus the proton beams at various points in the ring.

The LHC is part of the CERN accelerator complex, shown in Fig. 3.2. Protons are obtained by stripping electrons from hydrogen atoms using an ion source. The protons are collected and sent to the linear accelerator Linac2, where they are accelerated to an energy of 50 MeV. The protons are subsequently fed to the PS Booster, where they are accelerated to 1.4 GeV. From there, they are sent

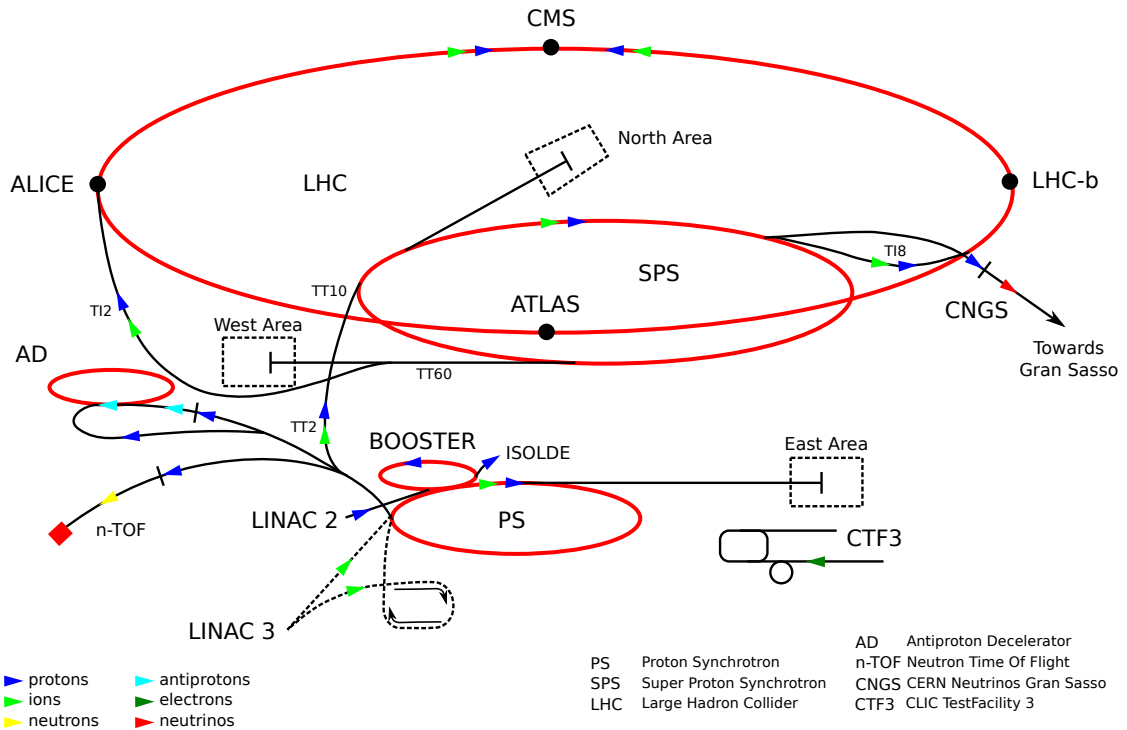


Figure 3.1: The CERN accelerator complex (not to scale) [12]. Shown on the LHC ring are the four main experiments: ATLAS, CMS, ALICE, and LHCb.

to the 628-m-circumference Proton Synchrotron, where they are further accelerated up to 26 GeV. The protons are then fed to the 7-km-circumference Super Proton Synchrotron, where they are boosted up to an energy of 450 GeV. Finally, they are injected into the LHC tunnel, where they can reach a maximum design energy of 7 TeV. In 2011, the maximum proton energy was 3.5 TeV.

The acceleration of protons is achieved in each part of the PS→SPS→LHC chain by the use of radio-frequency (RF) cavities. Protons traveling around the LHC ring at a frequency that is an integer factor of the RF system are accelerated each time they pass through the electric field of an RF cavity. The oscillating electric field induces a “bunching” structure to the beam, such that the protons

become grouped into discrete packets called bunches. Near the end of 2011, a total of 1 380 bunches were circulated in each beam, 1 331 of which were set up to collide at various points in the LHC ring. The bunches were separated in time by 50 ns.

Protons injected into the LHC ring at a slight angle with respect to the nominal orbit path will traverse the ring with a center of orbit slightly shifted relative to the nominal orbit. Such protons will thus be slightly displaced relative to the nominal orbit position, and the size of the displacement will depend on the position s along the ring. This displacement is referred to as the betatron amplitude $\beta_p(s)$ of the proton. We denote the maximum displacement out of all protons within a bunch as $\beta(s)$. The average spread in the injection angles of the protons within a bunch is characterized by the transverse emittance ε , and the average transverse size of the beam at a position s is $\sigma(s) = \sqrt{\beta(s)\varepsilon}$. Typically, the normalized transverse emittance $\varepsilon_n = \gamma\beta\varepsilon \sim \gamma\sigma(s)^2/\beta(s)$, where γ and β are the relativistic terms (assuming $\beta \sim 1$), is used instead to characterize the angular spread of the beam as it is independent of the beam energy.

The instantaneous luminosity of the two proton beams at the interaction point (IP) is given by

$$\mathcal{L} = \frac{f_{rev}n_bN_p^2}{4\pi\sigma^{*2}}F = \frac{\gamma f_{rev}n_bN_p^2}{4\pi\varepsilon_n\beta^*}F \quad (3.1)$$

where N_p is the number of protons per bunch, n_b the number of bunches per beam, $f_{rev} = 11246$ Hz the revolution frequency of the protons, γ the relativistic factor, σ^* the transverse RMS beam size at the IP, β^* the betatron amplitude at the IP, ε_n the normalized transverse emittance of the beam, and $F \lesssim 1$ a reduction factor arising from the non-zero crossing angle of the beams at the IP. A comparison of the values of each parameter between the design specification

and the values achieved in 2011 are given in Table 3.1. At design performance, the LHC provides a peak luminosity of $\mathcal{L} = 10^{34} \text{ cm}^{-2}\text{s}^{-1}$.

Table 3.1: LHC beam parameters at design performance and at the end of 2011.

Parameter	Design	End of 2011
Collision energy [TeV]	14	7
Bunch spacing [ns]	25	50
Number of colliding bunches (n_b)	2 808	1 331
Number of protons per bunch (N_p)	1.1×10^{11}	1.5×10^{11}
Betatron amplitude at IP (β^*) [cm]	50	10, 15
Normalized transverse emittance (ε_n) [$\mu\text{m}\text{-rad}$]	3.75	2-3.5
Peak instantaneous luminosity (\mathcal{L}) [$\text{cm}^{-2}\text{s}^{-1}$]	1×10^{34}	4×10^{33}
Mean interactions/crossing (at peak lumi.)	22	19

Over time, the luminosity of the beam decreases as the protons collide and are lost from the bunches. The total number of events N produced from a process with cross-section σ over a given time period $[t_0, t_1]$ is thus

$$N = \sigma \cdot \int_{t_0}^{t_1} \mathcal{L}(t) dt. \quad (3.2)$$

We refer to $L = \int_{t_0}^{t_1} \mathcal{L}(t) dt$ as the integrated luminosity. A total integrated luminosity of $L = 6.13 \times 10^{-39} \text{ cm}^{-2} = 6.13 \text{ fb}^{-1}$ was delivered by the LHC in 2011.

The total pp cross-section at the LHC collision energy is roughly $\sigma_{total} \sim 100 \text{ mb}$. A large fraction of this cross-section is due to inelastic scattering events ($\sigma_{inelastic} \sim 70 \text{ mb}$), which can be easily observed by the detector. The average number μ of such interactions per bunch crossing is estimated as

$$\mu = \sigma_{inelastic} \cdot \mathcal{L} \cdot R_{bunch}, \quad (3.3)$$

where $R_{bunch} = 50$ ns/bunch-crossing is the bunch spacing. Assuming the peak luminosity of 2011, $\mathcal{L} = 4 \times 10^{33}$ cm⁻²s⁻¹, we find that there are roughly $\mu \sim 19$ interactions per bunch crossing. We refer to interactions of this type as “pile-up” interactions, since they will tend to be produced in concurrence with and superposed over any other rare hard-scatter collision of interest.

3.2 The Compact Muon Solenoid Detector

The CMS detector is a general-purpose detector built to observe a wide variety of physics phenomena at the TeV energy scale. With the goal of discovering rare processes like the production of the Higgs boson or other new-physics phenomena, the detector must be capable of providing high lepton identification efficiency and precise track position and momentum measurement, while giving high rejection power to the overwhelming background from QCD processes. Moreover, to infer the presence of energetic neutrinos or other weakly-interacting particles, the detector must be nearly hermetic.

The CMS detector is constructed in a 15-m-diameter cylindrical geometry and spans a length of 21 m. An illustration of the CMS detector is shown in Fig. 3.2. The large size of the detector is needed to absorb the energetic particles created by the LHC collisions. The detector features a superconducting solenoid, which provides a magnetic field of 3.8 T. Within the volume of the solenoid are the silicon pixel and strip tracker systems, the crystal electromagnetic calorimeter, and the brass/scintillator hadron calorimeter. Outside of the solenoid are muon detectors consisting of drift tubes, cathode strip chambers, and resistive plate chambers. The forward hadron calorimeter extends the

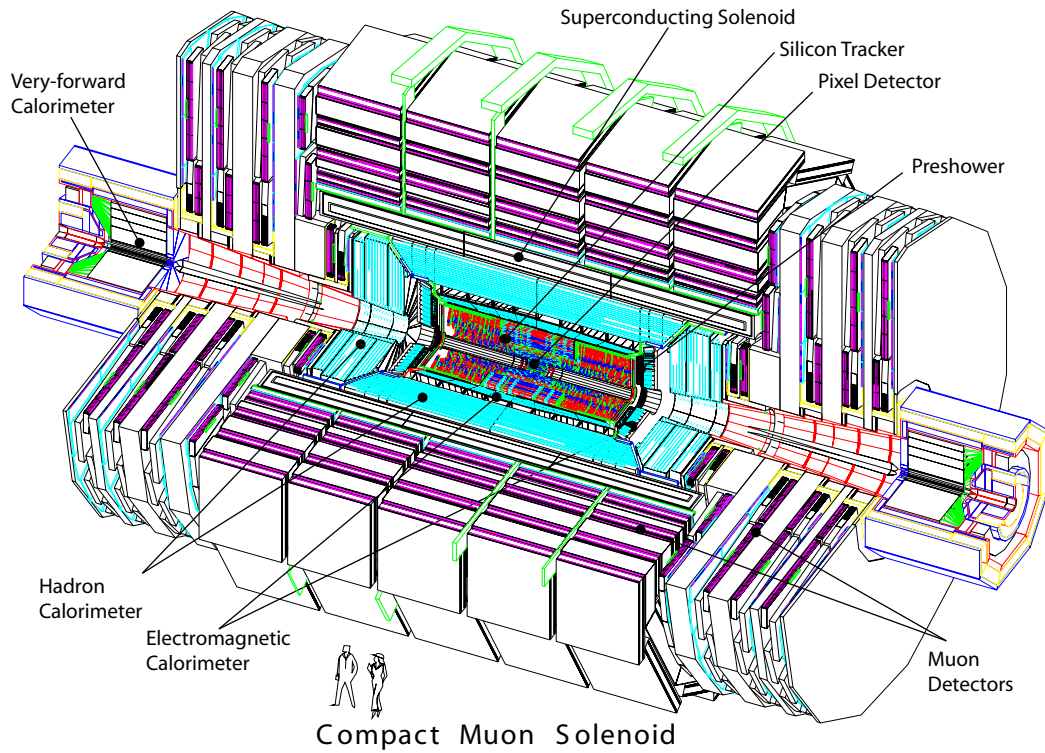


Figure 3.2: Perspective view of the CMS detector.[13]

pseudorapidity coverage (defined below) of the detector up to $|\eta| < 5.2$. Located 100 m underground, the CMS detector is naturally shielded from external sources of radiation such as cosmic rays.

We use a right-handed coordinate system with the nominal collision point at the origin, the positive x direction pointing towards the center of the LHC ring, and the positive y direction pointing upwards (perpendicular to the LHC plane). The positive z direction points in the counter-clockwise direction of the ring (when looking from above). The azimuth angle ϕ is defined in the x - y plane, beginning from the positive x -axis. The polar angle θ is measured from the positive z -axis. We define the pseudorapidity as $\eta = -\ln(\tan(\theta/2))$.

3.2.1 Solenoid magnet

A key component of the CMS detector is the superconducting solenoid magnet, which provides a B -field of 3.8 T. The strong magnetic field is required to provide sufficient bending power to measure the momenta of charged particles to the desired level of accuracy. The 2180-turn magnet coil spans a length of 12.5 m and a diameter of 6 m. With a current of 18 kA, the magnet stores a total magnetic energy of 2.1 GJ and is cooled to a temperature of 5 K. Weighing 12 kt, the magnet forms the bulk of the total 12.5 kt mass of the CMS detector. The magnet coil surrounds the tracker and calorimeter systems, while the return field is channeled through a 12-sided iron structure (“yoke”) interleaved with muon detectors. The iron yoke also acts as a filter (hadron absorber) for the muon detectors.

3.2.2 Tracker systems

The tracker system provides an accurate measurement of the trajectories and momenta of charged particles and allows for the efficient reconstruction of secondary vertices from the decay of heavy-flavor hadrons. In addition, it must have a fast response to disentangle particle tracks of collisions from neighboring bunch crossings. However, as the closest detector element to the interaction point, the tracker system must also be able to withstand large amounts of radiation over the lifetime of the experiment. The large particle flux near the collision point necessitates detectors with high granularity in order to avoid degradation in the track reconstruction efficiency. To satisfy the above constraints, CMS employs an all-silicon tracker with a total sensitive area of 200 m². The tracker

combines fast response time, excellent spatial resolution, and low occupancy with a radiation-hard design.

The CMS tracker system is comprised of an inner pixel detector and an outer silicon microstrip detector. The tracker system spans a total length of 5.6 m, extends to a radius of 1.1 m, and covers a pseudorapidity range of $|\eta| < 2.5$.

Pixel Tracker

The pixel tracker system is composed of three barrel layers and two endcap disks on either side of the barrel layers. A view of the pixel tracker is shown in Fig. 3.3. The barrel layers are 53 cm in length and have radii of 4.4 cm, 7.3 cm, and 10.2 cm. The layers are segmented into modules, which contain silicon pixel sensors connected to read-out chips via bump-bonds. Each read-out chip serves a 52×80 array of pixels. The two-dimensional array of pixels across three barrel layers provide a 3D reconstruction of the particle track. There are a total of 672 (96) full modules (half modules) in the barrel region, each containing 16 (8) read-out chips. This gives a total of 48 million pixels in the barrel region. Because the B -field of the solenoid magnet is oriented perpendicular to the electric field of the depleted region in the silicon sensors, the electron-hole pairs will tend to drift and be collected across several neighboring pixels. The distribution of charge across pixels permits the computation of the center of gravity of the total charge, which results in an improved position resolution.

The endcap disks are located at $|z| = 35.5$ cm and $|z| = 48.5$ cm, and are arranged in a “turbine” geometry with 24 trapezoidal blades and 7 modules per blade. The blades are arranged to give hermetic coverage and are tilted at an

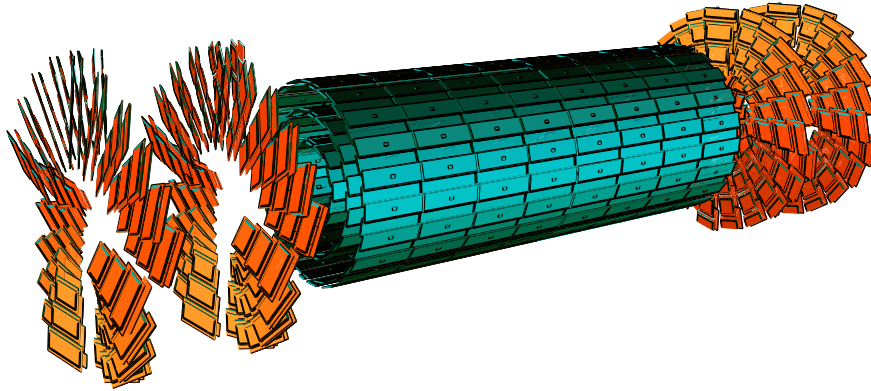


Figure 3.3: Perspective view of pixel tracker [14]. Each rectangular unit in the barrel layers is a pixel module.

angle of 20° to accommodate the sharing of charges among neighboring pixels. The sensors on each blade are grouped into arrays of various sizes called plaquettes. There are a total of 672 plaquettes in the endcap detectors, giving a total of 18 million pixels.

Each pixel sensor covers an area of $100\mu\text{m} \times 150\mu\text{m}$ and has a thickness of $285\mu\text{m}$ ($270\mu\text{m}$) in the barrel (endcap) detector. The pixel size was chosen small enough so that the occupancy at design luminosity is roughly 10^{-4} per pixel per bunch crossing. The hit resolution of the pixels has been measured to be about $\sim 20\mu\text{m}$ in the r - ϕ coordinate and $\sim 30\mu\text{m}$ in the z coordinate, while the hit efficiency is greater than 99% across the entire detector.

Silicon Strip Tracker

The silicon strip tracker (SST) surrounds the pixel system, covering a radial distance of $20\text{ cm} < r < 110\text{ cm}$. The SST is divided into four sub-detectors. The tracker inner barrel (TIB) consists of 4 cylindrical layers with a length of $|z| < 55\text{ cm}$. The silicon strips are aligned axially to measure the r - ϕ coordi-

nate. The first two layers consist of double-sided strip modules, which have a 100 mrad angle with respect to each other to allow a measurement of the z coordinate. The tracker outer barrel (TOB) is comprised of 6 layers and extends the coverage to $|z| < 118$ cm. The inner two layers of the TOB consist of double-sided modules. Each of the two tracker inner disk (TID) detectors consists of 3 disks, which are each segmented to form 3 concentric rings. The two innermost rings in each layer consist of double-sided modules. The tracker endcap (TEC) occupies the region of $124 \text{ cm} < |z| < 282 \text{ cm}$ and is made with 9 disks on either side, each disk segmented into 8 petals. The petals contain both double-sided and single-sided modules. The layout of the tracker system is shown in Fig. 3.4.

The silicon sensors have thicknesses of either $320 \mu\text{m}$ or $500 \mu\text{m}$ and a strip pitch ranging from $80 \mu\text{m}$ to $205 \mu\text{m}$, depending on the barrel/disk layer. Strip lengths vary from 10 cm to 20 cm; the higher noise due to longer strips in the outer layers is compensated by using thicker sensors. Strip sensors have an occupancy of a few percent per strip per bunch crossing at design luminosity, and a hit resolution ranging from $15 \mu\text{m}$ to $40 \mu\text{m}$. The hit efficiency of the strip modules is greater than 99%. The resolution of the transverse and longitudinal impact parameter of reconstructed tracks in the tracker system (including the pixel tracker) is $\sim 20 \mu\text{m}$ and $\sim 40 \mu\text{m}$, respectively.

3.2.3 Calorimeter systems

Electromagnetic Calorimeter

Electrons and photons produced from the LHC collisions will have typical energies of at least a few hundred MeV. In this energy regime, an electron trav-

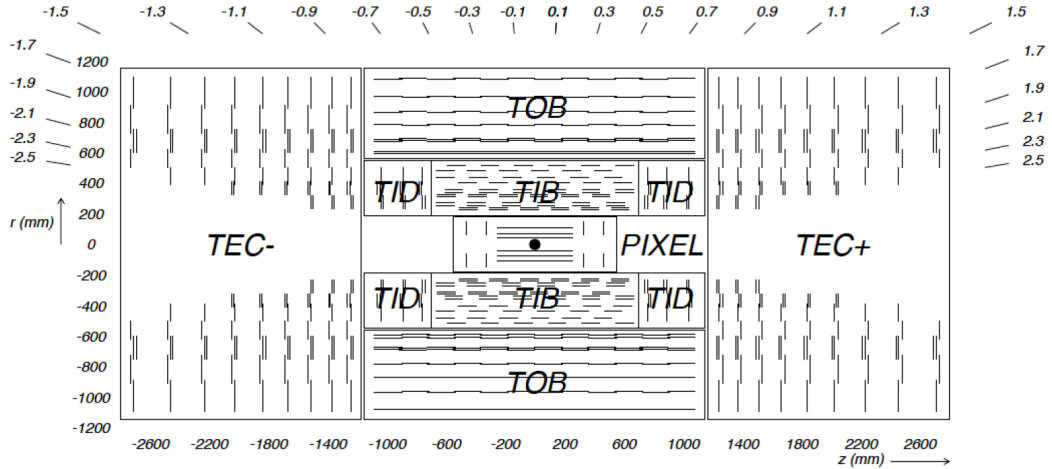


Figure 3.4: Schematic (r - z) view of the pixel and silicon strip tracker systems [15].

eling through matter will lose the majority of its energy through the process of bremsstrahlung, while photons will experience energy loss predominantly through the process of pair-production. In either case, the secondary photon or electron-positron pair will subsequently make an e^+e^- pair of its own or radiate more photons, respectively. This process continues until the energies of the particles reach the critical energy of the material. The resulting cascade of particles is an electromagnetic shower. The depth of the shower is characterized by the radiation length X_0 of the material, which is defined through the relation

$$-\frac{dE}{dx} = \frac{E_0}{X_0}, \quad (3.4)$$

where E_0 is the energy of the incident electron/photon and x is the thickness of the material. The lateral spread in the shower, caused by multiple scattering of the electrons away from the shower axis, is characterized by the Molière radius R_M . Approximately 90% of the total energy from the shower is contained within $1 R_M$.

The CMS electromagnetic calorimeter (ECAL) comprises of a homogenous

calorimeter in the barrel and endcap regions, together with an additional sampling calorimeter in the endcap region. The total pseudorapidity coverage of the ECAL is $|\eta| < 3$. Lead tungstate (PbWO_4) scintillation crystals are used in the barrel and endcap detectors. The main advantages of lead tungstate are its fast response time and high radiation resistance. Moreover, the material has a short radiation length ($X_0 = 8.9$ mm) and small Molière radius ($R_M = 22$ mm). The crystal dimensions were chosen to encompass most of the lateral and longitudinal spread of an electromagnetic shower. They have a front face of 22×22 mm (29×29 mm) and a length of 230 mm (220 mm) in the barrel (endcap) regions, which corresponds to the dimensions $1R_M \times 1R_M \times 26X_0$ ($1.3R_M \times 1.3R_M \times 25X_0$). The crystals are shorter in the endcap region due to the presence of the preshower detectors, which we describe below.

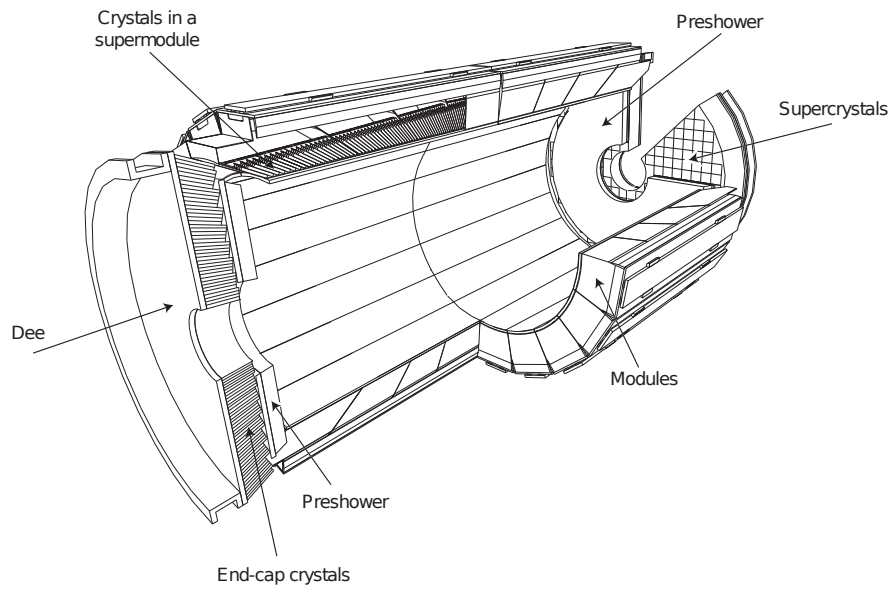


Figure 3.5: Layout of the CMS electromagnetic calorimeter [16]. Shown are the supermodules of the barrel region, the Dees of the endcap regions, and the preshower detectors. The division of the supermodules into 4 modules and the crystals within a supermodule/Dee are also shown.

An illustration of the ECAL is shown in Fig. 3.5. The ECAL is divided into three components: the barrel, endcap, and preshower detectors. The barrel component (EB) provides coverage in the region $|\eta| < 1.479$ and has an inner radius of 129 cm. Crystals in the barrel region are grouped into modules, with each module consisting of 400 to 500 crystals. A set of four modules makes up a “supermodule”. There are 18 supermodules in each of the two ϕ -halves of the barrel detector. Each supermodule contains 1700 crystals, giving a total of 61200 crystals in the barrel region. The crystals are aligned projectively (i.e. with the front face towards the nominal collision point), but with a slight 3° tilt to prevent efficiency loss due to cracks in the crystal coverage. Each crystal provides an angular coverage of 0.0174×0.0174 in η - ϕ .

The two endcap calorimeters (EE) provide a coverage of $1.479 < |\eta| < 3$, and are each divided into two “Dees”. Each Dee is a semicircular aluminum plate containing blocks of 5×5 crystals. A total of 3662 crystals are contained in each Dee.

The ECAL preshower detectors (ES), which are positioned in front of the EE crystals, cover a region of $1.7 < |\eta| < 2.6$. Each detector is a sampling calorimeter with two sets of lead absorber and silicon strip sensor layers. The material thickness of the lead is $2X_0$ ($1X_0$) in the first (second) layer. The task of the ES is to distinguish between photons produced directly from the collision and photons produced via neutral pion decays, $\pi^0 \rightarrow \gamma\gamma$. In the latter process, the pair of closely spaced photons is more easily resolved with the finer granularity of the ES.

The low scintillation light yield of lead tungstate (~ 100 photons/ MeV) for the EB and EE detectors requires the use of photodetectors with large ampli-

fication capabilities. Moreover, since the ECAL is placed within the magnet solenoid, the photodetectors must be able to operate in a strong B -field. In the barrel region, silicon avalanche photodiodes (APDs) are used due to their compactness, high gain (50 \times), low sensitivity to magnetic fields, and high radiation resistance. APDs achieve a quantum efficiency of 75% at 439 nm. In the endcap regions, vacuum phototriodes (VPT's) are used to combat the increased radiation background. Each VPT consists of a 25-mm-diameter copper mesh anode placed between a cathode and a dynode. The VPT's operate at about 22% quantum efficiency at 430 nm with a gain of 8 to 10.

The energy resolution of the ECAL is determined by several factors. The first is a stochastic term arising from the proportionality of the particle energy to the number of scintillation photons produced: $\sigma/E \propto \sqrt{E}/E = 1/\sqrt{E}$. A second factor due to the noise in the ECAL is largely independent of the energy: $\sigma/E \propto 1/E$. Finally, calibration errors, leakage, and crystal non-uniformity result in a fraction of the incident energy that is not measured. This term is proportional to the incident energy and is the dominant factor at higher energies. The total energy resolution in the barrel region is [17]:

$$\frac{\sigma}{E} = \frac{2.8\%}{\sqrt{E} [\text{GeV}]} \oplus \frac{0.415 \text{ GeV}}{E} \oplus 0.3\%, \quad (3.5)$$

where the terms on the right are added in quadrature.

Hadron Calorimeter

The interaction of a hadron with matter can be described in a manner similar to the case of electromagnetic interactions. The interaction typically leads to a hadronic shower of particles. In this case, however, the characteristic depth of

the shower is the nuclear interaction length λ_I . Hadronic showers are comprised of two components, the electromagnetic part (induced by π^0 decays) and the hadronic part (π^\pm, n , etc.). The lateral size of a hadronic shower is characterized by a core shape of size R_M , determined from the electromagnetic component of the shower, and an additional tail in the distribution caused by the hadronic component.

The CMS hadronic calorimeter (HCAL) consists of four distinct detectors: the barrel (HB) and endcap (HE) calorimeters, the outer calorimeter (HO), and the forward calorimeter (HF). An illustration of each component of the HCAL is shown in Fig. 3.6.

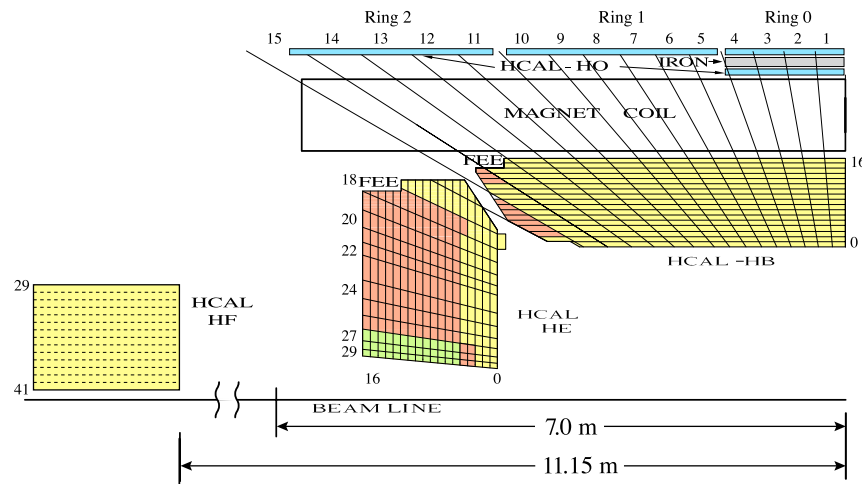


Figure 3.6: Quarter-slice view (in the r - z plane) of the CMS hadronic calorimeter [18]. The lines in η delimit the HCAL towers. “FEE” refers to the location of the Front End Electronics. The different colors indicate the grouping of scintillator layers in the longitudinal readout.

The barrel and endcap detectors are sampling calorimeters with alternating layers of brass absorber and plastic scintillator. Brass is chosen as the absorber for its high stress tolerance and short interaction length of $\lambda_I = 16.4$ cm. More-

over, brass is a non-magnetic material — an important property as the HB and HE are positioned within the solenoid magnet. The barrel and endcap regions have a pseudorapidity coverage of $|\eta| < 1.4$ and $1.3 < |\eta| < 3.0$, respectively. The HB covers a radial distance of $177 \text{ cm} < r < 295 \text{ cm}$ and consists of 18 wedges in ϕ , each subtending 20° . There are a total of 17 layers of 3.7-mm-thick plastic scintillators sandwiched in between 50-mm-thick brass absorbers. The first and last absorbers are made with stainless steel for structural strength. The plastic scintillators are segmented into tiles. Groups of tiles, one from each layer, form projective “towers”, each covering an angular area $\Delta\eta \times \Delta\phi = 0.087 \times 0.087$. A single tower encompasses most of a hadron shower at a given angle. The HE also consists of 18 ϕ -wedges and is similarly segmented into 14 towers of angular area $\Delta\eta \times \Delta\phi = 0.087 \times 0.087$ (0.175×0.175) in the region $|\eta| < 1.6$ ($|\eta| > 1.6$), with one tower partially shared with the HB. There are 19 active layers between 79-mm-thick brass layers in the HE. The total interaction length of the HB and HE (including the ECAL) is about $10\lambda_I$.

The outer hadron calorimeter lies outside of the magnet coil and covers a range of $|\eta| < 1.26$. It serves to provide extra layers of scintillation to capture the leakage of long or late-starting hadron showers. The HO is divided into 5 rings in η of 30° ϕ -sectors, following the segmentation of the muon barrel system. The central ring consists of two layers of 1-cm-thick scintillating tiles on either side of a 19.5-cm-thick iron slab. All other rings contain a single layer of scintillator. The magnet coil is used as an additional absorber of at least $1.4\lambda_I$, extending the interaction length of the calorimeters to a total of $11.8\lambda_I$.

The HB, HE, and HO detectors employ hybrid photodiodes (HPD) to convert optical signals to electronic output. HPD’s have the advantage of operating

within a high magnetic field and can provide the necessary large signal amplification ($\sim 2000\times$) through their silicon-based design.

The forward calorimeters are located at a distance of $|z| = 11.2$ m from the nominal interaction point and have a coverage of $3.0 < |\eta| < 5.2$. They comprise of a steel absorber embedded with radiation-hard quartz fibers, which generate signals through Cherenkov radiation. The fibers are aligned parallel to the beam axis in 5-mm separation. The signal is channeled to conventional photomultiplier tubes behind thick shielding. Each HF detector is segmented into 13 rings of 18 wedges, forming towers in $\Delta\eta$ and $\Delta\phi$ with typical sizes of 0.175×0.175 .

The response of the HCAL to the electromagnetic component of a hadronic shower is different from its response to the hadronic component. This property limits the energy resolution of the HCAL due to several effects. Firstly, the fraction of the total hadron energy carried by the electromagnetic component can be substantial (as high as 70%) and can fluctuate greatly from one shower to the next. Secondly, a significant fraction of the energy of the hadronic component can be used for nuclear recoil or for breaking up nuclei, or can be carried away by neutrinos and muons from decays in flight. This component, which is “invisible” to the calorimeter, can also fluctuate greatly from one shower to the next. These effects limit the precision to which the energy of a typical hadron shower can be determined.

The energy resolution of the HCAL is ECAL-dependent, since in most cases the hadron shower begins in the ECAL. The energy resolution is broken into two components — a stochastic and a constant term. The combined ECAL+HCAL resolution is [19; 20]

$$\frac{\sigma}{E} = \frac{a}{\sqrt{E [\text{GeV}]}} \oplus b, \quad (3.6)$$

where $a = 0.85 \text{ GeV}^{\frac{1}{2}}$ ($1.98 \text{ GeV}^{\frac{1}{2}}$) and $b = 0.07$ (0.09) in the HB/HE (HF) regions.

3.2.4 Muon systems

Most of the muons produced from the proton collisions at the LHC have energies in the minimum-ionization regime. They are therefore able to pass through the tracker and calorimeter systems while losing a minimal amount of energy. Detectors sensitive to charged particles and that are placed outside of the solenoid magnet can therefore be used to identify muons exiting the inner detectors. Moreover, the momenta of tracks in the muon systems can be inferred entirely from the return solenoid field present outside of the magnet coil.

CMS employs three kinds of gas-ionization detectors for muon detection. Due to the wide area of detection ($25\,000 \text{ m}^2$) needed to cover the solenoid, the muon system must be inexpensive and robust. In the barrel region, where the rate of muons is relatively low and where the B -field is mostly contained in the return yoke, standard drift-tube chambers (DT) are employed. In the endcap region, where muon (and background) rates are high and the B -field is large and non-uniform, cathode strip chambers (CSC) are used instead. A third detector system, consisting of resistive plate chambers (RPC), is used to provide very fast response times and to give a useful redundancy in the reconstruction of the muon trajectory.

The drift-tube chamber system, shown in Fig. 3.7, consists of four concentric cylinders sandwiched between the return yoke of the magnet. Each cylinder is divided into 5 wheels with 12 sectors each. For the inner three cylinders, there is one drift chamber per sector, while for the outermost cylinder, the top-most

and bottom-most sectors consist of two chambers. In total, there are 250 drift tube chambers, providing a pseudorapidity coverage of $|\eta| < 1.2$.

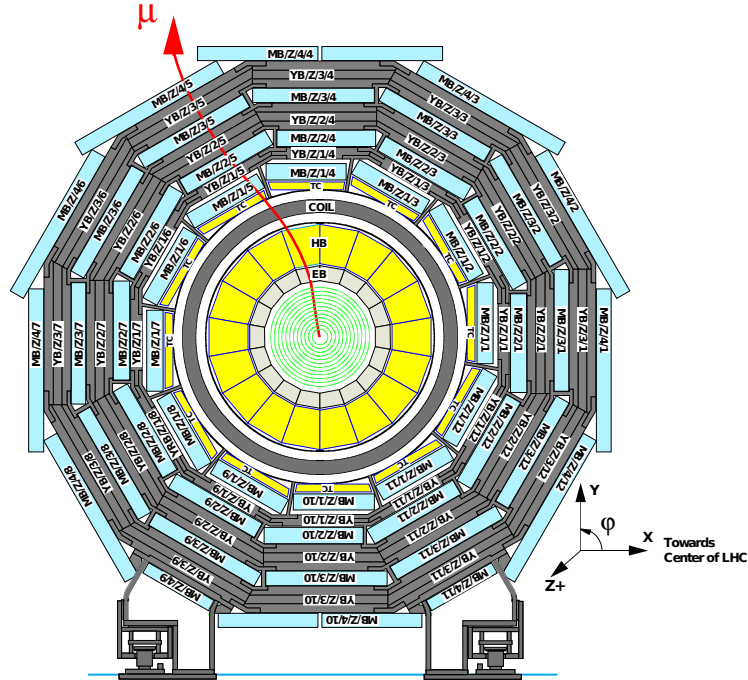


Figure 3.7: Cross-sectional view of CMS detector (originally from [11]). The drift-tube chambers are shaded in light blue, while the magnet solenoid and iron yoke is shown in gray.

A single drift-tube cell is 42 mm wide and 13 mm high and consists of an anode wire surrounded by cathode walls within a gas volume. A drift-tube chamber consists of 2 or 3 “superlayers”, which are sets of four layers of drift-tube cells. Superlayers are oriented with anode wires along the beamline (to measure the ϕ coordinate) as well as orthogonal to the beamline (for z -coordinate measurement). The left-right ambiguity in the drift direction within a drift-tube cell is resolved by staggering the cells by half-cell-widths and by obtaining track position measurements in at least three of the four cell layers of a superlayer. The DT provides a muon track measurement with a single-hit resolution of $250\ \mu\text{m}$ and an angular resolution of $\sim 1\ \text{mrad}$.

Cathode strip chambers are used in the endcap region, as shown in Fig. 3.8, and provide a coverage of $0.9 < |\eta| < 2.4$. They comprise of multiwire proportional chambers with the copper cathode segmented into strips aligned in the radial direction and with the anode wires aligned in the ϕ direction. An ionization avalanche results in a distribution of charge across several cathode strips, providing an improved track position measurement. Chambers are arranged in a trapezoidal shape with 7 cathode planes interleaved with planes of 3.1-mm-spaced anode wires. Chambers are grouped to form eight rings in each endcap. In total, there are of 234 CSC chambers per endcap.

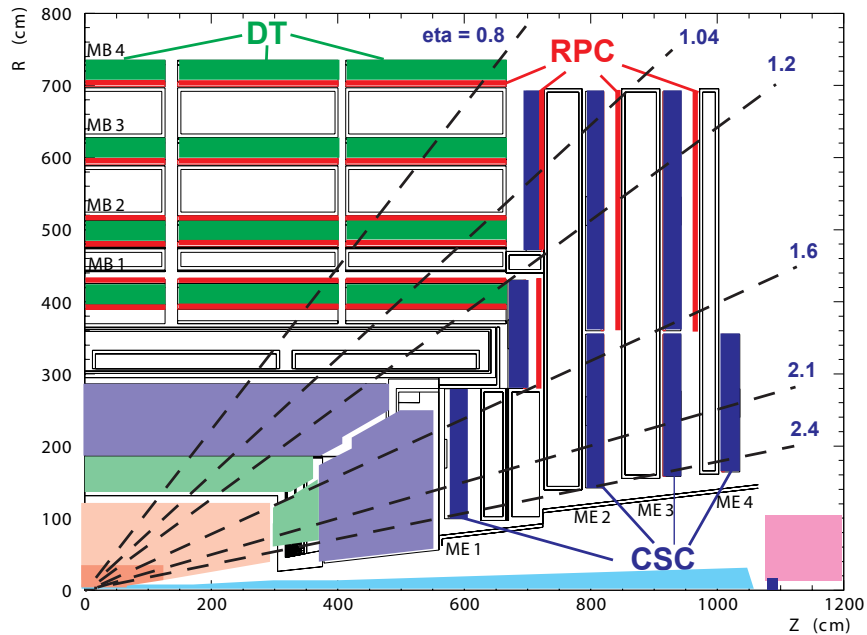


Figure 3.8: Quarter slice view of the CMS muon detectors [21]. Three of the five wheels of the DT system are shown in green. CSC chambers from each of the eight rings are shown in blue. The position of the RPC detectors are highlighted in red.

Resistive plate chambers provide a coverage of $|\eta| < 1.6$. Each chamber contains 2 or 3 sets of RPC layers, called “rolls”. Each roll is made of a pair of RPC units, where a unit consists of two parallel plates of high-resistivity plas-

tic placed within a strong electric field and separated by a 2-mm gas gap . The ionization avalanche caused by the passing muon induces a local change to the electric field between the plates. Due to short width of the gas gap, the passage of the muon can be detected with a time resolution of about 1 ns, making the RPC highly capable of assigning the muon to the correct bunch crossing. The high resistivity of the plates allows for a fast recovery of the electric field, which is crucial as the RPC is expected to function under a hit rate of 1 kHz/cm².

The placement of the RPC chambers is shown in Fig. 3.8. In the barrel region, an RPC chamber is attached to either side (a single side) of a DT chamber in the two innermost (outermost) barrels. In the endcap region, RPC chambers are attached to a single side of the CSC chambers in four of the rings. A total of 610 RPC chambers are used.

3.2.5 Trigger and DAQ system

At design luminosity, the LHC delivers collisions at a rate of 40 MHz. Most collisions will be generic pp scattering events, which are not of primary interest. Moreover, the practical limitations of disk storage permit only a small fraction of all collisions to be saved for later analysis. Therefore, a trigger and data acquisition (DAQ) system is required to reject all but the most interesting events. Furthermore, since a pair of bunches collide (at design luminosity) once every 25 ns, the system must be able to process multiple collisions concurrently.

CMS employs a two-level trigger system. A schematic of the trigger system is shown in Fig. 3.9. The Level 1 (L1) trigger consists of custom-made, programmable hardware designed to reduce the input event rate of 40 MHz to

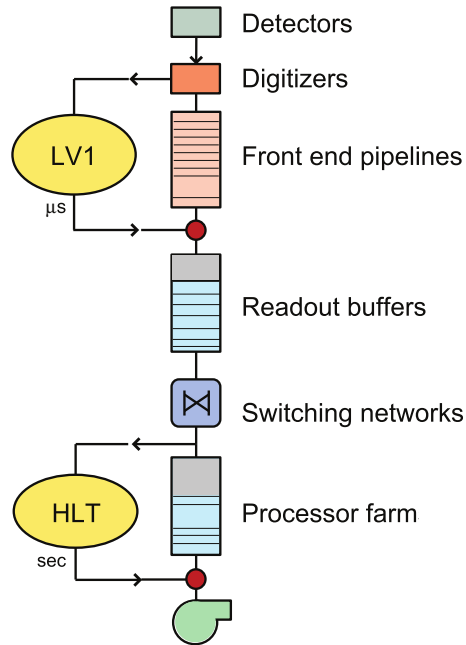


Figure 3.9: Schematic of CMS trigger and data acquisition system [22].

about 100 kHz. The data pipeline capacity of the L1 trigger is $3.2 \mu\text{s}$, which corresponds to simultaneously processing the collisions of 128 continuous bunch crossings (at design luminosity). To satisfy this time constraint without excessive infrastructure cost, the L1 trigger reads the information provided by the detectors at a coarser granularity than is available from the full detector readout. The ECAL and HCAL detectors are sub-divided into “trigger towers”, each consisting of a block of ECAL crystals and a corresponding set of HCAL towers. The energy patterns in the trigger towers are analysed to identify candidate electrons, photons, and jets. The total energy E_T of a trigger tower is also computed. The above four objects are called “trigger primitives” and are constructed for each tower within the region $|\eta| < 3$. In the forward region of $|\eta| > 3$, trigger primitives for only jets and energy sums are made. A Regional Calorimeter Trigger performs a set of algorithms on the trigger primitives from all trigger

towers to better identify e/γ candidates in regional segments covering half of the detector in z and 40° in ϕ . The candidates are forwarded to the Global Calorimeter Trigger, which sorts the e/γ candidates based on their transverse energies. In addition, jets are constructed and sorted, and the full detector energy sum computed (as well as the corresponding missing- E_T) at this stage. A final list of objects are then sent to the Global Trigger.

Trigger primitives are constructed from the DT system by track segments in the superlayers. They are sent to the DT Track Finder to match segments from different chambers and to assign kinematic parameters to the track. Similarly, track segments are formed in the CSC from the cathode and anode readout of each chamber using pattern templates. Three-dimensional tracks are constructed from these segments with the CSC Track Finder. In the RPC, hit patterns are formed using the spatial and temporal coincidence of hits in several RPC layers, and are assigned to the proper bunch crossing. The Global Muon Trigger receives up to four muon candidates from each of the DT, CSC, RPC-barrel, and RPC-endcap detectors. Lookup tables are used to combine candidates associated with a common muon and to assign a quality code to the candidates. The four highest-quality candidate muons are forwarded to the Global Trigger.

The Global Trigger performs the final decision to accept an event for processing at the second trigger level. It receives the muon and calorimeter candidates and executes a list of algorithms called “bits”, each of which is a logical combination of requirements on the number of candidates and their energies/momenta. The final L1 decision is based on the OR of all bits.

The task of the High Level Trigger (HLT) is to reduce the event rate of

100 kHz from the L1 trigger down to about 100 Hz for permanent storage. The HLT consists of a processor farm with about 1 000 nodes, 9 200 cores, and 18 TB of memory. The data from a collision event accepted by the L1 trigger is transferred to a readout buffer and then sent to a particular processor in the farm via a switching network that operates at ~ 100 GB/s.

At the HLT, the full granularity of the CMS detector is available and software algorithms similar to the offline object reconstruction (Sec. 4) can be performed. The basic strategy of the HLT software is to perform selection requirements that require a minimum amount of detector information before proceeding to more CPU-intensive reconstruction steps. For instance, selection criteria based only on information from the calorimeters and muon systems are applied first. Requirements on the pixel tracker hit information is then applied. Finally, the selection criteria requiring complete track reconstruction are evaluated. This strategy ensures that events are accepted/rejected in the least amount of time needed. The total processing time per event at the HLT is about 100 ms. As in the L1 trigger, a list of trigger paths are defined in the HLT, each path consisting of a set object selection criteria. An event is accepted for storage if it satisfies the requirements of at least one trigger path.

Events passing the HLT are sent to a storage manager, which routes the data from events to pre-defined disk streams used for online monitoring and for permanent storage. The average size of an event written to tape is 1.5 MB. A total of ~ 5 PB of data are collected each year at design performance.

CHAPTER 4

EVENT RECONSTRUCTION

In this chapter, we describe the techniques used to reconstruct the particles produced from a collision event. We begin with a discussion of the reconstruction of tracks and vertices. We then describe the reconstruction of muons and electrons, and give an overview of the particle-flow method. We then discuss the reconstruction of jets and the missing transverse energy, E_T^{miss} . Finally, we describe the various techniques for identifying b -quark jets.

4.1 Tracks and vertices

4.1.1 Tracks

Prior to reconstructing tracks, local clusters of hits in the pixel and strip trackers are formed. The clusters are then joined to form tracks using a Kalman filter method [23], which we describe below. The reconstruction proceeds in several iterations. The first iteration is responsible for reconstructing the most easily identified tracks, such as those with high transverse momenta and that are located near to the interaction point. Successive iterations attempt to reconstruct tracks that are harder to identify. This strategy, called “iterative tracking”, achieves both a high efficiency for genuine tracks and a relatively low reconstruction rate of fake tracks, where a fake track is one that is not produced by the passage of a particle. Each iteration consists of four steps - the generation of track “seeds”, the extrapolation of tracks from the seeds, track fitting, and track selection.

The first step of each iteration begins with the identification of track seeds. A track seed is formed from either a pair or a triplet of hits, with each hit originating from a separate detector layer. The hits, together with the beamspot position, provide an initial estimate of the trajectory parameters of the track. The pixel tracker is used to generate seeds due to its high granularity and close proximity to the interaction point. Moreover, lower momentum tracks will have smaller bending radii and will therefore require the reconstruction to begin in the innermost tracking layer.

The extrapolation of the track from the seed hits to the rest of the tracker system is performed using a Kalman filter method. The method takes an iterative approach to constructing the track. At each stage, a search is performed for compatible detector hits in the next outer detector layers using the present estimate of the track parameters. A χ^2 test is used to check the compatibility between a hit and the track. If a compatible hit is found, the trajectory parameters are updated with the new hit included. This process repeats until the outermost detector layer is reached. The effect of the tracker material on the trajectory is included in the extrapolation procedure.

Once the outermost hits are found, a more precise estimate of the track parameters is obtained by applying again the Kalman filter to the full list of associated hits. At this stage, the fit to the track takes into account the non-uniformity of the B -field, which prevents the track from following a perfect helix trajectory. In this case, the trajectory must be solved numerically. Finally, a complementary “smoothing” fit is performed using the same hits initialized from the opposite direction, beginning with the outermost tracks. This is done to refine the fit parameters and locate additional hits in the inner layers that were not found at the

seed-generation stage.

At each pass of the iterative tracking process, a set of selection criteria are applied to reject poorly reconstructed tracks. The selection criteria include requirements on the normalized chi-square χ_{norm}^2 of the track fit, the track impact parameter significance, and the number n_{layers} of pixel and strip tracker layers with hits. The first two requirements are of the form $\chi_{norm}^2 < \alpha_0 n_{layers}$ and $|d_0/\sigma_{d_0}| < (\alpha_1 n_{layers})^\beta$, where α_0 and α_1 range from 0.25 to 2 and where β is either 3 or 4, depending on the iteration stage. The condition on the number of layers, which varies from $n_{layers} > 0$ to $n_{layers} > 6$ depending on the iteration stage, is particularly effective in reducing the number of fake tracks.

The momentum resolution of tracks is about 0.7 (5.0)% at 1 (1 000) GeV in the central pseudorapidity region. Tracks from muons are reconstructed with an efficiency of at least 99% over a momentum range of $1 \text{ GeV} < p_T < 100 \text{ GeV}$ and across the full η range of the tracker. Tracks from charged pions, which undergo nuclear interactions with the tracker material, have a reconstruction efficiency in the range of 80% to 90% depending on the p_T and η of the pion.

4.1.2 Vertices

Once the tracks of a collision event have been reconstructed, the points of origin of the tracks, called the interaction vertices, can be extracted. The reconstruction of vertices proceeds in three steps. In the first step, a set of well-identified tracks are selected for clustering. The selection is based on the number of pixel and strip hits, the χ^2 of the track fit, and the track impact parameter with respect to the beamspot position. The second step is to decide which tracks belong to

a common vertex. The clustering of tracks is achieved with a deterministic annealing (DA) algorithm [24]. The z coordinates of the points of closest approach of the tracks to the beamspot are used as input to a function F that gives a measure of the probability of an a priori configuration of n number of vertices at positions z_1^V, \dots, z_n^V . The annealing method finds the vertex configuration that maximizes $F(z_k^V)$. In this manner, each track i is given a probability p_{ik} of originating from vertex k . The track is then assigned to the vertex for which p_{ik} is largest. The DA algorithm has the advantage over simpler clustering techniques of being robust against events with a large number of vertices. The positions of the vertices are then determined more precisely using an adaptive vertex fitter algorithm [25], which is an extension of the conventional Kalman filter method that is capable of handling track outliers wrongly associated with a vertex. The adaptive vertex fit returns a weight w between 0 and 1 for each track describing the likelihood of the track originating from the given vertex. We use the “number of degrees of freedom” of a vertex, $n_{dof} \sim \sum_{i=1}^{n_{Tracks}} w_i$, as a measure of the number of tracks compatible with the given vertex. The vertex with the largest value of $\sum_{tracks} p_{\Gamma}^2$, where the sum runs over all tracks associated with the vertex, is considered the hard-interaction vertex of the event.

4.2 Muons

Tracks in the muon systems are reconstructed using a Kalman filter method beginning with track segments in the innermost chambers. The track is propagated from one muon station to the next, taking into account the interaction of the muon with the material and the magnetic field. Once the track reaches the outermost station, a second Kalman filter is applied in the reverse direction,

beginning at the outermost station, to refine the track fit. Finally, the track is extrapolated into the nominal interaction point. Tracks that are constructed in this way are referred to as stand-alone muons, as their reconstruction relies solely on the hits in the muon systems. Standalone muons are reconstructed with a momentum resolution of better than 10% up to $p_T = 100$ GeV.

Stand-alone muon tracks can be extended to include hits in the tracker system. The track in the muon system is extrapolated inwards and compatible hits in the strip and pixel trackers are included iteratively. The final track is referred to as a global muon. The inclusion of hits in the inner tracker improves the muon momentum measurement for high p_T tracks, which have a relatively large bending radius. The relative momentum resolution of global muons is about 1% (5%) for muons with pseudorapidity $|\eta| \sim 0$ (2.1).

An alternate approach to combining tracks in the tracker system and the muon chambers is to extrapolate from all tracks reconstructed in the tracker outward to the muon system, again accounting for the changing B -field and detector material. If at least one track segment in the muon system is matched to the tracker track, the track is referred to as a tracker muon. Due to the less stringent requirements on the hits in the muon chambers, tracker muons have a higher efficiency of reconstruction for low- p_T muons ($p_T < 5$ GeV). Tracker muons and global muons that share the same tracker track are combined into a single muon candidate.

We refer to muons that are produced directly from the hard interaction as prompt muons. These include muons that are produced from the decay of a W or Z boson. All other sources of muon tracks are referred to as “fake” muons. These include tracks produced from pions or from decay-in-flight muons (e.g.

$K \rightarrow \mu$). To reduce the probability of misidentifying fake muons, we select tracks based on the normalized chi-square χ_{norm}^2 of the global muon fit, the number of hits in the silicon and pixel tracker, the transverse impact parameter d_0 of the track, and the longitudinal distance to the hard interaction vertex z_{pv} . The exact requirement for each quantity will be described in Sec. 5.3.

4.3 Electrons

Electrons are reconstructed using a combination of calorimeter and tracking information. Special care must be taken to account for the significant loss of energy, due to bremsstrahlung, of an electron as it traverses through the tracker and into the ECAL detector.

The reconstruction of electrons begins with the clustering of crystal deposits in the ECAL. As an electron traverses towards the ECAL, it will interact with the large tracker material and radiate bremsstrahlung photons. Since the solenoid field will bend the path of the electron in the ϕ direction, the energy deposited from the emitted photons will cover a large swath of ECAL crystals in the ϕ coordinate. The clustering algorithms are specially designed to handle such a pattern of energy deposits. In the barrel region, clusters are formed by starting from crystals that have locally maximum energy deposits, referred to as seed crystals. Crystal clusters of sizes 1×3 or 1×5 (in $\phi \times \eta$) are formed at each ϕ increment around the seed crystal. The crystal clusters are then themselves clustered in the ϕ direction to form a “supercluster”. In the endcap region, clusters are formed by collecting the energy in 5×5 crystal arrays. Clusters that lie within 0.3 rad in ϕ of each other are then grouped into superclusters. The position of a

supercluster is the energy-weighted average of its constituent crystals.

The electron track is constructed by first matching the supercluster formed in the calorimeter with compatible hits in the inner tracker layers. If such hits are found, a dedicated electron track reconstruction is performed. In contrast to the standard Kalman filter method for generic tracks, the track reconstruction for electrons applies a “Gaussian sum filter” technique [26], which accounts for the bremsstrahlung energy losses within the tracker and the possibility of track kinks due to the emission of photons. In this method, the energy loss is modeled using a linear combination of multiple Gaussian functions.

An alternative approach to electron reconstruction has been developed to accommodate low- p_T electrons, where the smear of bremsstrahlung can be too wide for the supercluster algorithms above, and for electrons near jets, where the presence of a large number of tracks can hinder the supercluster-track matching process. The approach starts from a set of high purity tracks, as reconstructed in the manner described in Sec. 4.1, and employs a particle-flow clustering method (Sec. 4.4) to form superclusters.

Electron candidates formed by the association of the reconstructed track and the supercluster undergo a pre-selection to reduce the probability of a hadronic jet to be misidentified as an electron. The selection requirements include a minimum angle in $\Delta\phi$ and $\Delta\eta$ between the supercluster and the track, a low fraction of energy deposited in the HCAL in the region around the supercluster, and a minimum supercluster energy of $E_T > 4 \text{ GeV}$. In the alternative approach to reconstructing electrons, a selection based on a multivariate discriminant is applied instead. To further reduce the contribution of fake electrons, candidates are selected based on the track impact parameter d_0 and the longitudinal dis-

tance to the hard interaction vertex z_{pv} , as in the case of muons. In addition, electrons must have a minimal amount of lost hits, where a lost hit is an instance in which the electron track crosses a detector layer without registering a hit.

4.4 Particle-flow reconstruction

The high granularity of the CMS detectors and the large magnetic field provide sufficient position and momentum resolution to allow for the individual reconstruction and identification of all stable particles produced in a collision event, namely muons, electrons, photons, charged hadrons, and neutral hadrons. The complete reconstruction of the event is achieved with the particle-flow algorithm [27], which is a method of combining the information from all detectors in a way that provides the most precise determination of the energy, direction, and species of each stable particle.

The fundamental building blocks of the reconstruction algorithm are the tracks in the tracker system, calorimeter clusters, and tracks in the muon system. Calorimeter clusters are formed in each subdetector (EB, EE, ES, HB, and HE) separately by aggregating calorimeter cells around the local energy maxima. Tracks are reconstructed in the iterative procedure described in Sec. 4.1.1. Tracks and clusters are then associated using a linking algorithm to avoid any possible double-counting between the deposited energy and measured track momentum. Similarly, clusters in the EB and EE are linked to clusters in the preshower and HCAL calorimeters.

In the particle-flow method, muons are reconstructed by forming links be-

tween the tracks in the tracker and the muon systems in the same manner as described in Sec. 4.2 for the case of global muons. Electrons are reconstructed by applying a Gaussian sum filter fit to high-purity tracks, as in Sec. 4.3. The electron candidates are then required to satisfy a selection criteria based on a multivariate discriminant using a combination of tracking and calorimeter information. Neutral hadrons and photons are reconstructed through the presence of large calorimeter deposits with few or no linked tracks. In the case of an overlap between calorimeter deposits and tracks, the photon and neutral hadron energy is taken as the excess of calorimeter energy with respect to the total momentum of the tracks. Any remaining track-calorimeter links in the event give rise to charged hadrons. The measured energy of a hadron is recalibrated to account for the non-linear response of the HCAL and for the difference in response of the ECAL between photons and hadrons.

4.5 Jets

Jets are reconstructed using the list of particle-flow candidates described in the previous section. The clustering of particles is performed using the anti- k_T algorithm [28], which defines the two distance measures:

$$d_{ij} = \min\left(\frac{1}{k_{T_i}^2}, \frac{1}{k_{T_j}^2}\right) \cdot \frac{\Delta_{ij}^2}{R^2}, \quad (4.1)$$

$$d_{iB} = \frac{1}{k_{T_i}^2}, \quad (4.2)$$

where k_{T_i} , y_i , and ϕ_i are the transverse momentum, rapidity, and azimuth angle, respectively, of particle i , and where $\Delta_{ij}^2 = (y_i - y_j)^2 + (\phi_i - \phi_j)^2$. The quantity d_{iB} gives a measure of the proximity of the particle to the beam-line. The algorithm proceeds at each iteration by finding the minimum value of d_{ij} and d_{iB} in the

event. If d_{ij} is the minimum, then particles i and j are combined into a single entity, while if the minimum is d_{iB} , particle i is considered a jet and removed from the event. The procedure terminates once all particles are removed. With this algorithm, jets are formed around the most energetic particles and are bounded geometrically by the parameter R . The anti- k_T algorithm is an infrared- and collinear-safe algorithm that has the desirable quality that jet boundaries are insensitive to the presence of soft particles. Moreover, the algorithm satisfies the practical requirement of running sufficiently quickly in the high luminosity environment of the LHC.

A typical jet that is reconstructed in the tracker-covered pseudorapidity region has on average 15%, 20%, and 65% of its energy carried by photons, neutral hadrons, and charged hadrons, respectively [29]. The measurement of the true energy of hadrons (and therefore of jets) is hindered by the non-uniformity and non-linear response of the calorimeters. The non-linearity with respect to the incident particle energy is a result of the different response of the HCAL to the hadronic and electromagnetic components of a hadron shower, as described in Sec. 3.2.3. Moreover, the presence of pile-up interactions will contribute additional unwanted energy to the reconstructed jets. To account for such effects, the measured four-momentum of a jet p_μ^{raw} is scaled by a correction factor that depends on the transverse momentum and pseudorapidity of the jet [30]:

$$p_\mu^{corrected} = C(p_T^{raw}, \eta) \cdot p_\mu^{raw}. \quad (4.3)$$

The correction factor C is composed of several pieces. The first piece accounts for the contribution from pile-up interactions. This contribution of energy is subtracted from each event using an estimate of the average energy deposition per unit area due to pile-up interactions¹ [31]. The second piece accounts for

¹ The estimate of the average energy deposition ρ from pile-up interactions is obtained by (a)

the relative non-uniformity of the detector in η . The relative response is measured using events with back-to-back jets. The third piece accounts for changes in the detector response as a function of the jet momentum. This component is measured using events with a γ +jet pair, with the well-measured photon providing an accurate measure of the true transverse momentum of the recoiling jet. The final piece accounts for residual differences found between the data and simulation. The total correction factor C can reach as large as 20% of the raw jet momentum, depending on the η and p_T of the jet. The energy resolution of jets is about 10% over a wide range in jet transverse momenta [32].

4.6 E_T^{miss}

The presence of neutral weakly-interacting particles, such as neutrinos, must be inferred from the imbalance of the total measured transverse momentum of the collision. The missing transverse energy is defined as $\vec{E}_T^{\text{miss}} = -\sum \vec{p}_T$, where the sum runs over all particles reconstructed from the particle-flow algorithm.

4.7 b jet identification

Jets arising from the hadronization and decay of b -quarks exhibit unique characteristics that allow their discrimination against jets from light-flavor (u , d , or s) quarks, gluons, and to a lesser extent c -quarks. The identification of b -quark jets (b jets) is crucial in reducing the otherwise overwhelming background processes

introducing a measure of the area A of a jet and (b) computing the average value of p_T/A over all jets in the event. Jets from pile-up interactions will have the property that $\rho \sim p_T/A$.

that contribute to the search for new physics processes with b -quark-enriched final states.

The discriminating properties of b -hadrons include their relatively large mass, high kinetic energies, long lifetime, the large number of charged particles produced in their decay, and their large branching ratios to leptons. With a typical proper lifetime of $c\tau \sim 400\mu\text{m}$, the tracks of the decay products of a b -hadron will tend to be produced with large impact parameters. Moreover, the long decay length results in an observable secondary vertex. In addition, due to the relatively large kinetic energy of the hadrons (from the b -quark fragmentation function), tracks will tend to be collimated relative to the jet axis.

The direct $b \rightarrow l$ and cascade $b \rightarrow c \rightarrow l$ decays each have a branching ratio of about 10%. This allows jets originating from b -quarks to be identified by the presence of nearby muons and electrons. For example, one can require a muon to lie within a cone of $\Delta R < 0.4$ about the jet axis, where $\Delta R = \sqrt{\Delta\phi^2 + \Delta\eta^2}$. Muons produced from b -hadron decays will tend to have lower momenta relative to muons from W or Z boson decays. Thus, the tracker muon algorithm (Sec. 4.2) can be used to provide a high identification efficiency for such muons. Using tracker muons with $p_T > 4\text{ GeV}$, the efficiency to identify b jets in this manner is about 15%. Additional discriminating properties of the muon include its transverse momentum relative to the jet axis and its track impact parameter. Both these quantities are expected to be larger for b -quark jets than for light-flavor and c -quark jets. While the efficiency for identifying b jets using their muonic decays is limited by the branching ratio given above, the method is relatively straightforward and takes advantage of the excellent muon reconstruction capability of the detector system. This technique has been used, for

example, in an early measurement of the top-pair production cross section at the LHC [33].

The impact parameter d_{IP} of tracks associated with a jet can also be used as a simple and efficient means to identify b jets. Since the uncertainty σ_{IP} on the measured impact parameter is dependent on the track position and momentum, the impact parameter significance d_{IP}/σ_{IP} is used as the discriminating variable [34].

Another distinguishing feature of b jets is the presence of a secondary vertex in the jet. As in the case of primary vertex reconstruction (Sec. 4.1.2), secondary vertices are reconstructed with the adaptive vertex fitter. To maintain a high purity in reconstructing true secondary vertices, tracks entering the vertex fit must satisfy more stringent requirements than in the primary vertex reconstruction. In addition, tracks are required to lie within $\Delta R < 0.3$ of the jet axis. To reject reconstructed secondary vertices that are compatible with a primary vertex, secondary vertices are required to have less than 65% of their associated tracks in common with the primary vertex. In addition, the significance in the separation in r between the secondary vertex and a primary vertex must satisfy $\Delta d_r/\sigma_{\Delta d_r} > 3$. Moreover, to reduce the contamination from vertices caused by the interaction of hadrons with the detector material and by long-lived light-flavor mesons, secondary vertices are required to be within $\Delta d_r < 2.5$ cm of the primary vertex and to have a vertex mass incompatible with a K^0 and less than 6.5 GeV. Finally, the flight direction, defined by the vector pointing from the hard interaction vertex to the secondary vertex, must be within $\Delta R < 0.5$ of the jet axis.

The information from the impact parameters of tracks associated with a jet

and from the reconstructed secondary vertex can be combined to increase the efficiency of identifying b jets. This is achieved using a multivariate technique, which we refer to as the Combined Secondary Vertex (CSV) algorithm. In the instances where a secondary vertex is not reconstructed, tracks with $d_{IP}/\sigma_{IP} > 2$ can still be combined to form a “pseudo-vertex”. This allows the computation of vertex-like quantities for such jets. If neither a vertex nor pseudo-vertex can be constructed, the discrimination is made using only the track information.

The CSV algorithm is constructed as follows. A set of nine variables are used to construct a joint likelihood. They are the secondary vertex category (i.e. vertex, pseudo-vertex, or no-vertex), the transverse flight distance significance, the vertex mass, the number of tracks at the vertex, the fraction of the jet energy carried by tracks from the vertex, the pseudorapidity of vertex tracks with respect to the jet axis, the transverse impact parameter significance of the first track that raises the vertex mass above the c -quark threshold of 1.5 GeV (with tracks ordered in decreasing transverse impact parameter significance), the number of tracks in the jet, and the three-dimensional impact parameter significance of the tracks. Because the distribution of these variables for c -quark jets are sufficiently distinct from that of light-flavor/gluon jets, we treat these two categories of jets separately. For each jet flavor (b , c , or light/gluon), we construct a likelihood function $\mathcal{L}^{b,c,l} = f^{b,c,l}(\alpha) \cdot \prod_i f_{\alpha}^{b,c,l}(x_i)$, where α refers to the vertex category, x_i are each of the 8 remaining variables listed above, and $f^{b,c,l}$ are the probability density functions for each variable. We then construct a b jet discriminant using a weighted sum of likelihood ratios:

$$d_{CSV} = 0.25 \cdot \frac{\mathcal{L}^b}{\mathcal{L}^b + \mathcal{L}^c} + 0.75 \cdot \frac{\mathcal{L}^b}{\mathcal{L}^b + \mathcal{L}^l}, \quad (4.4)$$

where the values of 0.25 and 0.75 are used as a rough estimate of the relative fractions of c -quark and light-flavour/gluon jets in the set of all non- b jets. By

construction, d_{CSV} has an output between 0 and 1, with higher values of d_{CSV} representing a higher probability of the jet being a b jet.

The efficiency to identify true b jets (b -tag efficiency) and the efficiency to falsely identify non- b jets as b jets (mis-tag rate) with the CSV algorithm depend on the choice of the threshold on d_{CSV} . A lower threshold cut on d_{CSV} results in a higher b -tag efficiency, but with an accompanying increase in the mis-tag rate. Various techniques have been developed to measure the b -tag efficiency and mis-tag rate in situ from the collected data [34]. For the particular threshold cut of $d_{CSV} > 0.679$, the b -tag efficiency and mis-tag rate are about 75% and 1%, respectively, for 80 GeV jets.

CHAPTER 5

SEARCH FOR SUPERSYMMETRY IN EVENTS WITH B-QUARK JETS AND E_T^{MISS}

This chapter describes the search for top and bottom squarks from gluino-pair and top-squark-pair production. We search in events with large E_T^{miss} , no isolated leptons, at least three high- p_T jets, and one or more bottom-quark jets (b jets). We begin this chapter with an introduction to the search. We then describe the data and simulated samples used in the analysis, the event selection, and the measurement of the trigger efficiency. We then discuss the data-driven techniques used to determine each of the background contributions. After demonstrating the effectiveness of each technique separately, we combine the background predictions in a global likelihood function. Finally, we present the interpretation of the results in terms of the simplified model spectra introduced in Section 2.2.4.

5.1 Introduction

The b -quark-enriched SUSY models discussed in Section 2.2.4 can exhibit striking experimental signatures. A typical event in the $\tilde{g}\tilde{g} \rightarrow bbbb$ model will have four high- p_T b jets and large E_T^{miss} arising from the two LSP's. In the $\tilde{g}\tilde{g} \rightarrow tttt$ model, an additional eight jets can arise from the hadronic decay of each of the four W bosons. Thus, a distinctive feature of these models is the production of multiple high- p_T b (and non- b) jets, large E_T^{miss} , and no leptons.

The requirement of one or more b jets significantly reduces the contribution from SM processes. The primary sources of background in such a final state

include the production of $t\bar{t}$ and single-top-quark events, the production of a W or Z boson in association with multiple jets, and non-top-quark multijet events produced entirely via the strong interactions. Throughout the text, we will refer to the last category of events as “QCD” background. For events with a top quark or W boson, large E_T^{miss} can be produced through the decay of a W into a charged lepton and neutrino. Similarly, for events with a Z boson, the decay of the Z into two neutrinos also results in a significant amount of E_T^{miss} . In QCD events, large E_T^{miss} arises predominantly through the mismeasurement of the momentum of a jet. Semileptonic b - and c -quark decays give a smaller contribution to the E_T^{miss} in QCD events.

The strategy of the search is as follows. We first apply a series of selection criteria to significantly reduce the contribution from SM background. In addition, we define a set of search regions that are each sensitive to unique regions in the parameter space of the simplified model spectra. We then use Monte Carlo simulation to study the characteristics of the remaining SM background processes and to validate the data-driven background estimation methods. The data-driven methods rely on control samples from the data that are enriched in a particular background process. The estimates are then combined in a global likelihood function that accounts for correlation among the background methods and for potential contributions from the SUSY signal in the control samples.

5.2 Data and Monte Carlo samples

A total of 5.55 fb^{-1} of data were collected from March to October of 2011. We reject a small fraction of the recorded data due to poor detector conditions and use a total of 4.98 fb^{-1} of data in this search. Figure 5.1 illustrates the accumulation of the data throughout the year.

We use Monte Carlo (MC) generators to simulate the production of a SUSY signal and SM background processes from proton-proton collisions. The collision of high-energy hadrons can be factorized into several components. The primary component is the hard interaction of a parton of one hadron with a parton of the other. The momentum of each parton is described by a parton distribution function. A second component is the emission of particles from the two partons and from the hard-scatter products prior to and after the hard scatter, respectively. This is referred to as initial-state and final-state radiation. A third component is the decay of short-lived particles produced from the hard scatter. A fourth component is the showering of all the remaining colored particles after the hard scatter and the subsequent formation of hadrons. Finally, there is the component of the collision that describes the remnant constituents of the two hadrons not participating in the hard interaction, referred to as the underlying event. A proper simulation of a proton-proton collision must account for all of the above components.

The generation of a physics process as described above is then interfaced with a detailed simulation of the CMS detector. This allows us to study the characteristics of the event reconstruction of a given process of interest. In particular, we use MC simulation to study the details of event kinematics and to

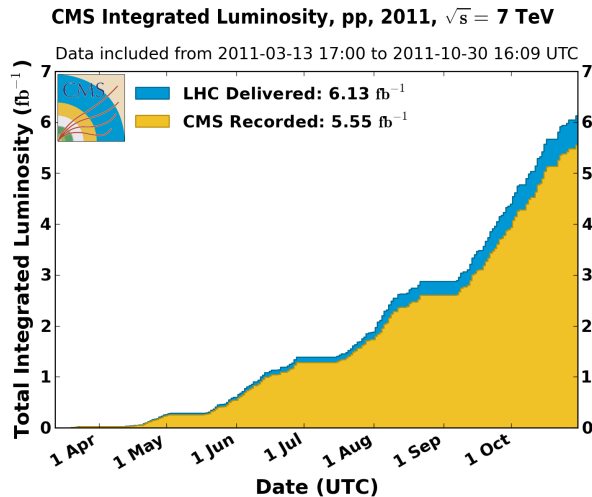


Figure 5.1: The integrated luminosity collected in 2011 [35]. Of the 5.55 fb^{-1} recorded by the experiment, 4.98 fb^{-1} were recorded with all detectors in a good condition.

measure the detector acceptance. In addition, the simulation provides a means of developing and validating the background estimation methods. To compare sets of MC events of different physics processes (MC samples) with each other and with the data, we assign a weight to the set of events corresponding to process X given by $w_X = \sigma_X \cdot L_{int} / N_X$, where σ_X is the cross section of the physics process, L_{int} the integrated luminosity corresponding to the collected data, and N_X the total number of events generated.

Background samples are generated at the parton-level with either MADGRAPH 5.1.1.0., POWHEG 301, or PYTHIA 6.4.22. For all samples, PYTHIA 6.4 is used to describe the parton-showering and hadronization, with the CTEQ6 [36] set describing the parton distribution functions. The decay of τ leptons in the MC is modeled using the TAUOLA package [37]. The response of the CMS detector is fully simulated with GEANT4 [38] and includes a complete emulation of the L1 trigger system. A list of the background samples, as well as the cross

sections used, is given in Table 5.1. The $t\bar{t}$ MC is weighted using the measured $t\bar{t}$ cross section. QCD samples are produced in bins of \hat{p}_T and span over a large range of cross sections. The bins with the largest contribution to the analysis signal regions correspond to the ranges $300 \text{ GeV} < \hat{p}_T < 470 \text{ GeV}$ and $470 \text{ GeV} < \hat{p}_T < 600 \text{ GeV}$, which have cross sections of 1170 pb and 70.2 pb, respectively. For the $W \rightarrow l\nu$, $Z \rightarrow \nu\nu$, and $Z \rightarrow l^+l^-$ processes, a minimum threshold requirement of $H_T^{gen} > 300 \text{ GeV}$ is imposed during event generation, where H_T^{gen} is the transverse energy sum of all generator-level jets. This is done so that the majority of the events in each sample are not rejected by the high H_T requirements of the search regions.

Signal samples are generated using PYTHIA 6.4. For the $\tilde{g}\tilde{g} \rightarrow bbbb$ and $\tilde{g}\tilde{g} \rightarrow tttt$ models, events are generated across a grid of points in $m_{\tilde{g}}$ vs. m_{LSP} space. Similarly, for the $\tilde{t}\tilde{t} \rightarrow tt$ model, a scan over $m_{\tilde{t}}$ vs. m_{LSP} space is generated. The mass ranges are listed in Table 5.2. Due to the large number of events that must be generated over the entire parameter space, the full GEANT4 simulation of the CMS detector would require a very large amount of computing resources. Instead, signal samples are generated using “Fast Simulation” [43], which employs a simplified model of the CMS detector geometry and response, and a customized track reconstruction algorithm. The Fast Simulation has been tuned to agree with the full simulation for a wide variety of particle interactions and across a large range of energies, while having the advantage of reducing event generation times by two to three orders of magnitude. Residual differences between the event reconstruction with Fast Simulation and the full simulation, such as those observed in the efficiency of b jet identification, are accounted for in the treatment of the signal efficiency uncertainty. The cross sections for gluino-pair and top-squark-pair production are calculated at next-

Table 5.1: MC sample information for background processes. The last column shows the equivalent integrated luminosity of the sample, which is a measure of the total number of events generated. For example, for the $t\bar{t}$ sample, $\sigma \cdot L_{\text{equiv}} \sim 60 \times 10^6$ events were generated. For the $W \rightarrow lv$ and $Z \rightarrow l^+l^-$ processes, $l = e, \mu$, and τ combined.

Process	Generator	σ (pb)	Order	L_{equiv} (fb^{-1})
$t\bar{t}$	MADGRAPH	158 [39]	-	376
t/\bar{t} (s -channel)	POWHEG	3.2/1.4 [40]	NNLO	82/96
t/\bar{t} (t -channel)	POWHEG	42/23 [41]	NNLO	93/86
t/\bar{t} (tW -channel)	POWHEG	7.9 [42]	NNLO	103
$W \rightarrow lv$	MADGRAPH	48.5	LO	111
$Z \rightarrow \nu\bar{\nu}$	MADGRAPH	42.1	NLO	72.8
$Z \rightarrow l^+l^-$	MADGRAPH	20.9	LO	326
WW	PYTHIA	27.8	LO	152
WZ	PYTHIA	10.5	LO	407
ZZ	PYTHIA	4.3	LO	977
QCD	PYTHIA	-	LO	-

to-leading order precision using the PROSPINO2 program, assuming a reference MSSM scenario [7].

For all MC samples, pile-up interactions (Sec. 3.1) are simulated and the MC is reweighted so that the average number of pile-up interactions matches that of the data.

Table 5.2: MC sample information for signal processes. For a given gluino (or top-squark) mass, the LSP is constrained kinematically to satisfy $m_{\text{LSP}} < m_{\tilde{g}}$ (or $m_{\text{LSP}} < m_{\tilde{t}}$).

Process	$m_{\tilde{g}}/m_{\tilde{t}}$ range [GeV]	m_{LSP} range [GeV]	# Events per point
$\tilde{g}\tilde{g} \rightarrow bbbb$	$100 < m_{\tilde{g}} < 1200$	$50 < m_{\text{LSP}} < 1150$	10,000
$\tilde{g}\tilde{g} \rightarrow tttt$	$450 < m_{\tilde{g}} < 1200$	$50 < m_{\text{LSP}} < 800$	50,000
$\tilde{t}\tilde{t} \rightarrow tt$	$225 < m_{\tilde{t}} < 1200$	$50 < m_{\text{LSP}} < 1025$	50,000

5.3 Event selection

Events are selected by requiring a large amount of calorimetric activity and missing transverse energy at the trigger level. We reconstruct jets at the L1 and HLT entirely with calorimeter deposits. The decision at the L1 requires that the scalar transverse energy sum of all jets be larger than 100 GeV. At the HLT, events are required to satisfy both an H_T and an H_T^{miss} requirement, where H_T is the scalar sum of all jets with $p_T > 40$ GeV and $|\eta| < 3.0$, while H_T^{miss} is the modulus of the vector sum of jets with $p_T > 30$ GeV and $|\eta| < 3.0$. A complete list of the triggers used at the HLT for the signal selection is given in Table A.2 The most stringent requirements at the HLT were $H_T > 350$ GeV and $H_T^{\text{miss}} > 110$ GeV.

Events are reconstructed offline using the particle-flow method described in Sec. 4. Jets are formed by clustering the set of all reconstructed particles. However, to obtain the most accurate measurement of the momentum of the parton that formed a given jet, certain types of particles are excluded from the clustering process. For example, an isolated lepton produced near the hard interaction vertex tends to originate from a W or Z boson, and not from the decay of a hadronic jet. Moreover, particles produced from pile-up interactions in the event can have the unwanted effect of overlaying additional tracks or energy deposits near a jet produced from the hard interaction¹. Therefore, prior to clustering the list of reconstructed particles into jets, certain particles are removed from the list based on the following conditions. First, reconstructed charged hadrons associated to vertices that are not the hard interaction vertex (i.e. pile-up vertices) are removed. Second, isolated electrons and muons with $p_T > 5$ GeV that are compatible with originating from the hard interaction vertex are also re-

¹This is true even after applying the pile-up-related jet momentum correction described in Sec. 4.5, which does not sufficiently subtract the energy from charged hadrons.

moved. Jets are clustered with the remaining list of particles using the anti- k_T algorithm with distance parameter $R = 0.5$ (Sec. 4.5).

To ensure a high-quality vertex fit consistent with a hard interaction (Sec. 4.1), the vertex with the highest sum- p_T^2 of associated tracks is required to satisfy the conditions given in Table 5.3. The identification requirements on jets, electrons, and muons are also listed in Table 5.3. The relative isolation of a lepton with transverse momentum p_T^l is given by

$$I = \left(\sum_{\text{charged hadrons}} p_T + \sum_{\text{neutral hadrons}} E_T + \sum_{\text{photons}} E_T \right) / p_T^l, \quad (5.1)$$

where the sums indicate the total transverse momentum/energy of charged hadrons/neutral hadrons/photons in a cone of radius $\Delta R = \sqrt{\Delta\phi^2 + \Delta\eta^2} = 0.3$ around the lepton. The other lepton quality requirements in Table 5.3 are described in Secs. 4.2 and 4.3. The list of jet quality requirements is applied to reduce contributions from anomalous sources of jets, including jets that arise from HCAL noise. Events are required to have at least three jets and no muons or electrons.

We define the offline $H_T = \sum_{i=1}^{n\text{Jets}} p_{T,i}$, with the jets satisfying the above requirements. The missing transverse energy vector \vec{E}_T^{miss} is defined as the negative vectorial sum of all reconstructed particle-flow objects, as described in Sec. 4.6. The thresholds on H_T and $E_T^{\text{miss}} = |\vec{E}_T^{\text{miss}}|$ are discussed in the following section.

To reduce the contribution of QCD-background events, in which the \vec{E}_T^{miss} tends to align with the mismeasured jet (or the semileptonically decaying b jet), we require that the \vec{E}_T^{miss} direction be at a minimum angle in ϕ away from the jets in the event. The exact requirement is defined and discussed in Sec. 5.5.1.

We identify b jets in the event using the Combined Secondary Vertex algo-

Table 5.3: Selection criteria for analysis objects. For the case of electrons, η_{sc} refers to the measurement of the pseudorapidity of the corresponding supercluster.

Object	Selection
Vertex	$n_{dof} > 4, z < 24 \text{ cm}, \rho < 2 \text{ cm}$
Electron	$p_T \geq 10 \text{ GeV}, \eta_{sc} < 2.5, 1.4442 < \eta_{sc} < 1.566$ At most one lost hit $ d_0 < 0.02 \text{ cm}, z_{pv} < 0.5 \text{ cm}$ $I < 0.2$
Muon	$p_T \geq 10 \text{ GeV}, \eta < 2.4$ Global muon and Tracker muon $\chi_{norm}^2(\text{global muon}) < 10, \geq 1$ valid hits in muon system ≥ 11 (≥ 1) silicon (pixel) hits on track $ d_0 < 0.02 \text{ cm}, z_{pv} < 0.5 \text{ cm}$ $I < 0.15$
Jet	$p_T \geq 50 \text{ GeV}, \eta < 2.4$ At least two constituents and one charged constituent $< 99\%$ of energy from neutral hadrons, photons, or electrons $> 0\%$ of energy from charged hadrons

rithm described in Sec. 4.7. Jets are considered b jets if they have a discriminant value of $d_{CSV} \geq 0.679$. The threshold is chosen such that the probability of misidentifying a light-flavored or gluon jet as a b jet is around 1% for jets with p_T around 80 GeV. The corresponding efficiency to identify true b jets is around 75%. To increase the sensitivity of the analysis to signal models with lower momentum b jets, we loosen the p_T requirement for b jets to 30 GeV.

Finally, we apply a set of filters that are designed to reduce the contribution from events with anomalous sources of E_T^{miss} . Such sources include the presence of inactive detector regions and poor track reconstruction. A description of the filters is given in Sec. A.4.

5.3.1 Selection regions and nomenclature

We define five search regions based on the criteria on E_T^{miss} , H_T , and the number of b jets. The regions are listed in Table 5.4 and are labeled in the format “NBL”(“NBT”), where NB refers to the requirement on the number of b jets, and L (T) refers to the “loose” (“tight”) set of E_T^{miss} and H_T requirements. Since we consider only one search region with ≥ 3 b jets, we drop the L label for that selection.

The search regions are chosen to maximize the sensitivity to different regions of $m_{\tilde{g}}$ vs. m_{LSP} (or $m_{\tilde{t}}$ vs. m_{LSP}) space in the simplified models. When optimizing the search region definitions, we take into account constraints imposed by the trigger and by the background estimates. The 3B (2BT) selection is expected to give the best sensitivity in the $\tilde{g}\tilde{g} \rightarrow bbbb$ and $\tilde{g}\tilde{g} \rightarrow tttt$ models with low (high) values of $\Delta m = m_{\tilde{g}} - m_{\text{LSP}}$, while the 1BT selection is expected to be best-suited for the $\tilde{t}\tilde{t} \rightarrow tt$ model.

For each search region, a set of corresponding control regions are used in the background prediction methods. The regions are defined in Table 5.5, where we also introduce the nomenclature that will be used throughout the text. The purpose of each control region is discussed in the relevant background prediction section.

Table 5.4: Search regions definitions. Common selection requirements for all search regions include the criteria described in Sec. 5.3.

Search Region Name	E_T^{miss} [GeV]	H_T [GeV]	$N_{b\text{jets}}$
1BL	≥ 250	≥ 400	≥ 1
1BT	≥ 500	≥ 500	≥ 1
2BL	≥ 250	≥ 400	≥ 2
2BT	≥ 300	≥ 600	≥ 2
3B	≥ 250	≥ 400	≥ 3

5.3.2 Suppressing SM background with b jets

The requirement of one or more b jets significantly reduces the amount of expected SM background relative to the expected signal in the SUSY models of interest. In particular, $t\bar{t}$ events are expected to have only two b jets, while the production rate of a W or Z boson in association with heavy-flavor jets is expected to be relatively small. This is illustrated in Table 5.6, where we show the expected yield of signal and SM background events computed from MC simulation. Using the values of $m_{\tilde{g}} = 925$ GeV and $m_{\text{LSP}} = 100$ GeV in the $\tilde{g}\tilde{g} \rightarrow bbbb$ model as a benchmark, we find that the signal-to-background ratio increases by factors of three and fifty for the 1BL and 3B selections, respectively, relative to a selection without requiring b jets.

Table 5.5: Relationship between the search region (SIG) and the corresponding control regions. Common selection requirements for all regions include the criteria described in Sec. 5.3. The variable $\Delta\hat{\phi}_{\min}$ is defined in Sec. 5.5. For the regions that require one or two leptons, a lepton means an e or μ . For the SIG-DL and SB-DL control regions, the threshold on the b -tag discriminant is lowered to $d_{CSV} \geq 0.244$ (see Sec. 5.6).

Region	Description
SIG	Search region defined in Table 5.4.
SB	Identical to SIG, except with $150 \text{ GeV} < E_{\text{T}}^{\text{miss}} < 250 \text{ GeV}$.
SIG-LDP	Identical to SIG, except with $\Delta\hat{\phi}_{\min} < 4$.
SB-LDP	Identical to SB, except with $\Delta\hat{\phi}_{\min} < 4$.
SIG-SL	Identical to SIG, except for the requirement of exactly 1 lepton.
SB-SL	Identical to SB, except for the requirement of exactly 1 lepton.
SIG-DL	Identical to SIG, except for a $Z \rightarrow l^+l^-$ and ≥ 1 b jet selection.
SB-DL	Identical to SIG-DL, except for $150 \text{ GeV} < E_{\text{T}}^{\text{miss}} < 250 \text{ GeV}$.

Table 5.6: Expected selection yield in 4.98 fb^{-1} from MC simulation. For $\tilde{g}\tilde{g} \rightarrow bbbb$, we use the benchmark point of $m_{\tilde{g}} = 925 \text{ GeV}$ and $m_{\text{LSP}} = 100 \text{ GeV}$. The Pre- b selection corresponds to the selection requirements of the 1BL region, except with no requirement on the number of b jets. The last column gives the signal-to-background ratio. The uncertainties are statistical only.

Selection	QCD	$Z \rightarrow \nu\bar{\nu}$	top & W	Total SM	$\tilde{g}\tilde{g} \rightarrow bbbb$	S/B
Pre- b	107 ± 27	683 ± 8	930 ± 6	1720 ± 29	56.4 ± 1.0	0.03
1BL	28 ± 6	104 ± 2	362 ± 2	494 ± 7	54.1 ± 0.9	0.11
1BT	0.7 ± 0.2	5.3 ± 0.4	7.2 ± 0.4	13.2 ± 0.6	13.7 ± 0.4	1.04
2BL	6 ± 1	13.8 ± 0.7	128 ± 1	148 ± 2	42.7 ± 0.8	0.29
2BT	1.7 ± 0.6	3.5 ± 0.3	31.6 ± 0.5	36.7 ± 0.9	34.3 ± 0.7	0.93
3B	0.29 ± 0.07	0.8 ± 0.1	13.9 ± 0.2	15.0 ± 0.2	22.1 ± 0.4	1.47

5.4 Trigger efficiency

Since the MC simulation includes an emulation of the L1 trigger system and uses the same HLT software algorithms that are applied to the data, the trigger selection described in the previous section can in principle be applied to the events in the MC. However, the trigger thresholds at the HLT evolved rapidly during the data-taking period, due to increasing instantaneous luminosities. The MC samples are generated with a single version of the trigger condition and, due to the large computational resources required to generate the MC, cannot be regenerated every time an updated trigger is deployed in the data. Therefore, when using the MC, we simply weight the MC events by the measured efficiency of the trigger, as described below.

The probability for an event with a given a offline H_T and E_T^{miss} value to pass the trigger condition is called the trigger efficiency. We evaluate from data the efficiency for events to pass the H_T and H_T^{miss} components of the trigger separately. For the H_T component, we measure the efficiency using an independent muon-triggered dataset. The H_T efficiency for the most stringent condition $H_T > 350\text{ GeV}$ is shown in the left plot of Fig 5.2. The overall efficiency of the H_T component is measured to be 86% (99%) for offline H_T values of 400 GeV (500 GeV).

We find the H_T^{miss} efficiency to differ between events containing an electron or muon and events with no leptons. This is due primarily to the fact that events with no leptons are largely QCD events, where most of the E_T^{miss} arises from jet mismeasurements, while events with a single lepton are largely top-quark and W events, where the E_T^{miss} arises from a neutrino. For events without lep-

tons, the H_T^{miss} efficiency is measured using a sample collected with only an H_T requirement at the trigger level. For events with a single lepton, we use a sample collected from a lepton+ H_T trigger, with the H_T requirement in the trigger identical to that of the main analysis trigger. The H_T^{miss} efficiency curve for the tightest condition $H_T^{\text{miss}} > 110 \text{ GeV}$ is shown for the case without leptons in the right plot of Fig 5.2.

Since a wide range of H_T^{miss} thresholds were applied at the HLT throughout the year, we compute the overall H_T^{miss} efficiency as the weighted average of efficiencies at each threshold. The weights correspond to the fraction of the total integrated luminosity collected by each trigger. The overall H_T^{miss} efficiencies for various offline selections used in the analysis are given in Table 5.7. The efficiency of the H_T^{miss} component of the trigger is 98% for $E_T^{\text{miss}} > 250 \text{ GeV}$ in the signal region.

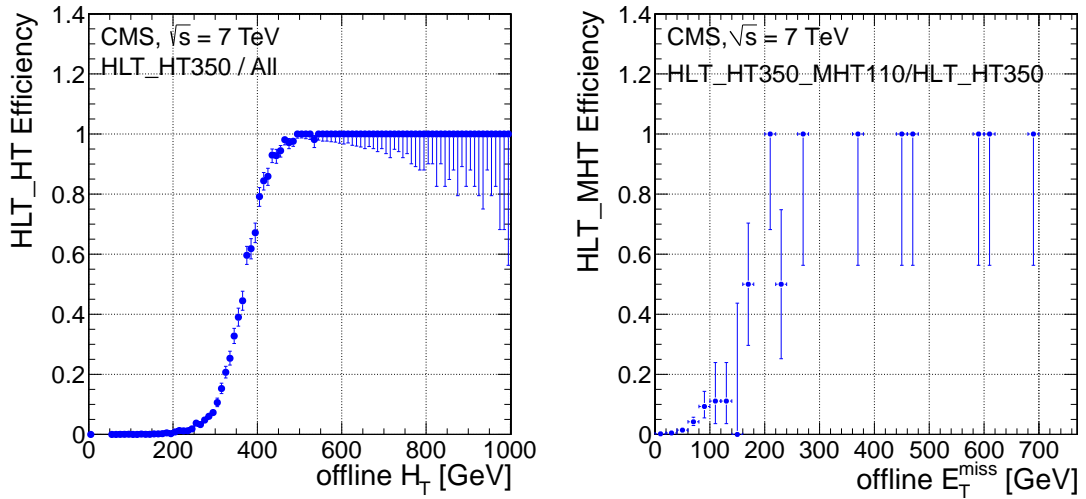


Figure 5.2: Efficiency for the $H_T > 350 \text{ GeV}$ condition (left) and the $H_T^{\text{miss}} > 110 \text{ GeV}$ condition (right) of the tightest trigger. For the H_T^{miss} efficiency, the 0-lepton offline cuts described in Table 5.7 have been applied.

Table 5.7: Overall H_T^{miss} efficiencies for various offline selections used in the analysis. The 0-lepton ($1-e/\mu$) selection refers to the requirement of zero leptons (one electron/muon) in the evaluation of the efficiency. For all selections, the cuts $H_T \geq 400$ GeV and $\Delta\hat{\phi}_{\text{min}} > 4$ have been applied. Errors shown are statistical only.

Selection	E_T^{miss} region [GeV]	H_T^{miss} efficiency (%)
0-lepton	$150 < E_T^{\text{miss}} < 250$	$85.0^{+3.4}_{-4.6}$
	$E_T^{\text{miss}} \geq 250$	$98.1^{+1.2}_{-3.6}$
1- e	$150 < E_T^{\text{miss}} < 250$	$95.4^{+0.7}_{-0.9}$
	$E_T^{\text{miss}} \geq 250$	$100^{+0}_{-1.7}$
1- μ	$150 < E_T^{\text{miss}} < 250$	$99.1^{+0.3}_{-0.5}$
	$E_T^{\text{miss}} \geq 250$	$100^{+0}_{-1.9}$

5.5 QCD background

QCD-background events enter the signal region primarily in the scenario where a single jet is grossly mismeasured. This may be due either to a detector mismeasurement or from the semileptonic decay of a b or c jet, where in the latter case a neutrino is emitted from the decay of the heavy-flavor hadron. The contribution from events of the latter type is enhanced naturally by our b jet requirement. For example, in the 1BL selection, roughly two thirds of QCD events have at least one true b jet, and in roughly one third of QCD events, more than half of the total E_T^{miss} arises from the semileptonic decay of a b jet.

The overall contribution from QCD events to the total SM background is heavily suppressed by the b jet requirement. While QCD events are expected to contribute only as much as 5% of the total background, they are difficult to model accurately in the simulation, particularly in the high E_T^{miss} and high H_T regions that this search is sensitive towards. We therefore control and estimate the QCD background using a data-driven technique that allows us to (a) eliminate the vast majority of QCD events and (b) provide a straightforward and effective means to estimate the remaining QCD background.

5.5.1 Construction of $\Delta\hat{\phi}_{\text{min}}$ variable

Fig. 5.3 provides an illustration of the E_T^{miss} arising from a typical QCD event. As discussed above, the E_T^{miss} is due primarily to a single jet i that is significantly mismeasured. If all other jets in the event were perfectly measured, then the E_T^{miss} would point exactly along the direction of jet i . More realistically, each of

the other jets in the event are typically also mismeasured by an amount dictated by their energy resolutions. This results in a non-zero angle $\Delta\phi_i$ between the resulting E_T^{miss} and jet i .

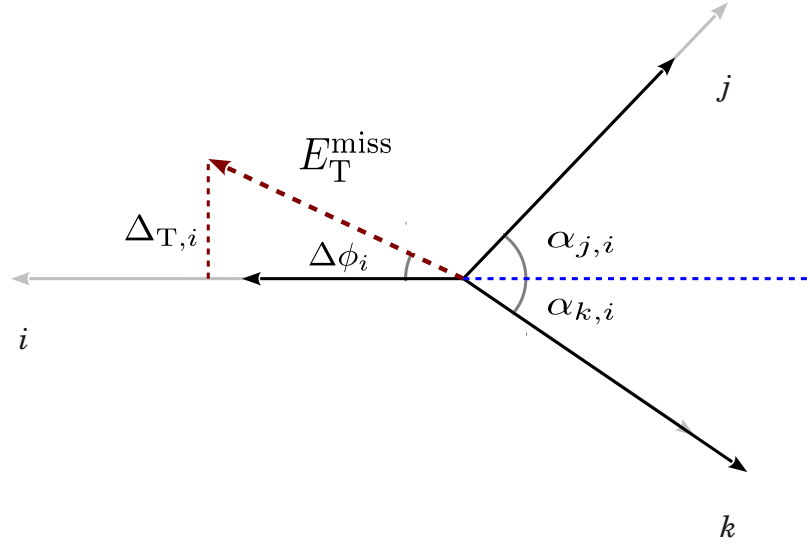


Figure 5.3: Illustration of the quantities used in the computation of $\Delta\hat{\phi}_{\text{min}}$. The gray (black) arrows indicate the true (measured) magnitude of the momentum of each jet. In this case, jet i is largely mismeasured, inducing a large value of E_T^{miss} in its vicinity.

We compute the expected component of E_T^{miss} perpendicular to jet i , denoted $\Delta_{T,i}$, by adding the expected sizes of the mismeasurement of the other jets, as follows. Each jet j ($j \neq i$) contributes an average amount to the component of E_T^{miss} perpendicular to jet i that is given by $\Delta_{j,i} = \sigma(p_T^j) \cdot \sin(\alpha_{j,i})$, where $\sigma(p_T^j)$ is the energy resolution of jet j and $\alpha_{j,i}$ is the angle depicted in Figure 5.3. The mismeasurements of the jets are independent of each other, so the total component

of E_T^{miss} perpendicular to jet i is estimated as:

$$\Delta_{T,i} = \sqrt{\sum_{j \neq i} (\Delta_{j,i})^2} \quad (5.2)$$

$$\approx \sqrt{\sum_{j \neq i} \left(0.1 \cdot p_{T,j} \cdot \frac{|\vec{p}_{T,i} \times \vec{p}_{T,j}|}{p_{T,i} \cdot p_{T,j}} \right)^2} \quad (5.3)$$

$$= \left(\frac{0.1}{p_{T,i}} \right) \sqrt{\sum_{j \neq i} |\vec{p}_{T,i} \times \vec{p}_{T,j}|^2}, \quad (5.4)$$

where we approximate the relative energy resolution of jet j to be about 10%, i.e. $\sigma(p_T^j) \approx 0.1 \cdot p_T^j$ [32]. Thus, we can compute the expected angle between E_T^{miss} and jet i as

$$\sigma_{\Delta\phi_i} = \arcsin\left(\frac{\Delta_{T,i}}{E_T^{\text{miss}}}\right) \approx \arctan\left(\frac{\Delta_{T,i}}{E_T^{\text{miss}}}\right), \quad (5.5)$$

where we make the small-angle approximation, which is valid for the large majority of QCD events. We then define the ratio $\Delta\hat{\phi}_i = \Delta\phi_i/\sigma_{\Delta\phi_i}$. In the scenario depicted in Fig. 5.3, the value of $\Delta\hat{\phi}_i$ for jet i is roughly unity, since we expect $\sigma_{\Delta\phi_i}$ to be a good approximation of $\Delta\phi_i$. Repeating the above computation for the other jets j and k , we typically find that $\Delta\hat{\phi}_j$ and $\Delta\hat{\phi}_k$ are each greater than unity, since the angles $\Delta\phi_j$ and $\Delta\phi_k$ are relatively large and the expected angles $\sigma_{\Delta\phi_j}$ and $\sigma_{\Delta\phi_k}$ are underestimated due to the severe mismeasurement of jet i . Thus, we expect that the smallest value of $\Delta\hat{\phi}_l$, for *any* jet l in the event, to be near unity and to correspond to the mismeasured jet i .

For events with E_T^{miss} arising from a neutrino, such as $t\bar{t}$ and W boson events, we also expect $\Delta\hat{\phi}_i$ to have values larger than unity, since the neutrino will not tend to be aligned with any of the jets. Thus, we define $\Delta\hat{\phi}_{\text{min}}$ as the minimum value of $\Delta\hat{\phi}_i$ over the three highest p_T jets in the event, and expect this variable to show a strong discrimination between QCD and non-QCD events. For comparison purposes, we define $\Delta\phi_{\text{min}}$ as the minimum value of $\Delta\phi_i$ over the same jets.

For the QCD event in Fig 5.3, the greater the under-measurement of jet i , the larger the magnitude of the induced \vec{E}_T^{miss} and the smaller the angle $\Delta\phi_i$. Thus, we expect E_T^{miss} and $\Delta\phi_i$ to be strongly anti-correlated. However, the value of $\Delta_{T,i}$ remains unchanged, as it only depends on the direction of jet i and on the other jets in the event. Thus, we expect $\sigma_{\Delta\phi_i}$ to scale in the same way as $\Delta\phi_i$ as the E_T^{miss} increases. Fig. 5.4 compares the shapes of $\Delta\phi_{\text{min}}$ and $\Delta\hat{\phi}_{\text{min}}$ in exclusive bins of E_T^{miss} . We observe a significant dependence of the $\Delta\phi_{\text{min}}$ shape on the E_T^{miss} bin, while for the case of $\Delta\hat{\phi}_{\text{min}}$ the dependence is largely removed.

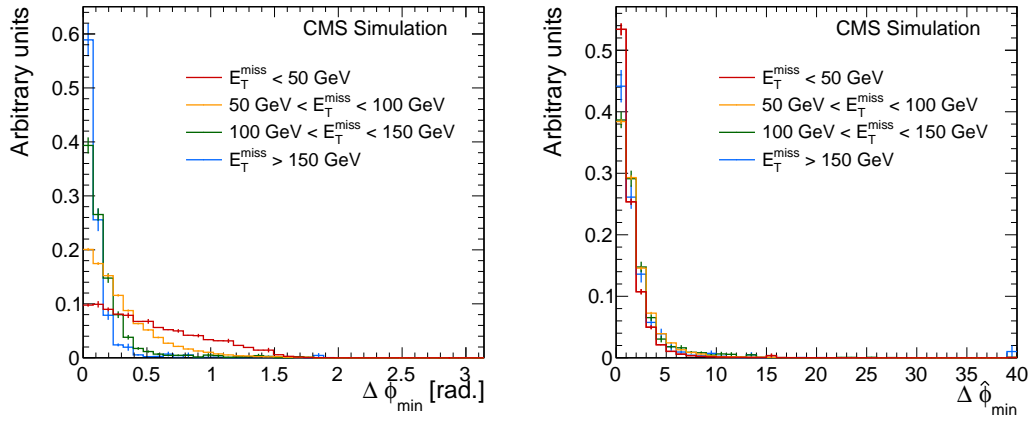


Figure 5.4: Distribution of $\Delta\phi_{\text{min}}$ (left) and $\Delta\hat{\phi}_{\text{min}}$ (right) in bins of E_T^{miss} in the QCD MC. The shape of the distribution is largely independent of E_T^{miss} for the case of $\Delta\hat{\phi}_{\text{min}}$.

To further illustrate the independence between E_T^{miss} and $\Delta\hat{\phi}_{\text{min}}$, we show in the top-left (top-right) plot of Fig. 5.5 the ratio of the number of events in the QCD MC passing a $\Delta\phi_{\text{min}} > 0.3$ ($\Delta\hat{\phi}_{\text{min}} > 4$) cut to the number of events failing the cut. We refer to this quantity as the pass-fail ratio. The independence between $\Delta\hat{\phi}_{\text{min}}$ and E_T^{miss} is seen by the flatness of the pass-fail ratio when plotted as a function of E_T^{miss} . We find that this independence extends to very high values of E_T^{miss} . Moreover, the bottom plot of Fig 5.5 illustrates that, for the case of $\Delta\hat{\phi}_{\text{min}}$, the pass-fail ratio is independent of the b jet requirement of the event.

This property is exploited in the prediction of the QCD background, which we discuss in the next section. The search regions defined in Sec. 5.3 include the requirement $\Delta\hat{\phi}_{\min} > 4$.

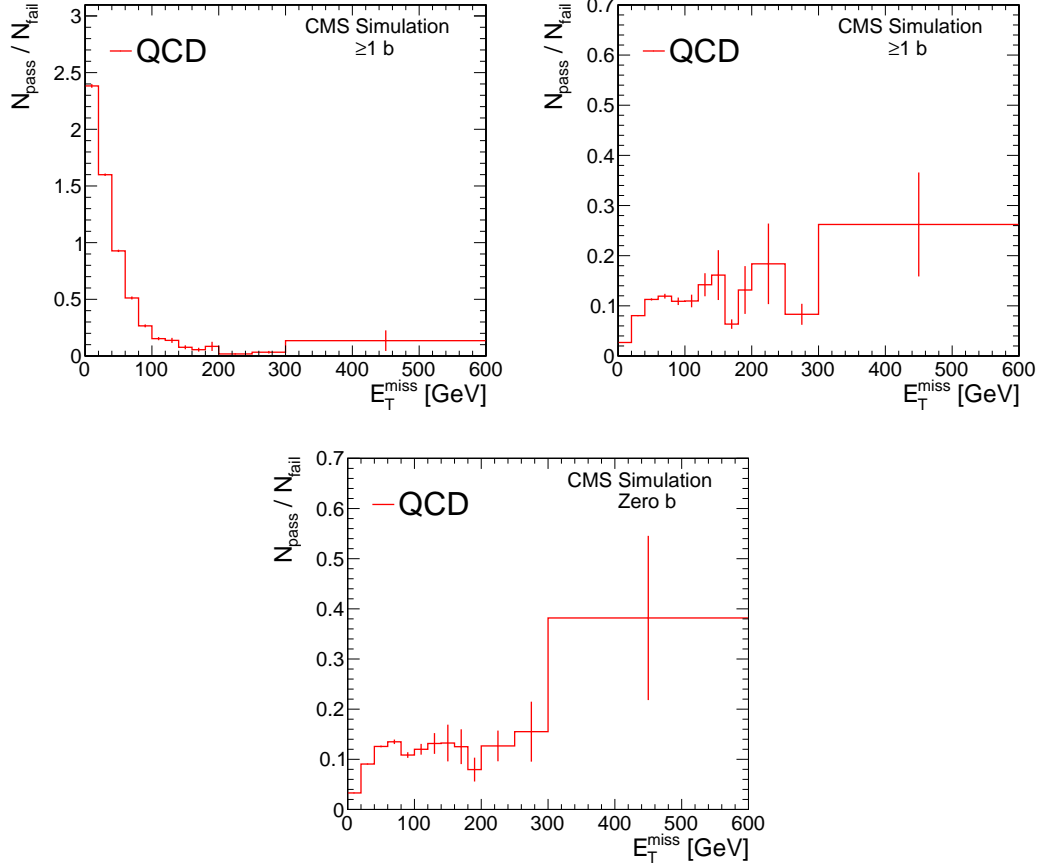


Figure 5.5: The pass-fail ratio for $\Delta\phi_{\min}$ (top-left) and $\Delta\hat{\phi}_{\min}$ (top-right) in bins of E_T^{miss} for the 1BL selection. A strong dependence on E_T^{miss} is shown for the case of $\Delta\phi_{\min}$, while the pass-fail ratio is largely constant for $E_T^{\text{miss}} \gtrsim 50$ GeV for the case of $\Delta\hat{\phi}_{\min}$. The bottom plot shows the pass-fail ratio for $\Delta\hat{\phi}_{\min}$ in the same selection, except for a $0b$ requirement.

5.5.2 QCD-background method

To estimate the QCD background remaining after the nominal $\Delta\hat{\phi}_{\min} > 4$ requirement, we make use of the observation that E_T^{miss} and $\Delta\hat{\phi}_{\min}$ are uncorrelated variables. We measure the pass-fail ratio from two low- E_T^{miss} regions (denoted the LSB and LSB-LDP regions) and apply the ratio to a high- E_T^{miss} , low- $\Delta\hat{\phi}_{\min}$ control region, which we denote as the SIG-LDP region in Table 5.5. In particular, we use the following relation:

$$N_{\text{SIG}}^{\text{QCD}} = N_{\text{SIG-LDP}}^{\text{QCD}} \cdot \frac{N_{\text{LSB}}^{\text{QCD}}}{N_{\text{LSB-LDP}}^{\text{QCD}}} = N_{\text{SIG-LDP}}^{\text{QCD}} \cdot R^{\text{QCD}}, \quad (5.6)$$

where we define $R^{\text{QCD}} \equiv \frac{N_{\text{LSB}}^{\text{QCD}}}{N_{\text{LSB-LDP}}^{\text{QCD}}}$ as the pass-fail ratio from the low- E_T^{miss} control regions. The precise definitions of the LSB and LSB-LDP regions is given in the next section. An analogous relation applies for the prediction of the QCD background in the SB region, $N_{\text{SB}}^{\text{QCD}}$, which is needed for the estimate of the top and W +jets background. A schematic diagram of the estimate procedure is given in Fig. 5.6.

5.5.3 QCD control samples

Before testing the method with the QCD MC, we first verify that the simulation does a reasonable job in modeling the data in the control regions that are populated by QCD events. Fig. 5.7 shows a comparison between the data and MC of the distribution of $\Delta\hat{\phi}_{\min}$ in the SB and SB-LDP regions. As expected, we find QCD events to have a distribution strongly peaked near $\Delta\hat{\phi}_{\min} = 1$. We also find that the shape of the $\Delta\hat{\phi}_{\min}$ distribution is reasonably well-modeled by the MC. As another check, we compare the QCD MC with a data sample collected

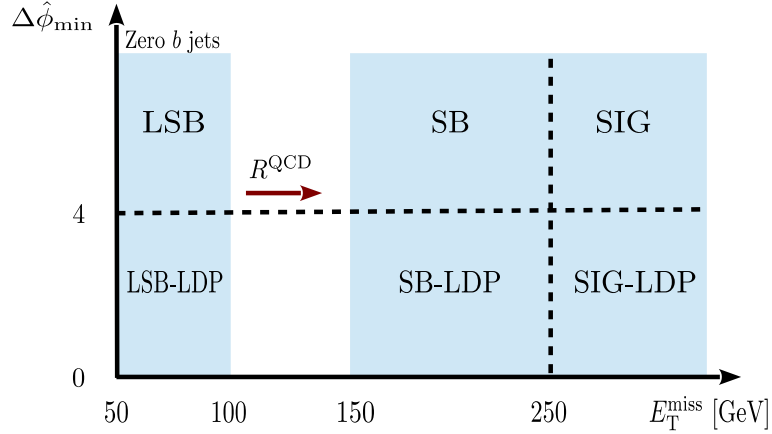


Figure 5.6: Schematic diagram of the QCD estimate procedure and the relevant regions. The lower E_T^{miss} boundary of the signal region in this diagram corresponds to the 1BL, 2BL, and 3B selections.

with only an H_T requirement at the trigger level. We refer to such a trigger as an inclusive- H_T trigger. We define the Lower Sideband (LSB) region to be the set of events collected by these triggers that satisfy all nominal selection criteria, with the exception of a $50 \text{ GeV} < E_T^{\text{miss}} < 100 \text{ GeV}$ and zero b jet requirement. Similarly, we define the LSB-LDP region to be identical to the LSB region, except with $\Delta\hat{\phi}_{\text{min}} < 4$. These regions are shown schematically in Fig. 5.6. The use of the inclusive- H_T triggers is required in order to collect events in such a low- E_T^{miss} region, which would not be possible with the nominal trigger. The zero b jet requirement is applied to ensure a very pure sample of QCD events. Fig. 5.8 shows a comparison of the data with the MC in the LSB region. As expected, this region is completely dominated by QCD events. We find fair agreement between the QCD MC and the data over several orders of magnitude. We also verify from the inclusive- H_T sample that the pass-fail ratio is flat as a function of E_T^{miss} and is described reasonably well by the MC. This is shown in Fig. 5.9, where we find for $E_T^{\text{miss}} \gtrsim 50 \text{ GeV}$ that the ratio is indeed constant. The results of

these comparisons add confidence that a closure test of the background method using the MC will provide a reasonable measure of the validity of the method in the data.

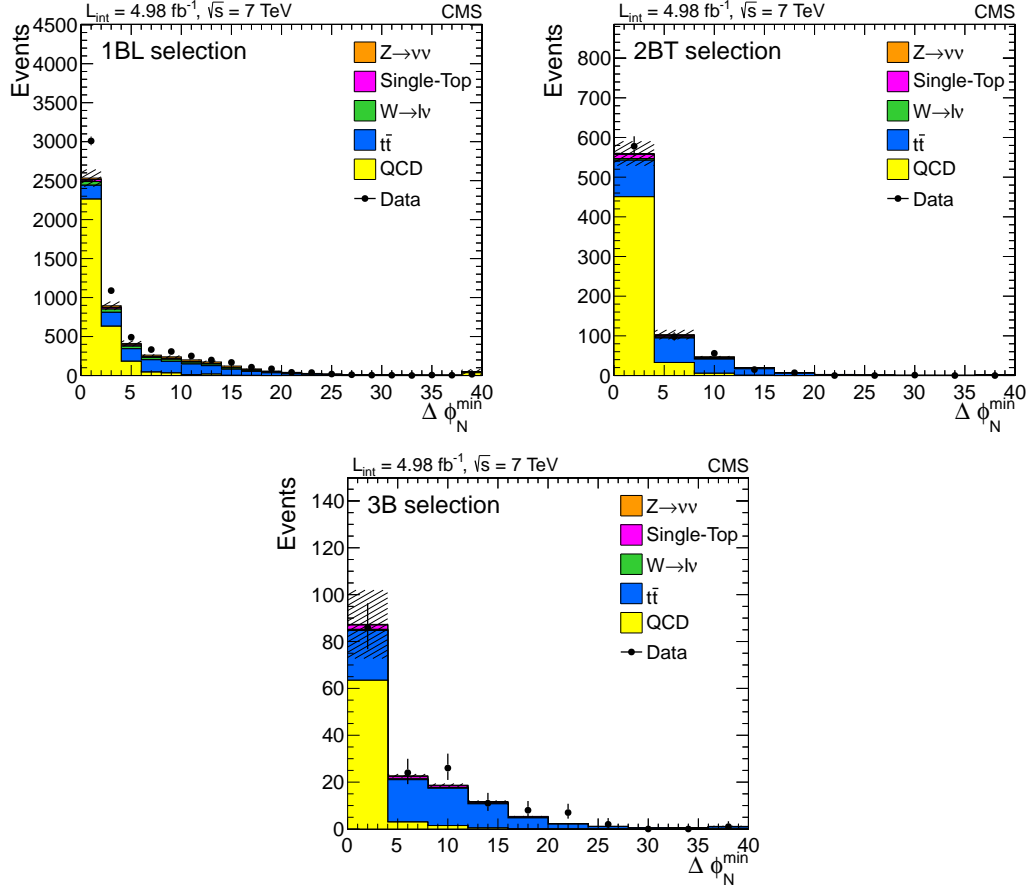


Figure 5.7: Data-MC comparison of $\Delta\hat{\phi}_{\min}$ in the SB and SB-LDP regions for the 1BL (top-left), 2BT (top-right), and 3B (bottom) selections. The hashed area gives the total statistical uncertainty on the MC.

5.5.4 Closure test of QCD prediction

To test the method described above, we apply Equation 5.6 to the QCD MC. The closure test results are shown in Table 5.8. We define closure here as the

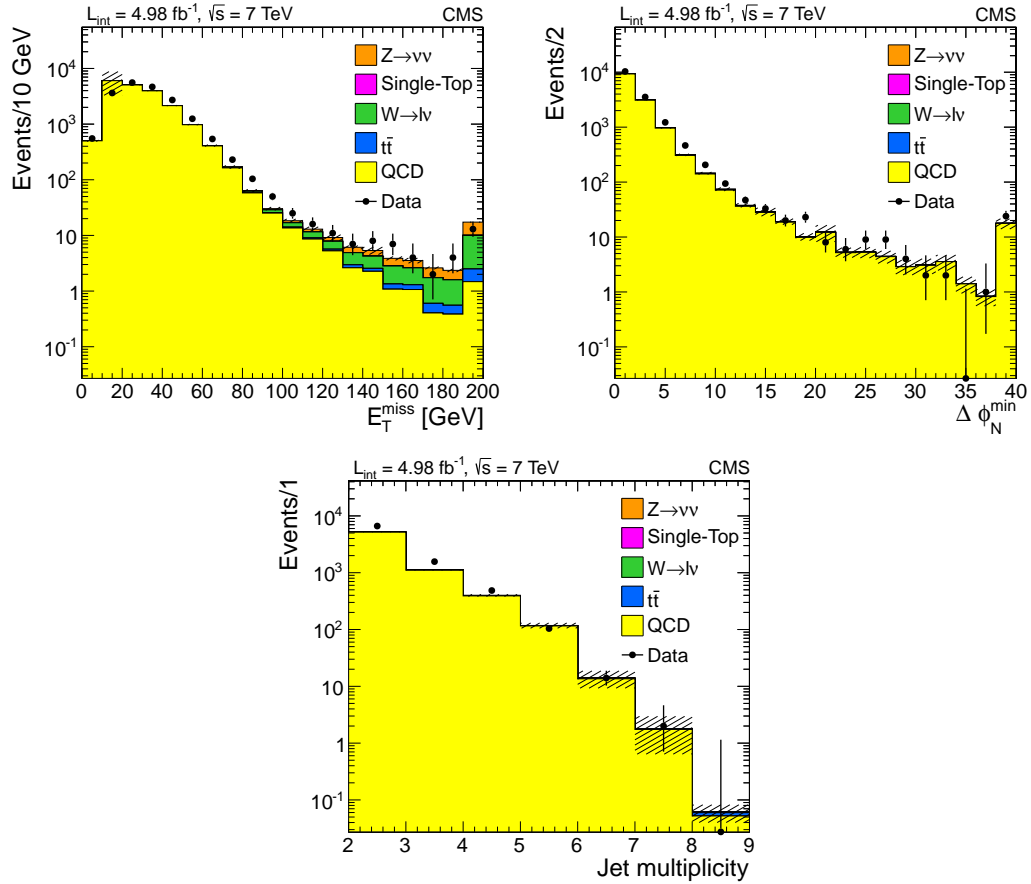


Figure 5.8: Data-MC comparison of E_T^{miss} (top-left), $\Delta\hat{\phi}_{\text{min}}$ (top-right), and the number of jets (bottom) distributions for events in the LSB region of the 1BL selection, except for the requirement on the variable that is plotted. The hashed area gives the total statistical uncertainty on the MC.

difference between the predicted and true yields, relative to the predicted yield. In general, the predicted values are consistent with the true QCD yield within the statistical uncertainty of the MC sample. We incorporate the level of closure observed in the MC into the systematic uncertainty on the QCD background prediction.

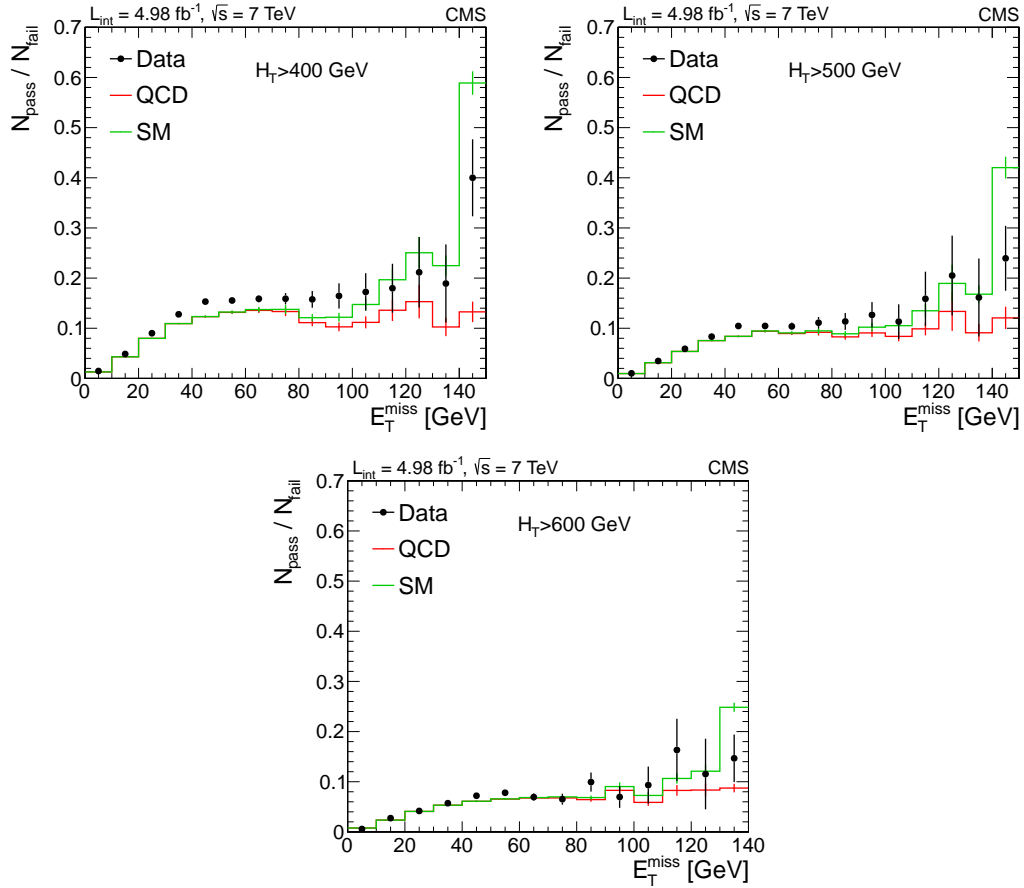


Figure 5.9: Pass-fail ratio in data collected with the inclusive- H_T sample for $H_T > 400$ GeV (top-left), $H_T > 500$ GeV (top-right), and $H_T > 600$ GeV (bottom) selections. The green histogram shows the non-QCD SM contribution stacked on top of the QCD contribution.

5.5.5 QCD prediction results

We account for several effects in the prediction of the QCD background from the data control samples. The first effect is the presence of non-QCD processes in the SIG-LDP region. The contamination comes largely from $t\bar{t}$ events, with a smaller contribution from W and Z events. We estimate the non-QCD contamination using the MC and subtract it from the data yield in that region. The second effect accounts for any difference in the trigger efficiency between the SIG and

Table 5.8: Closure test of the QCD background method in QCD MC. The closure is expressed in %.

Selection	R^{QCD}	$N_{\text{SIG-LDP}}^{\text{QCD}}$	$N_{\text{SIG}}^{\text{QCD}}(\text{pred})$	$N_{\text{SIG}}^{\text{QCD}}(\text{true})$	Closure
1BL	0.131 ± 0.002	226 ± 30	30 ± 4	28 ± 6	5 ± 24
1BT	0.092 ± 0.002	2.3 ± 1.0	0.22 ± 0.09	0.7 ± 0.2	-210 ± 170
2BL	0.131 ± 0.002	61 ± 12	8 ± 2	6 ± 1	23 ± 23
2BT	0.596 ± 0.016	13 ± 1	0.8 ± 0.1	1.7 ± 0.7	-103 ± 81
3B	0.131 ± 0.002	3.5 ± 0.5	0.45 ± 0.07	0.29 ± 0.07	35 ± 19

SIG-LDP regions. We expand Equation 5.6 to account for both these effects:

$$N_{\text{SIG}}^{\text{QCD}} = \varepsilon_{\text{SIG}} \cdot \left(\frac{N_{\text{SIG-LDP}}}{\varepsilon_{\text{SIG-LDP}}} - N_{\text{SIG-LDP}}^{\text{top+EW}} \right) \cdot R^{\text{QCD}}, \quad (5.7)$$

where $N_{\text{SIG-LDP}}^{\text{top+EW}}$ is the non-QCD contamination in the SIG-LDP region, and ε_X is the trigger efficiency in region X . An analogous relation holds for the prediction of the QCD background in the SB region. A third correction is made to the observed yields in the LSB and LSB-LDP regions. We find a dependence of the pass-fail ratio on the primary vertex multiplicity. In general, the higher the vertex multiplicity, the larger the smearing of the $E_{\text{T}}^{\text{miss}}$ away from the mismeasured jet, and the larger the pass-fail ratio. Since the inclusive- H_{T} sample is collected using a trigger that is constrained to accept events at a fixed rate, the sample contains a lower average number of pile-up interactions than the nominal sample. Thus, the primary vertex multiplicity can differ slightly between the LSB (and LSB-LDP) region and the regions collected with the nominal trigger. We reweight the observed yields based on this difference when computing R^{QCD} . Table 5.9 shows the results of the data-driven estimates.

Table 5.9: QCD background prediction in the SIG region. $N_{\text{SIG-LDP}}^{\text{top+EW}}$ is the total non-QCD contamination in the SIG-LDP region. Errors are statistical only.

Selection	R^{QCD}	$N_{\text{SIG-LDP}}$	$N_{\text{SIG-LDP}}^{\text{top+EW}}$	$N_{\text{SIG}}^{\text{QCD}}$
1BL	0.170 ± 0.004	259	97 ± 1	28 ± 3
1BT	0.117 ± 0.005	2	2.0 ± 0.2	0.0 ± 0.2
2BL	0.170 ± 0.004	57	29.8 ± 0.6	5 ± 1
2BT	0.083 ± 0.005	19	10.1 ± 0.3	0.8 ± 0.4
3B	0.170 ± 0.004	9	3.4 ± 0.1	1.0 ± 0.5

5.5.6 Systematic uncertainties on QCD prediction

Table 5.10 lists the systematic uncertainties on the QCD background prediction. The uncertainty on the non-QCD contamination in the LDP regions is estimated by evaluating the MC-related uncertainties listed in Sec. 5.8.2. In addition, we include the uncertainty on the cross-sections of each process. Based on these studies, we assign an uncertainty of 40% to the size of the non-QCD contamination. The QCD prediction is re-evaluated after varying the non-QCD component by this uncertainty.

We find the pass-fail ratio R^{QCD} to exhibit a dependence on the number of jets in the event. To assess the sensitivity of the method to this feature, we repeat the MC closure test after reweighting events in the MC based on the jet multiplicity distributions observed in the relevant regions in the data. The worst level of closure observed between the nominal closure test and the closure test with the jet multiplicity reweighted is used as a systematic uncertainty on the validity of the method.

A systematic uncertainty due to the dependence of the pass-fail ratio R^{QCD} on the distribution on the number of primary vertices (discussed in the previous section) is estimated by varying the size of the correction by $\pm 100\%$.

We test explicitly in the data the assumption of the independence of $\Delta\hat{\phi}_{\text{min}}$ and $E_{\text{T}}^{\text{miss}}$ by varying the boundary of the $E_{\text{T}}^{\text{miss}}$ range of the LSB region. We shift the lower edge of the LSB region (at 50 GeV) by ± 10 GeV. Due to the steeply-falling $E_{\text{T}}^{\text{miss}}$ spectrum, the sample size changes by roughly a factor of two in each of these shifts. The resulting variation in the value of R^{QCD} is used as an additional systematic uncertainty.

Finally, we include a systematic uncertainty due to the uncertainty on the trigger efficiency.

Table 5.10: Systematic uncertainties on the QCD estimate in the SIG region, in %. The total uncertainty is the sum in quadrature of all sources of systematic error. For the 1BT selection, the nominal estimate is zero, so the percent changes due to varying the non-QCD contamination and trigger efficiency are ill-defined. The prediction for this selection is $N_{\text{SIG}}^{\text{QCD}} = 0.1$ when the non-QCD component is reduced by 40%.

Selection	Non-QCD	Closure	LSB range	LSB PV	Trigger	Total
1BL	23	37	0.3	7.9	5.1	44
1BT	*	320	1.1	9.0	*	*
2BL	42	41	0.3	7.9	5.8	60
2BT	43	152	5.8	9.8	5.6	159
3B	25	45	0.3	7.9	5.0	52

5.6 $Z \rightarrow \nu\bar{\nu}$ background

Events with a Z boson decaying to two neutrinos contribute from 5% to 40% of the total SM background, depending on the search selection. We estimate the contribution of this background using a data control sample enriched with $Z \rightarrow e^+e^-$ and $Z \rightarrow \mu^+\mu^-$ events. We expect the kinematic properties of $Z \rightarrow l^+l^-$ events to match very well with those of $Z \rightarrow \nu\nu$ events. The two reconstructed leptons are manually “erased” from the event in order to mimic the signature of a $Z \rightarrow \nu\nu$ decay. We then recompute the $E_{\text{T}}^{\text{miss}}$ and all other affected quantities in the event, and apply the nominal selection criteria. Finally, we correct the observed yield in the control sample to account for the detector acceptance of the leptons, the lepton reconstruction and selection efficiencies, and several other effects discussed below.

5.6.1 $Z \rightarrow \nu\bar{\nu}$ control sample

A sample enriched in $Z \rightarrow l^+l^-$ events is collected with a series of triggers that require two leptons with thresholds as high as $p_{\text{T}} > 17 \text{ GeV}$ on one lepton and $p_{\text{T}} > 8 \text{ GeV}$ on the other. The full list of triggers is shown in Tables A.3 and A.4. We require the two reconstructed leptons to satisfy the offline lepton requirements listed in Sec. 5.3, but with a more stringent p_{T} threshold of $p_{\text{T}} > 17 \text{ GeV}$. The leptons are also required to be oppositely charged and form an invariant mass within 15 GeV of $m_Z = 91.2 \text{ GeV}$. With the exception of the requirement on the number of b jets, all other selection cuts described in Sec. 5.3 are applied. In order to retain sufficient statistics in the $Z \rightarrow l^+l^-$ control sample, we loosen the condition on the b jet discriminant to $d_{\text{CSV}} \geq 0.244$ and require at least 1 b jet for

all search selections. The choice of the discriminant value is chosen such that the probability of misidentifying a light-flavored or gluon jet as a b jet is around 10%. We denote b jets that satisfy this selection as loose b jets. The resulting sample is denoted the SIG-DL sample, as first introduced in Table 5.5.

In the following discussion, for events satisfying the above selection, the quantities E_T^{miss} and $\Delta\hat{\phi}_{\text{min}}$ are always the values computed *after* treating the two leptons as neutrinos. Fig 5.10 shows a comparison between the $Z \rightarrow l^+l^-$ MC and the data in the SIG-DL sample of the invariant mass of the lepton pair and the E_T^{miss} . The control sample is dominated by $Z \rightarrow l^+l^-$ events, with a small contribution from $t\bar{t}$ events. We find reasonable agreement between the data and the MC, which adds confidence that a closure test of the method (described below) performed with the MC provides an accurate measure of the validity of the estimation technique.

5.6.2 Acceptance and efficiencies

The acceptance \mathcal{A} of all $Z \rightarrow l^+l^-$ events passing the geometric and kinematic requirements on the leptons is evaluated from the $Z \rightarrow l^+l^-$ MC. The value of \mathcal{A} is found to depend on the choice of offline cuts applied. For example, imposing a large value of E_T^{miss} (after lepton removal) preferentially selects events with high- p_T leptons. We therefore compute \mathcal{A} after applying all nominal kinematic cuts. The values of \mathcal{A} for the various selections is given in Table 5.13.

We define $\varepsilon_{\text{reco}}$ to be the efficiency for a lepton to be reconstructed, and ε_{sel} the efficiency for a reconstructed lepton to pass the selection requirements of Sec. 5.3. Thus, the efficiency to identify two leptons in a $Z \rightarrow l^+l^-$ event can be

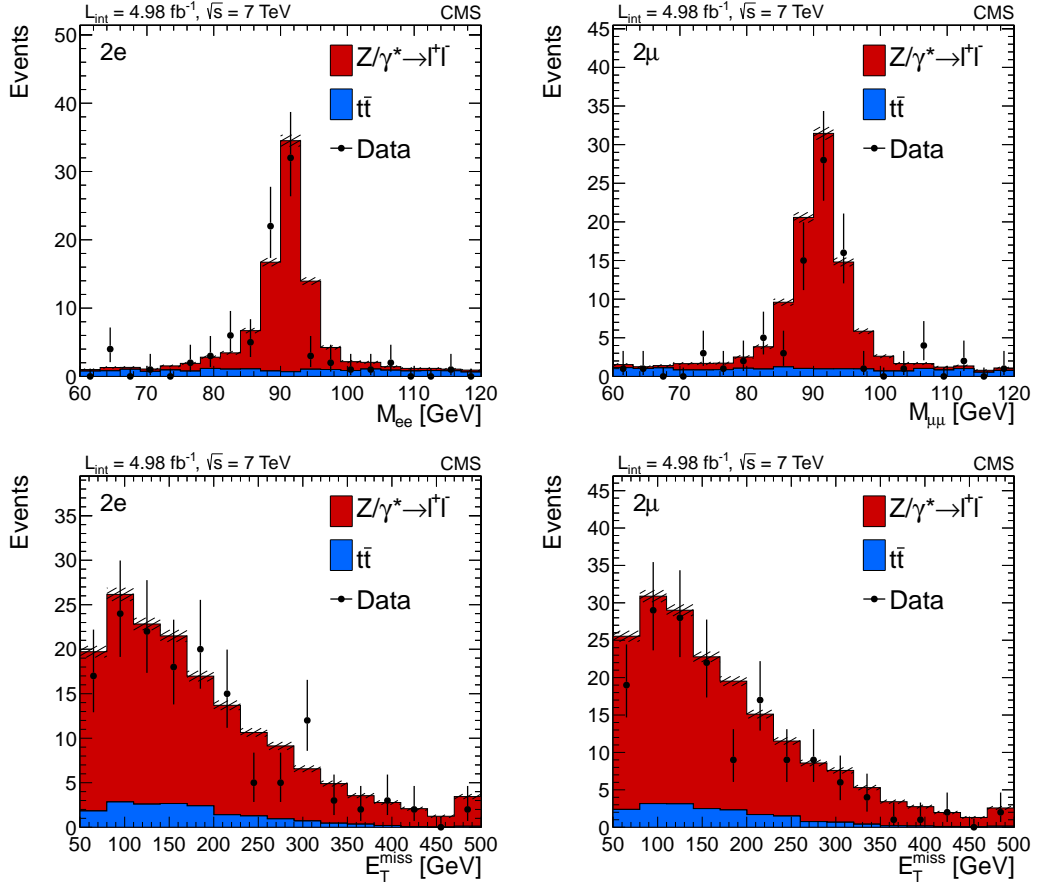


Figure 5.10: Data-MC comparison of the invariant mass of the two leptons (top row) and E_T^{miss} distributions (bottom row) of the SIG-DL region. The $Z \rightarrow e^+e^-$ ($Z \rightarrow \mu^+\mu^-$) selection is shown on the left (right) plots. In the invariant mass distributions, a cut of $E_T^{\text{miss}} > 150 \text{ GeV}$ is applied. The hashed area gives the total statistical uncertainty on the MC.

factorized as:

$$\varepsilon = \varepsilon_{\text{reco}}^2 \cdot \varepsilon_{\text{sel}}^2 \cdot \varepsilon_{\text{trig}}, \quad (5.8)$$

where $\varepsilon_{\text{reco}}^2$ is the efficiency for both leptons to be reconstructed, $\varepsilon_{\text{sel}}^2$ the efficiency for both reconstructed leptons to pass the lepton selection cuts, and $\varepsilon_{\text{trig}}$ the efficiency for both identified leptons to pass the trigger requirement. We factorize the efficiency in this way, particularly with the trigger condition as the *last* requirement, so that we may compute the efficiencies directly from the data in the

method described below.

We measure the lepton reconstruction efficiency using a “tag-and-probe” technique on $Z \rightarrow l^+l^-$ events [44]. For the case of electrons, the reconstruction efficiencies are measured to be $\varepsilon_{\text{reco,EB}} = 0.993 \pm 0.014$ and $\varepsilon_{\text{reco,EE}} = 0.968 \pm 0.034$ [45] for electrons found in the ECAL barrel and endcap regions, respectively. We take the average of these two values, weighted by the proportion of electrons-from- Z that are found in the barrel and endcap regions, to get $\varepsilon_{\text{reco}} = 0.987 \pm 0.014$. For the case of muons, the reconstruction efficiency is further factorized as

$$\varepsilon_{\text{reco}} = \varepsilon_{\text{track}} \cdot \varepsilon_{\text{ID}}, \quad (5.9)$$

where $\varepsilon_{\text{track}} = 0.988 \pm 0.005$ [46] is the efficiency for a muon to leave a track in the tracker system, and $\varepsilon_{\text{ID}} = 0.997 \pm 0.002$ [44] is the efficiency for a muon with a reconstructed track to be identified as a muon.

We apply the same technique to measure the lepton selection efficiency, using data collected from an independent jet-based trigger. We require one “tag” lepton to have $p_{\text{T}} > 20 \text{ GeV}$ and satisfy the lepton selection requirements of Sec. 5.3. The second “probe” lepton in the event is required to only be reconstructed and within the kinematic and geometric acceptance conditions of the SIG-DL region. The efficiency ε_{sel} can then be measured as the fraction of “probe” leptons that satisfy the full lepton selection. However, there is a non-negligible contribution of fake leptons that can satisfy the “probe” selection, where fake refers to any reconstructed object that is not a lepton-from- Z . Therefore, we extract the number of true leptons-from- Z by fitting to the distribution of the invariant mass of the lepton pair. We take the shape of the mass distribution for true $Z \rightarrow l^+l^-$ events from the $Z \rightarrow l^+l^-$ MC. This shape is convoluted with a Gaussian distribution to account for any difference in the detector resolu-

tion between the data and the MC. An exponential function is used to model the mass distribution from fake lepton pairs. The fit results are shown in Fig. 5.11. We measure a selection efficiency of $\varepsilon_{\text{sel}} = 0.78 \pm 0.03$ (0.81 ± 0.01) for the case of electrons (muons).

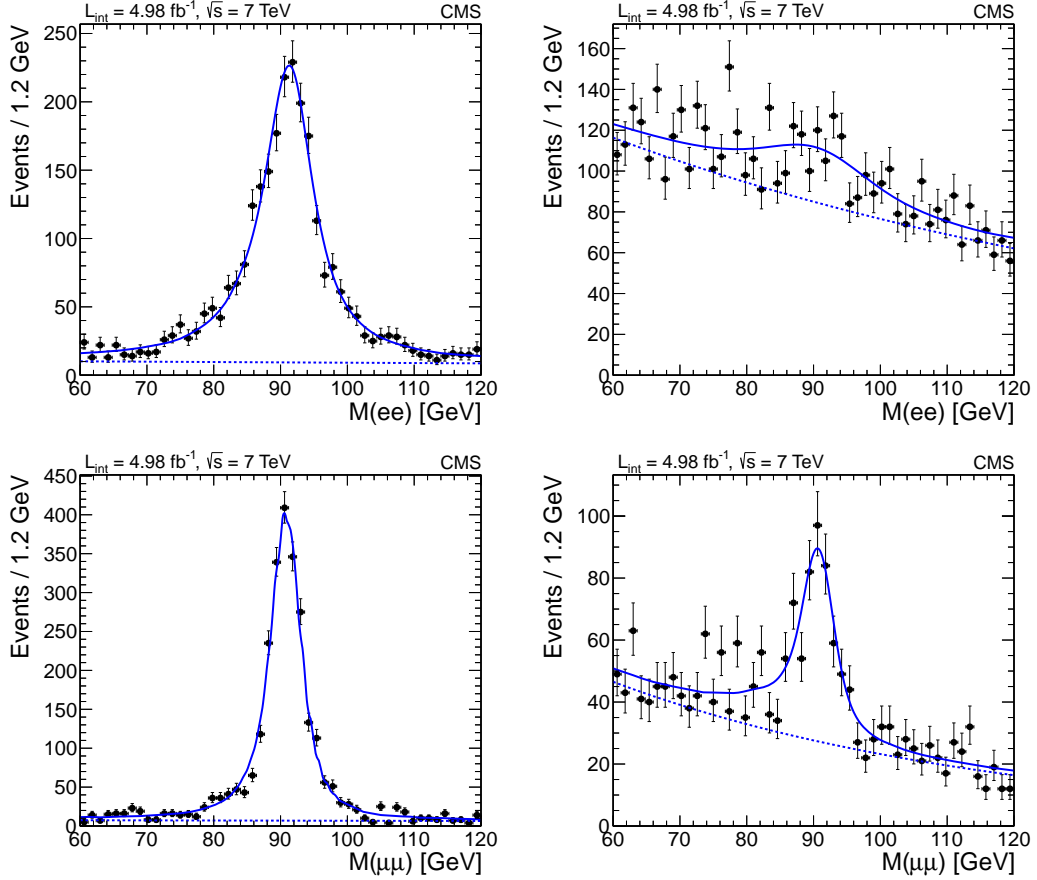


Figure 5.11: Invariant mass distribution of the lepton pairs used for the measurement of ε_{sel} . The top (bottom) plots show the distribution for electron (muon) pairs. The left (right) plots show the distribution of pairs for which the “probe” lepton passes (fails) the lepton selection of the SIG-DL region. The dashed line shows the fit result for the background component (i.e. fake lepton pairs).

The trigger efficiency $\varepsilon_{\text{trig}}$ is also measured using events collected from a jet-based trigger. We require the events to have two leptons that pass the full lepton requirements of the SIG-DL region. We measure the efficiency directly as the

fraction of these events that satisfy the double-lepton triggers used for the SIG-DL region. We find an efficiency of $\varepsilon_{\text{trig}} = 1.00_{-0.01}^{+0}$ (0.87 ± 0.04) for the case of $Z \rightarrow e^+e^-$ ($Z \rightarrow \mu^+\mu^-$) events. The higher trigger efficiency for the $Z \rightarrow e^+e^-$ case is due to the relatively looser requirements on the electron at the trigger level.

5.6.3 b jet extrapolation factor

The extrapolation factor

$$\mathcal{F} = \mathcal{F}(n) = \frac{N(\geq n \text{ } b \text{ jets})}{N(\geq 1 \text{ loose } b \text{ jet})} \quad (5.10)$$

is needed to scale the observed data yields in the SIG-DL sample to a corresponding sample with the same b jet requirement as in the search selection. We observe in both the data and the MC that \mathcal{F} is largely independent of the $E_{\text{T}}^{\text{miss}}$ and H_{T} of an event. For the case of $E_{\text{T}}^{\text{miss}}$, this can be understood from the fact that the largest contribution to the $E_{\text{T}}^{\text{miss}}$ in the $Z \rightarrow l^+l^-$ control sample arises from the p_{T} of the leptons (since they are treated as neutrinos). The kinematics of the leptons, and therefore the $E_{\text{T}}^{\text{miss}}$, should be uncorrelated with the probability of a loose b jet in the event to satisfy the nominal b jet requirement. For the case of H_{T} , we find that the probability of a loose b jet to satisfy the nominal b jet requirement is also largely independent of the presence of other jets in the event. This independence is illustrated in Fig. 5.12 and 5.13 for the case of $E_{\text{T}}^{\text{miss}}$ and H_{T} , respectively. The overall disagreement in the value of \mathcal{F} between data and MC in these plots arises from the known difference in the heavy flavor content of Z +jets events between the data and simulation. In Fig. 5.14, we show a comparison of the distribution of the discriminant of the b jet algorithm in a low $E_{\text{T}}^{\text{miss}}$ region of $50 \text{ GeV} < E_{\text{T}}^{\text{miss}} < 150 \text{ GeV}$ (denoted as the LSB'-DL region)

of the $Z \rightarrow l^+l^-$ sample and the nominal E_T^{miss} (SIG-DL) region. We find good agreement between the two regions in both the data and the MC. In addition, the distributions agree well in the corresponding regions of the $Z \rightarrow \nu\nu$ MC. In Fig. 5.14, the LSB' region of the $Z \rightarrow \nu\nu$ plot corresponds to the selection criteria of the SIG region, except with the E_T^{miss} requirement of the LSB'-DL region defined above. We measure \mathcal{F} for the 1BL, 1BT, and 2BL selections from the LSB'-DL region, while for the 2BT (3B) selections we loosen as well the H_T cut to $200 \text{ GeV} < H_T < 400 \text{ GeV}$ ($100 \text{ GeV} < H_T < 200 \text{ GeV}$) for the measurement of \mathcal{F} to retain sufficient statistics.

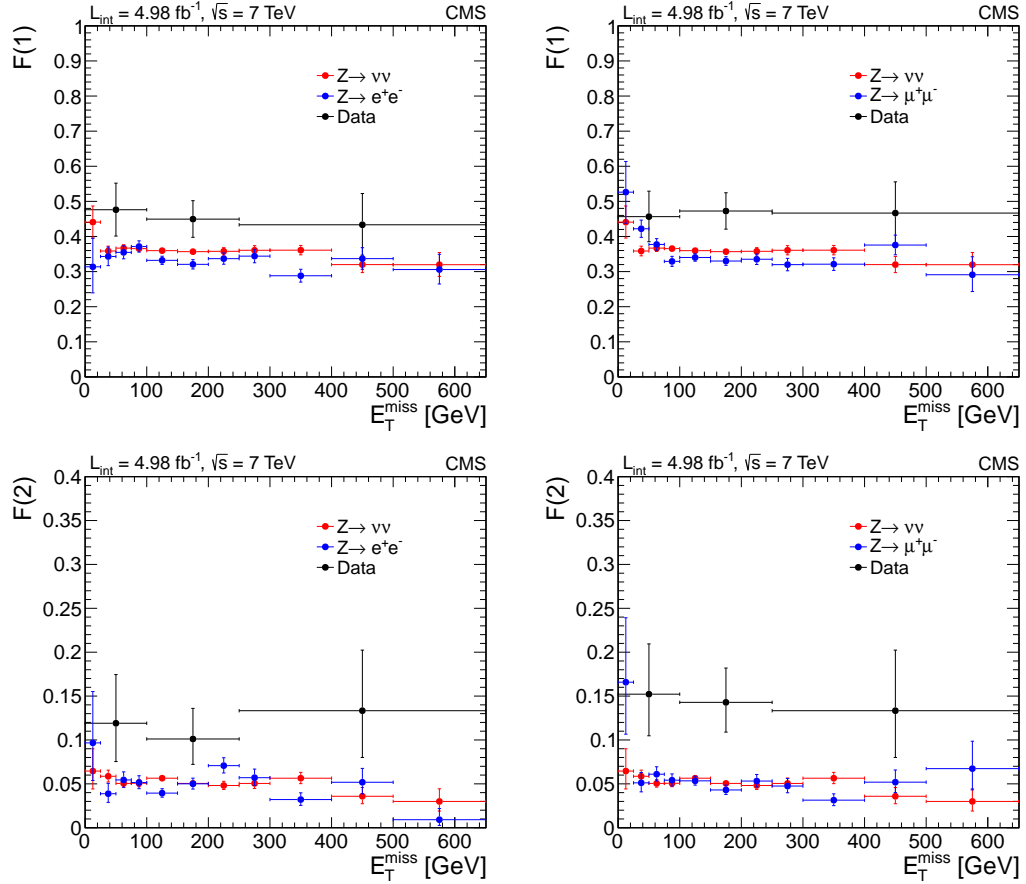


Figure 5.12: $\mathcal{F}(n)$ vs E_T^{miss} for $Z \rightarrow e^+e^-$ (left) and $Z \rightarrow \mu^+\mu^-$ (right) events in the $\geq 1 b$ (top) and $\geq 2 b$ (bottom) selections. The black (blue) points show the measured values from the data (MC). The red points show the corresponding values from the $Z \rightarrow \nu\nu$ MC.

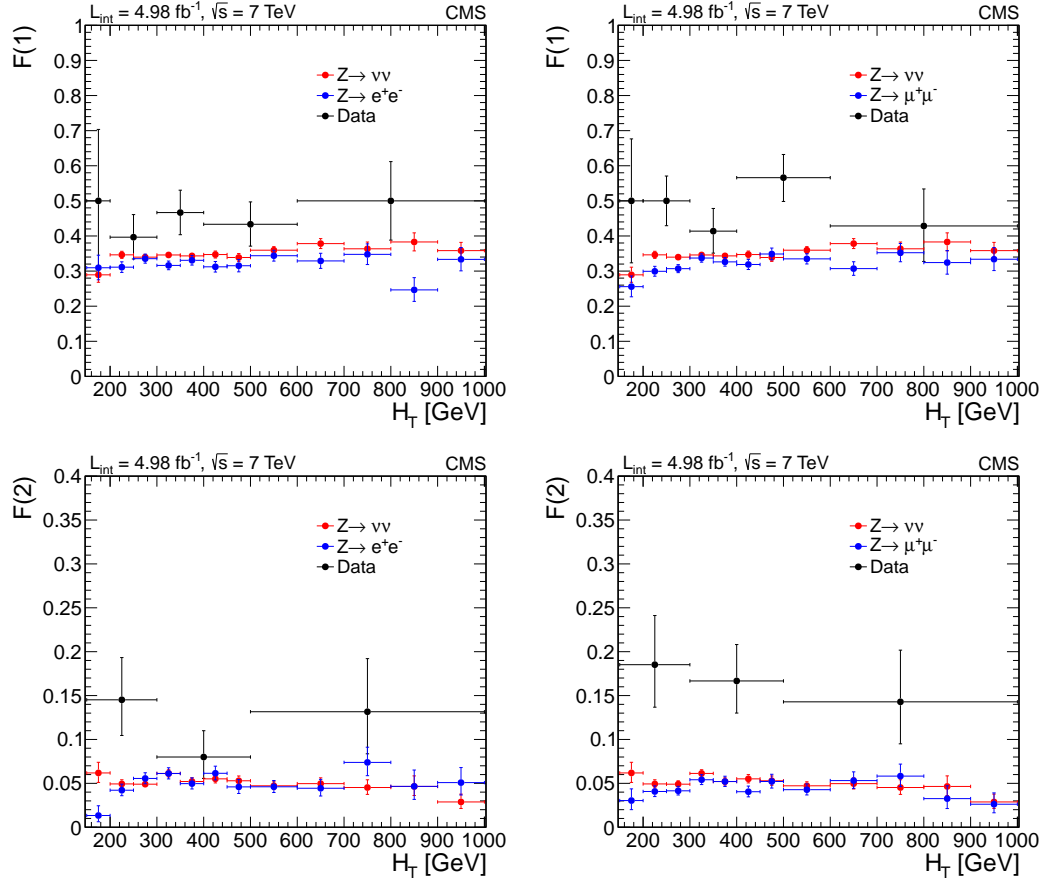


Figure 5.13: $\mathcal{F}(n)$ vs H_T for $Z \rightarrow e^+e^-$ (left) and $Z \rightarrow \mu^+\mu^-$ (right) events in the $\geq 1 b$ (top) and $\geq 2 b$ (bottom) selections, with $E_T^{\text{miss}} > 150$ GeV. The black (blue) points show the measured values from the data (MC). The red points show the corresponding values from the $Z \rightarrow \nu\nu$ MC.

5.6.4 $Z \rightarrow l^+l^-$ purity

The SIG-DL region contains a small amount of contamination from $t\bar{t}$ events. We measure the $Z \rightarrow l^+l^-$ purity of the region by performing a fit to the distribution of the invariant mass of the lepton pair in this region. The shape of the distribution for true $Z \rightarrow l^+l^-$ events is determined from a pure $Z \rightarrow l^+l^-$ sample in the data obtained by loosening the nominal selection requirements. We use a convolution of a Breit-Wigner distribution with a Crystal-Ball function [47] for

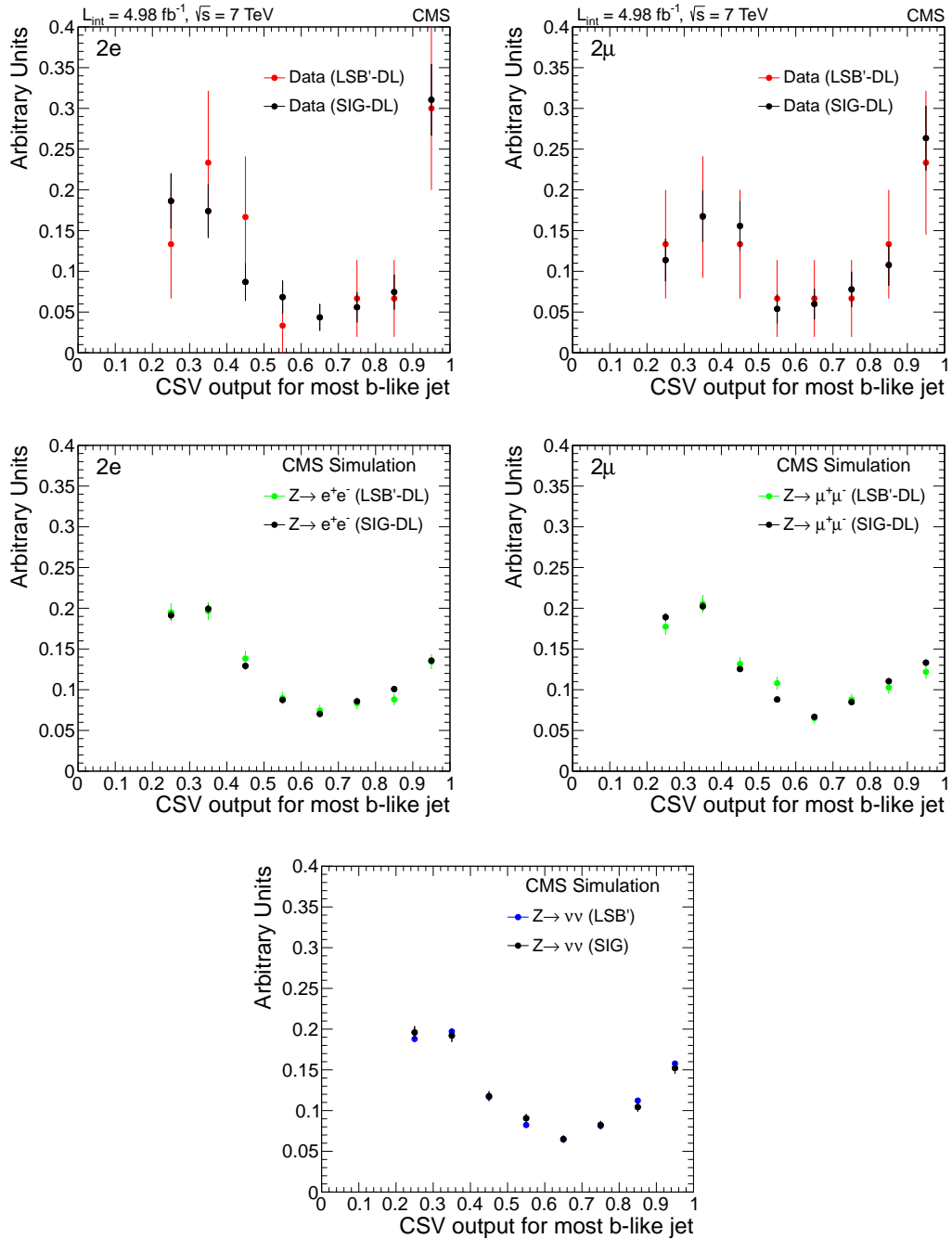


Figure 5.14: Distribution of the b jet discriminant in the $Z \rightarrow e^+e^-$ (left) and $Z \rightarrow \mu^+\mu^-$ (right) selection in the data (top row) and the MC (center row). The corresponding distribution from the $Z \rightarrow \nu\nu$ MC is shown in the bottom plot. The black (colored) points correspond to the selection for the SIG-DL (LSB'-DL) regions for the top two rows, and the selection for the SIG (LSB') regions for the bottom row.

the distribution of true $Z \rightarrow l^+l^-$ events. The fit results in the SIG-DL region are shown in Fig. 5.15. We measure a $Z \rightarrow l^+l^-$ purity of $\mathcal{P} = 0.95 \pm 0.09$ and $\mathcal{P} = 0.93 \pm 0.09$ for the case of $Z \rightarrow e^+e^-$ and $Z \rightarrow \mu^+\mu^-$ events, respectively.

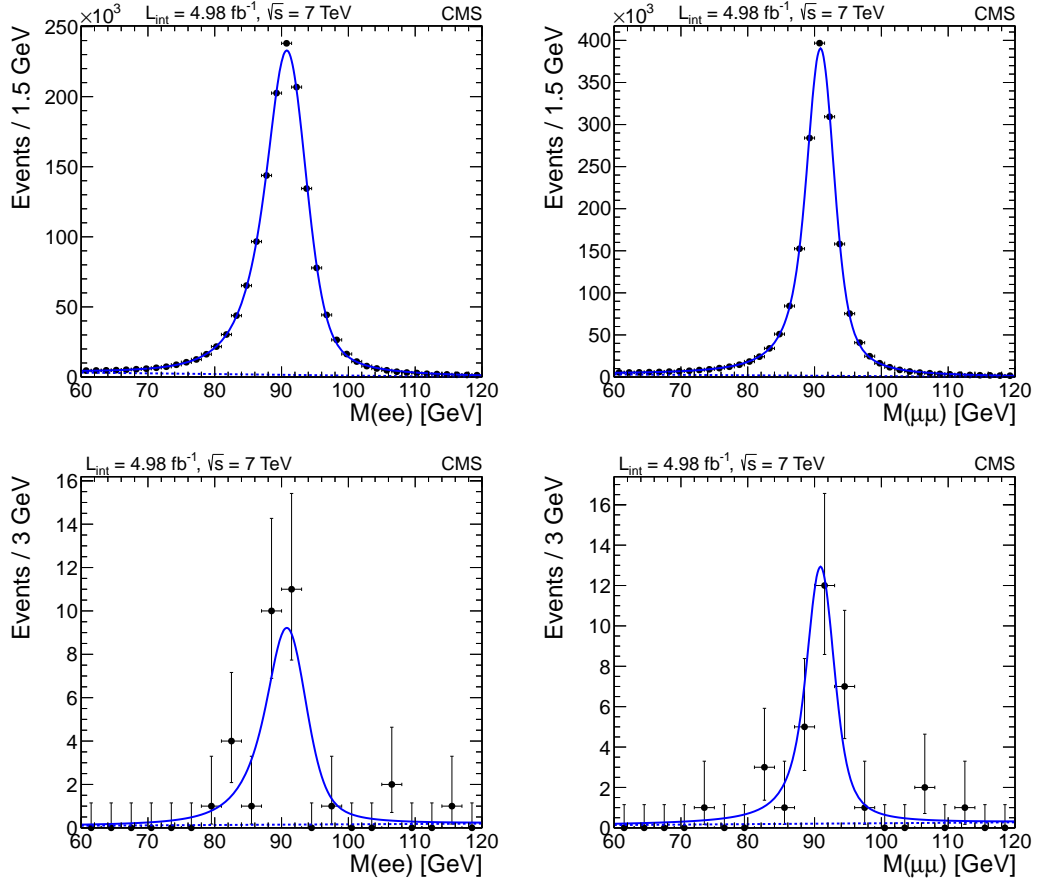


Figure 5.15: Invariant mass distribution in the pure $Z \rightarrow l^+l^-$ sample (top) and the SIG-DL region (bottom) for the $Z \rightarrow e^+e^-$ (left) and $Z \rightarrow \mu^+\mu^-$ (right) selection. The background is fitted with a linear function.

5.6.5 $Z \rightarrow \nu\bar{\nu}$ background method

The final prediction of the $Z \rightarrow \nu\bar{\nu}$ background is computed as follows. We scale the observed $Z \rightarrow l^+l^-$ yield in the SIG-DL region by the proportion of

the branching ratios of $Z \rightarrow \nu\nu$ and $Z \rightarrow l^+l^-$ decay: $\mathcal{R} = BR(Z \rightarrow \nu\nu)/BR(Z \rightarrow l^+l^-) = 5.95 \pm 0.02$ [1]. Furthermore, we account for the fraction of $Z \rightarrow l^+l^-$ events that were not identified by scaling the yield with the acceptance \mathcal{A} and efficiencies of the two identified leptons. In addition, we scale the yield by the b jet extrapolation factor \mathcal{F} to account for the loosened b jet requirement of the control sample. We make a final correction that accounts for the contamination of $t\bar{t}$ events in the $Z \rightarrow l^+l^-$ control sample. Thus, the fully-corrected $Z \rightarrow \nu\nu$ prediction is given by:

$$N_{\text{SIG}}^{Z \rightarrow \nu\nu} = N_{\text{SIG-DL}} \cdot \frac{\mathcal{R} \cdot \mathcal{F} \cdot \mathcal{P}}{\mathcal{A} \cdot \varepsilon}, \quad (5.11)$$

where the efficiency ε is given in Eq. 5.8. An analogous relation holds for the $Z \rightarrow \nu\nu$ prediction in the SB region, which is needed in the prediction of the top and W +jets background.

5.6.6 Closure test of $Z \rightarrow \nu\nu$ prediction

The key assumption to the $Z \rightarrow \nu\nu$ background prediction method is that the $E_{\text{T}}^{\text{miss}}$ distribution of $Z \rightarrow l^+l^-$ and $Z \rightarrow \nu\nu$ events is the same once the reconstructed leptons are treated as neutrinos. Figure 5.16 shows a comparison of the $E_{\text{T}}^{\text{miss}}$ distribution between $Z \rightarrow l^+l^-$ and $Z \rightarrow \nu\nu$ events in the MC, as well as the distribution observed in the $Z \rightarrow l^+l^-$ sample in the data. In general, we find fair agreement between the $Z \rightarrow l^+l^-$ and $Z \rightarrow \nu\nu$ distributions, although a slight bias towards higher values of $E_{\text{T}}^{\text{miss}}$ is seen for $Z \rightarrow l^+l^-$ events. This effect is discussed and quantified in the closure test below.

We test the accuracy of the method using the $Z \rightarrow l^+l^-$ and $Z \rightarrow \nu\nu$ MC. The results are shown in Table 5.11. A non-closure of 30-50% is observed across

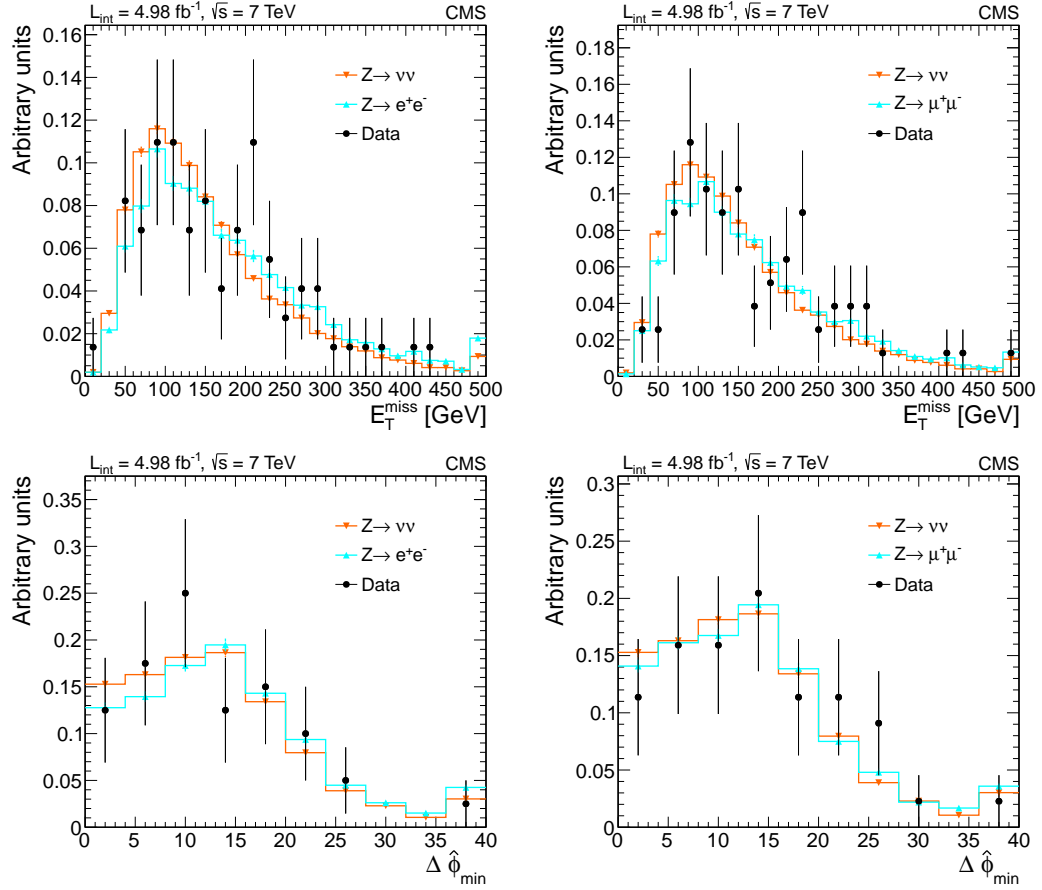


Figure 5.16: Comparison of the E_T^{miss} (top) and $\Delta\hat{\phi}_{\text{min}}$ (bottom) distributions between $Z \rightarrow \nu\nu$ MC and $Z \rightarrow l^+l^-$ events in both data and MC, for the $Z \rightarrow e^+e^-$ (left) and $Z \rightarrow \mu^+\mu^-$ (right) selections. The distributions are normalized to unit area. All other nominal 1BL selection cuts are applied, with the exception of a $E_T^{\text{miss}} > 150 \text{ GeV}$ requirement for the bottom plots.

the various selections. We find the source of non-closure to be primarily from events for which one (or both) of the neutrinos are out of acceptance. Such events have a E_T^{miss} spectrum that is not well-modeled by the $Z \rightarrow l^+l^-$ control sample, since both leptons must (by definition) be in acceptance in the $Z \rightarrow l^+l^-$ sample. Therefore, the distribution of E_T^{miss} from the $Z \rightarrow l^+l^-$ sample does not take the shape of this component of the $Z \rightarrow \nu\bar{\nu}$ background into account. The size of the bias observed in the closure test is treated as a systematic uncertainty,

as discussed in the next section.

5.6.7 Systematic uncertainties on $Z \rightarrow \nu\nu$ prediction

The dominant systematic uncertainties of the $Z \rightarrow \nu\nu$ prediction arise from the uncertainty in the level of closure of the method and in the value of the extrapolation factor \mathcal{F} . Table 5.12 summarizes the systematic uncertainties on the $Z \rightarrow \nu\bar{\nu}$ prediction.

To evaluate a systematic uncertainty associated with the level of closure of the method, we first repeat the closure test using values of \mathcal{F} obtained from a lower E_T^{miss} region ($50 \text{ GeV} < E_T^{\text{miss}} < 150 \text{ GeV}$) and higher E_T^{miss} region ($150 \text{ GeV} < E_T^{\text{miss}} < 250 \text{ GeV}$) relative to the LSB'-DP region defined in Sec. 5.6.3. For the case of the 2BT and 3B selections, we also repeat the closure test after measuring \mathcal{F} from a lower H_T region. These variations test the assumption of the independence of \mathcal{F} on E_T^{miss} and H_T . We assign as a systematic uncertainty the worst level of closure found from all such variations.

We assign a separate uncertainty on the extrapolation factor \mathcal{F} by evaluating in the data the change in \mathcal{F} when measured from a lower E_T^{miss} region (and lower H_T region for the case of the 2BT and 3B selections) relative to the LSB'-LDP region.

The uncertainty on the purity \mathcal{P} is evaluated by repeating the fits to the invariant mass distribution using alternative choices for the signal and background shapes. We find a variation of 10% on the value of \mathcal{P} . Similarly, we evaluate the uncertainty on the lepton selection efficiency ε_{sel} by repeating the

Table 5.11: MC closure test of the $Z \rightarrow \nu\bar{\nu}$ prediction method. Errors shown are statistical only. As in Sec. 5.5, we define the closure as the difference between the predicted and true yields, relative to the predicted yield. The closure is expressed in %.

Selection	$N_{\text{SIG-DL}}$	\mathcal{F}	\mathcal{A}	ε	$N_{\text{SIG}}^{Z \rightarrow \nu\bar{\nu}}(\text{pred})$	$N_{\text{SIG}}^{Z \rightarrow \nu\bar{\nu}}(\text{true})$	Closure
$Z \rightarrow e^+e^-$							
1BL	33.3 ± 0.8	0.347 ± 0.008	0.678 ± 0.005	0.606 ± 0.010	168 ± 7	106 ± 3	37 ± 3
1BT	2.5 ± 0.2	0.32 ± 0.01	0.78 ± 0.02	0.61 ± 0.01	10 ± 1	5.4 ± 0.7	46 ± 9
2BL	33.3 ± 0.8	0.046 ± 0.004	0.678 ± 0.005	0.606 ± 0.010	22 ± 2	15 ± 1	32 ± 8
2BT	8.6 ± 0.4	0.050 ± 0.004	0.70 ± 0.01	0.61 ± 0.02	6.0 ± 0.6	2.9 ± 0.5	52 ± 10
3B	33.3 ± 0.8	0.0023 ± 0.0006	0.678 ± 0.005	0.606 ± 0.010	1.1 ± 0.3	0.7 ± 0.2	42 ± 26
$Z \rightarrow \mu^+\mu^-$							
1BL	33.8 ± 0.8	0.346 ± 0.008	0.687 ± 0.005	0.70 ± 0.01	145 ± 5	106 ± 3	27 ± 3
1BT	1.4 ± 0.2	0.35 ± 0.01	0.75 ± 0.02	0.69 ± 0.01	5.8 ± 0.8	5.4 ± 0.7	6 ± 18
2BL	33.8 ± 0.8	0.055 ± 0.004	0.687 ± 0.005	0.70 ± 0.01	23 ± 2	15 ± 1	35 ± 7
2BT	8.6 ± 0.4	0.056 ± 0.004	0.74 ± 0.01	0.69 ± 0.02	5.6 ± 0.5	2.9 ± 0.5	49 ± 11
3B	33.8 ± 0.8	0.0027 ± 0.0006	0.687 ± 0.005	0.70 ± 0.01	1.1 ± 0.2	0.7 ± 0.2	41 ± 25

fits to the invariant mass distributions of the tag-and-probe pair with alternative signal and background shapes. An uncertainty of 10% (2%) is observed for the $Z \rightarrow e^+e^-$ ($Z \rightarrow \mu^+\mu^-$) selection. In addition, we repeat the efficiency measurement using a single-lepton-triggered data sample. This alternative measurement allows us to examine any potential dependence of the selection efficiency on the hadronic activity in the event. In the $Z \rightarrow e^+e^-$ case, we observe good agreement in the two measurements, while in the $Z \rightarrow \mu^+\mu^-$ case, a difference of 7% is seen. We assign a total systematic uncertainty on the selection efficiency of 10% (7%) for the $Z \rightarrow e^+e^-$ ($Z \rightarrow \mu^+\mu^-$) case.

We evaluate the uncertainty on the trigger efficiency $\varepsilon_{\text{trig}}$ by measuring the dependence of the efficiency on the choice of the offline H_T and E_T^{miss} cut applied. Based on the observed variation, we assign an uncertainty of 4%.

5.6.8 $Z \rightarrow \nu\nu$ prediction results

Table 5.13 summarizes the measured values of the $Z \rightarrow l^+l^-$ purity, acceptance, and the lepton efficiencies. The measured values of \mathcal{F} , together with the $Z \rightarrow \nu\nu$ background predictions in the data, are given in Table 5.14. We combine the predictions from the $Z \rightarrow \mu^+\mu^-$ and $Z \rightarrow e^+e^-$ samples with an error-weighted average. The final prediction is given in Table 5.15.

Table 5.12: Systematic uncertainties (in %) for the $Z \rightarrow \nu\bar{\nu}$ background prediction.

Selection	\mathcal{P}	$\varepsilon_{\text{trig}}$	$\varepsilon_{\text{sel}}^2$	Closure	\mathcal{F}	Total
$Z \rightarrow e^+e^-$						
1BL	10	4	20	37	11	45
1BT	10	4	20	50	52	76
2BL	10	4	20	48	83	98
2BT	10	4	20	62	77	101
3B	10	4	20	108	100	149
$Z \rightarrow \mu^+\mu^-$						
1BL	10	4	14	42	34	56
1BT	10	4	14	29	13	36
2BL	10	4	14	41	23	50
2BT	10	4	14	57	73	94
3B	10	4	14	61	100	118

Table 5.13: Purity, acceptance, and efficiencies used for the $Z \rightarrow \nu\nu$ background estimate. The errors shown are statistical only. As discussed in Sec. 5.6.2, the value of the acceptance depends on the choice of offline kinematic cuts. We show the measured values from MC for each selection.

Quantity	$Z \rightarrow e^+e^-$	$Z \rightarrow \mu^+\mu^-$
Purity (\mathcal{P})	0.95 ± 0.09	0.93 ± 0.09
Acceptance (\mathcal{A})		
1BL,2BL, and 3B	0.678 ± 0.005	0.687 ± 0.005
1BT	0.78 ± 0.02	0.75 ± 0.02
2BT	0.70 ± 0.01	0.74 ± 0.01
$\mathcal{E}_{\text{reco}}$	0.987 ± 0.014	0.985 ± 0.005
\mathcal{E}_{sel}	0.78 ± 0.03	0.81 ± 0.01
$\mathcal{E}_{\text{trig}}$	$1.00^{+0}_{-0.01}$	0.87 ± 0.04

Table 5.14: Results for the $Z \rightarrow \nu\bar{\nu}$ background prediction from the $Z \rightarrow e^+e^-$ and $Z \rightarrow \mu^+\mu^-$ control samples separately. Errors are statistical only.

Selection	$N_{\text{SIG-DL}}$	\mathcal{F}	\mathcal{A}	ε	$N_{\text{SIG}}^{Z \rightarrow \nu\bar{\nu}}$
$Z \rightarrow e^+e^-$					
1BL	30 ± 5	0.45 ± 0.06	0.678 ± 0.005	0.59 ± 0.08	191 ± 53
1BT	2 ± 1	0.42 ± 0.10	0.78 ± 0.02	0.59 ± 0.08	10 ± 8
2BL	30 ± 5	0.11 ± 0.04	0.678 ± 0.005	0.59 ± 0.08	46 ± 20
2BT	5 ± 2	0.11 ± 0.04	0.70 ± 0.01	0.59 ± 0.08	8 ± 5
3B	30 ± 5	0.006 ± 0.006	0.678 ± 0.005	0.59 ± 0.08	3 ± 2
$Z \rightarrow \mu^+\mu^-$					
1BL	28 ± 5	0.43 ± 0.05	0.687 ± 0.005	0.55 ± 0.05	175 ± 46
1BT	1 ± 1	0.38 ± 0.08	0.75 ± 0.02	0.55 ± 0.05	5 ± 5
2BL	28 ± 5	0.12 ± 0.04	0.687 ± 0.005	0.55 ± 0.05	47 ± 19
2BT	4 ± 2	0.12 ± 0.04	0.74 ± 0.01	0.55 ± 0.05	6 ± 4
3B	28 ± 5	0.006 ± 0.005	0.687 ± 0.005	0.55 ± 0.05	2 ± 2

Table 5.15: Combined prediction of the $Z \rightarrow \nu\nu$ background. Both statistical and systematic errors are included.

	$N_{\text{SIG}}^{Z \rightarrow \nu\bar{\nu}}$ (from $Z \rightarrow e^+e^-$)	$N_{\text{SIG}}^{Z \rightarrow \nu\bar{\nu}}$ (from $Z \rightarrow \mu^+\mu^-$)	$N_{\text{SIG}}^{Z \rightarrow \nu\bar{\nu}}$ (average)
1BL	191 ± 101	175 ± 109	184 ± 74
1BT	10 ± 11	5 ± 6	6 ± 5
2BL	46 ± 50	47 ± 30	47 ± 26
2BT	8 ± 9	6 ± 7	7 ± 6
3B	3 ± 5	2 ± 4	2 ± 3

5.7 Top and W +jets background

The production of $t\bar{t}$, single-top-quark, and W +jets events together form the dominant source of background in all search selections. We use a data-driven technique to estimate the collective contribution from these processes, which we refer to as the top + W background. We can classify top + W events that enter the search region based on the decay of the W boson. In the first category, exactly one W boson decays to either an $l + \nu$ pair ($l = e, \mu$), or to a $\tau + \nu$ pair, where the τ subsequently decays leptonically. The electron or muon in events of this category fails the requirement of the lepton veto selection, either because it is out of acceptance, poorly identified, or non-isolated. In the second category, exactly one W boson decays into a $\tau + \nu$ pair, where the τ subsequently decays hadronically. A third category of $t\bar{t}$ events, where both W bosons decay to an $l + \nu$ pair (or to a $\tau + \nu$ pair, where the τ subsequently decays leptonically), contributes a smaller amount to the total top + W background. As an illustration, we give the expected relative contribution of each category (for $t\bar{t}$ events only) in Table 5.16 for the 1BL selection.

Table 5.16: Relative contribution of the $t\bar{t}$ background categories, from MC, for the 1BL selection. In the decay mode of the W , l refers to e or μ , and τ_l (τ_h) refers to the leptonic (hadronic) decay of the τ .

Category	W decay modes	Fraction of total $t\bar{t}$ background
Semi- l	$W_1 \rightarrow qq'$ $W_2 \rightarrow l\nu$ or $W_2 \rightarrow \tau_l\nu$	45%
Semi- τ -hadronic	$W_1 \rightarrow qq'$ $W_2 \rightarrow \tau_h\nu$	47%
Dileptonic	$W_i \rightarrow l\nu$ or $W_i \rightarrow \tau_l\nu$	8%

We estimate the top + W background by using a control sample dominated by top + W events. Such a sample is obtained by applying the selection cuts in Sec. 5.3, but with an inverted lepton veto condition (i.e. we require exactly one electron or muon). We refer to this selection as the Single Lepton (SL) region. We then use the distribution of E_T^{miss} in this control sample as a template for the E_T^{miss} distribution of top + W events in our search region. The crucial assumption of the background estimation method is that the E_T^{miss} distribution of top + W events is the same between the two regions. The dominant source of E_T^{miss} in both regions is the neutrino from the W decay, and the distribution of E_T^{miss} is largely independent of whether the W decays to an $e, \mu, \text{ or } \tau$, and whether the τ decays leptonically or hadronically.

We normalize the E_T^{miss} distribution obtained from the SL region to the side-band (SB) region defined in Table 5.5. In particular, the predicted number of top+W events is given by:

$$N_{\text{SIG}}^{\text{top+W}} = N_{\text{SB}}^{\text{top+W}} \cdot \frac{N_{\text{SIG-SL}}^{\text{top+W}}}{N_{\text{SB-SL}}^{\text{top+W}}} = N_{\text{SB}}^{\text{top+W}} \cdot R^{\text{top+W}}, \quad (5.12)$$

where $N_{\text{SIG-SL}}^{\text{top+W}}$ and $N_{\text{SB-SL}}^{\text{top+W}}$ are the observed number of events in the corresponding E_T^{miss} region of the SL sample, and where we have defined $R^{\text{top+W}} \equiv \frac{N_{\text{SIG-SL}}^{\text{top+W}}}{N_{\text{SB-SL}}^{\text{top+W}}}$.

The number of top + W events in the SB region is obtained from the following relation:

$$N_{\text{SB}}^{\text{top+W}} = N_{\text{SB}} - N_{\text{SB}}^{\text{QCD}} - N_{\text{SB}}^{Z \rightarrow \nu\nu} - N_{\text{SB}}^{\text{other}}, \quad (5.13)$$

where N_{SB} is the observed number of events in the SB region. The terms $N_{\text{SB}}^{\text{QCD}}$, $N_{\text{SB}}^{Z \rightarrow \nu\nu}$, and $N_{\text{SB}}^{\text{other}}$ are included to take into account contamination in the SB region by other background processes. We derive values for $N_{\text{SB}}^{\text{QCD}}$ and $N_{\text{SB}}^{Z \rightarrow \nu\nu}$ using the methods described in Secs. 5.5 and 5.6, respectively. The term $N_{\text{SB}}^{\text{other}}$ consists of contributions from Drell-Yan and diboson production and is estimated using

the MC. A schematic diagram of the estimate procedure is shown in Fig. 5.17.

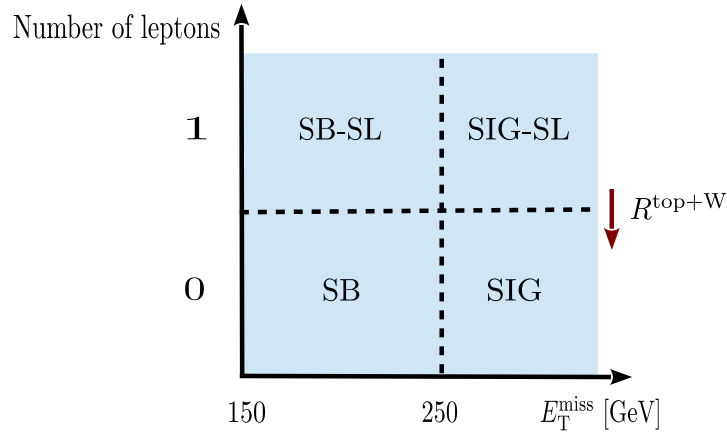


Figure 5.17: Schematic diagram of the top+W estimate procedure and the relevant regions. The lower E_T^{miss} boundary of the signal region in this diagram corresponds to the 1BL, 2BL, and 3B selections.

5.7.1 top + W control sample

As defined in the previous section, the SL sample is required to satisfy the nominal search selection, except with the replacement of the lepton veto with the requirement of one lepton. We impose an additional requirement on the transverse mass of the lepton and E_T^{miss} system, $m_T < 100$ GeV, to this control sample to reduce any possible contamination from SUSY signal events. Fig. 5.18 shows a comparison between the data and MC in the SL control sample. As expected, the sample is dominated by $t\bar{t}$ events and contains a small contribution from single-top-quark and W +jets events. The contribution from all other SM processes is negligible.

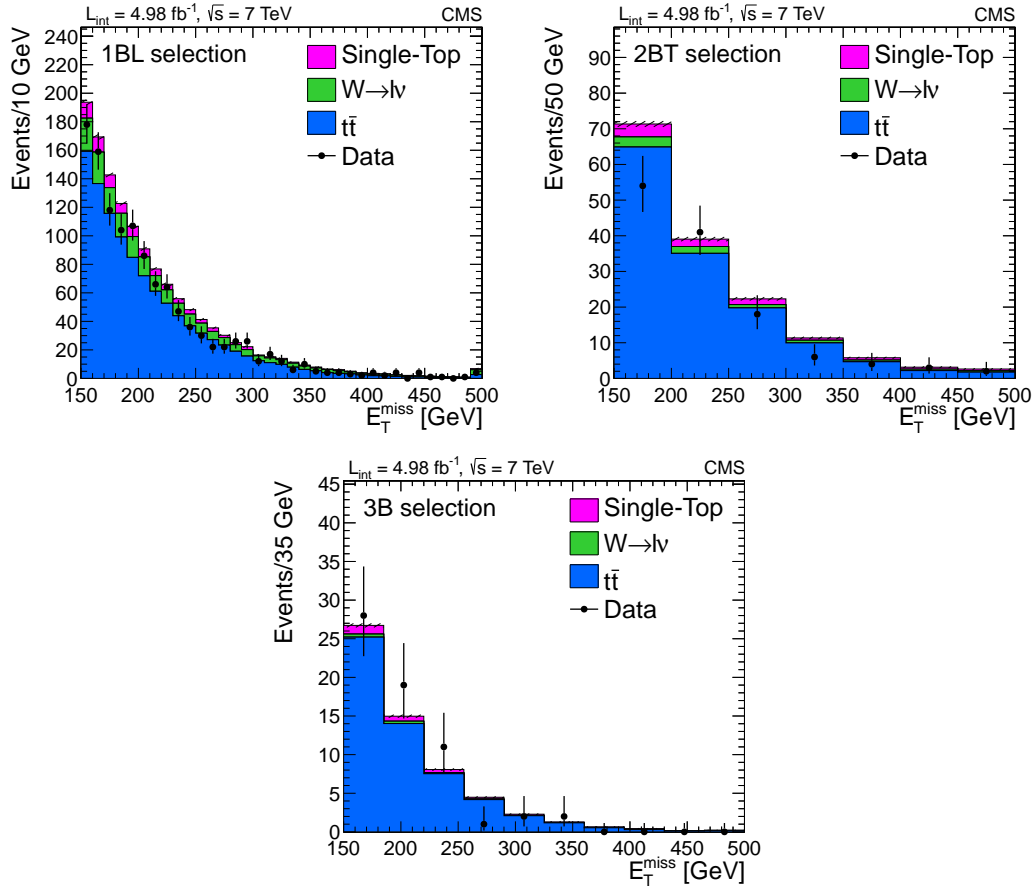


Figure 5.18: Comparison between the data and MC of the E_T^{miss} distribution in the SL control sample for the 1BL (top-left), 2BT (top-right), and 3B (bottom) selections. The hashed area gives the total statistical uncertainty on the MC.

5.7.2 Closure test of top + W prediction

Equation 5.12 relies on the assumption that the E_T^{miss} distributions of top + W events between the SL control sample and the search sample are consistent with each other. Fig. 5.19 shows the comparison in MC between the E_T^{miss} distributions in the SL region and the nominal regions. In general, we observe very good agreement in the shape of the distributions. To quantify the level of agreement, we compare in the top + W MC the true number of top + W events in the sig-

nal region with the prediction computed through Equation 5.12. The results are shown in Table 5.17. In general, we observe very good closure for the method.

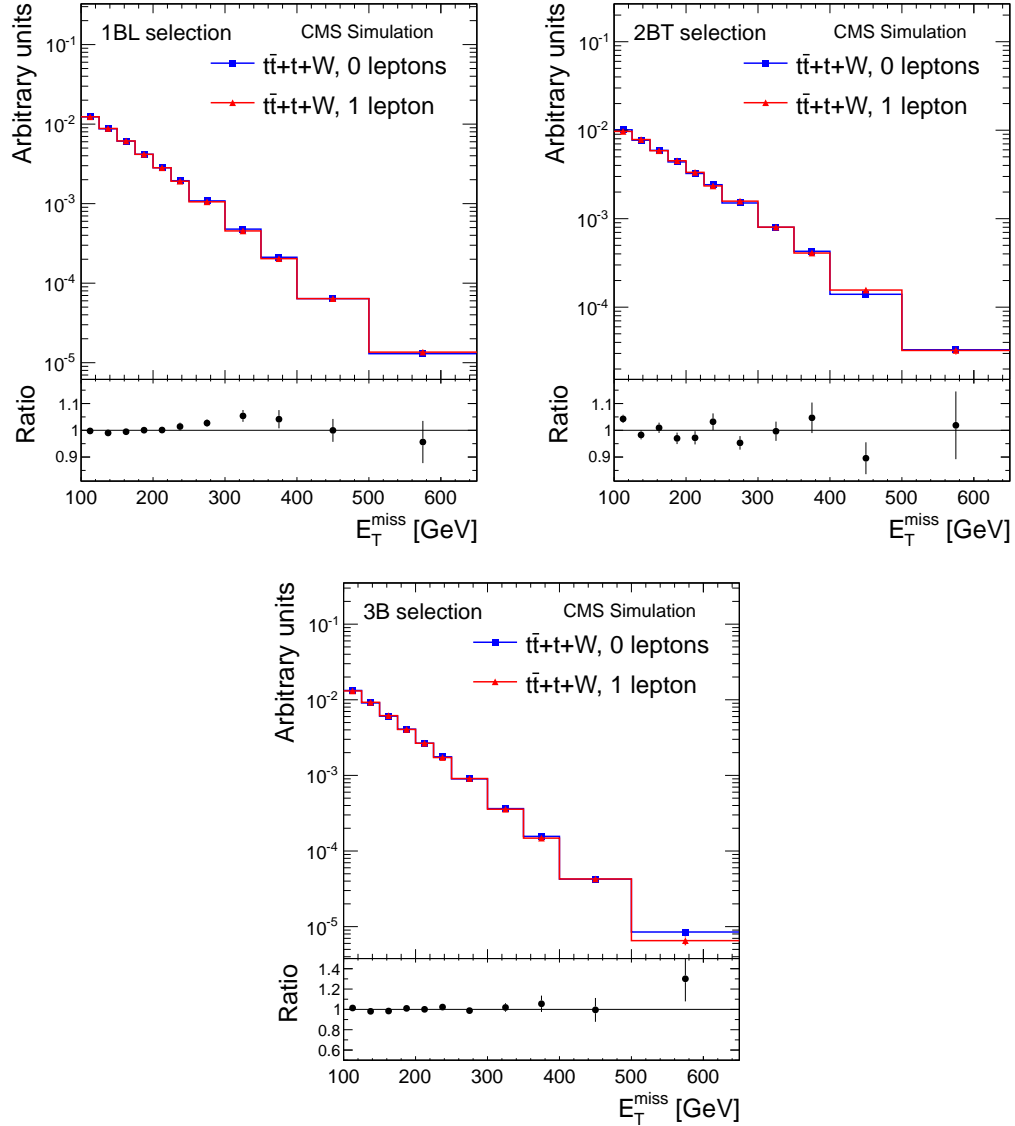


Figure 5.19: Comparison of the E_T^{miss} distribution for top + W events between the SL region (red) and the nominal region (blue) for the 1BL (top-left), 2BT (top-right), and 3B (bottom) selections. The plots below the main figures give the ratio of the blue and red distributions. We find very good agreement between the two regions.

Table 5.17: Closure test of the top + W prediction method in top + W MC, for each selection. Errors shown are statistical only. As in Secs. 5.5 and 5.6, we define the closure as the difference between the predicted and true yields, relative to the predicted yield. The closure is expressed in %

	$R^{\text{top+W}}$	$N_{\text{SB}}^{\text{top+W}}$	$N_{\text{SIG}}^{\text{top+W}}(\text{pred})$	$N_{\text{SIG}}^{\text{top+W}}(\text{true})$	Closure
1BL	0.249 ± 0.002	1434 ± 5	358 ± 3	370 ± 3	-3.2 ± 1.2
1BT	0.0104 ± 0.0007	761 ± 4	7.9 ± 0.5	7.3 ± 0.4	6.5 ± 7.8
2BL	0.217 ± 0.002	575 ± 2	125 ± 1	130 ± 1	-4.3 ± 1.5
2BT	0.201 ± 0.005	160 ± 1	32.4 ± 0.8	32.2 ± 0.6	0.4 ± 2.9
3B	0.207 ± 0.004	67.6 ± 0.4	14.1 ± 0.3	14.2 ± 0.2	-0.8 ± 2.3

5.7.3 Systematic uncertainties on top + W prediction

The dominant sources of systematic uncertainty in the prediction of the top + W background arise from the uncertainty in the QCD-background contribution to the SB region and on the uncertainty in the efficiency of the trigger. A summary of the systematic uncertainties on the top + W background prediction is given in Table 5.18.

The uncertainty due to the subtraction of QCD and $Z \rightarrow \nu\bar{\nu}$ contributions to the SB region is estimated by varying the data-driven QCD and $Z \rightarrow \nu\bar{\nu}$ predictions by their combined statistical and systematic uncertainties. We evaluate the uncertainty from the other non-(top + W) contributions by varying the MC estimate by $\pm 40\%$, which we obtain from evaluating the MC-related uncertainties listed in Sec. 5.8.2

The evaluation of the uncertainty on the trigger efficiency is described in App. A.3. We include the statistical uncertainty in the measured efficiency to

the total trigger uncertainty.

A systematic uncertainty on the level of closure of the method is evaluated as follows. The closure test described in the previous section is performed by combining the $t\bar{t}$, single-top-quark, and W +jets processes in the proportions given by their cross-sections listed in Table 5.1. To test the sensitivity of the method to the relative contribution of each process, we repeat the closure test after varying the cross-sections for the W +jets and single-top-quark processes by $\pm 50\%$ and $\pm 100\%$, respectively. The sizes of these variations are motivated by the uncertainty in the cross-sections for each process and by comparisons between the data and simulation. We assign as a systematic uncertainty the worst level of closure observed from all closure tests.

As a cross-check, we perform a second study to test the sensitivity of the method to changes in the E_T^{miss} distribution of the nominal sample arising from possible differences between the data and the MC. We separate the top + W events in the nominal sample into exclusive categories, based on the lepton flavor and on the cause of the lepton for failing the lepton veto condition. The causes include (a) the lepton falling out of kinematic acceptance (e.g. low- p_T and/or large- η leptons) and (b) the lepton failing the nominal quality/isolation criteria. Each category of events exhibits a E_T^{miss} distribution that can be significantly different from the E_T^{miss} distribution of the SL sample. We estimate an uncertainty on the expected yield from each category of events based on comparisons between the data and the MC. We then repeat the closure test after varying the contributions from each category by these uncertainties. We find that the level of closure in these extended tests is consistent with that of the nominal closure test, and therefore that the method is robust against modest

changes in the E_T^{miss} distribution arising from these variations.

Table 5.18: Systematic uncertainties on the top + W background prediction, expressed in %.

Selection	Closure	Trigger	SB contamination			Total
			QCD	$Z \rightarrow \nu\bar{\nu}$	Other	
1BL	4.6	13	13	7.7	0.8	20
1BT	15	14	19	7.7	0.7	29
2BL	5.5	11	8.6	7.4	0.3	17
2BT	4.6	11	21	11	0.2	26
3B	2.8	9.7	7.6	7.4	0.1	15

5.7.4 top + W prediction results

Before applying the estimation technique on the data, we consider the trigger efficiency in the various regions used in the method. As shown in Table 5.7, we measure a trigger efficiency that is different between the SL region and the search region, particularly in the E_T^{miss} range defined by the SB region. Moreover, Table 5.7 shows that the efficiencies in the SB-SL region depend on whether events have an electron or a muon. To account for these effects, we extend Eq. 5.12 to the following relation:

$$N_{\text{SIG}}^{\text{top+W}} = \varepsilon_{\text{SIG}} \cdot \frac{N_{\text{SIG-SL}}/\varepsilon_{\text{SIG-SL}}}{N_{\text{SB-SLe}}/\varepsilon_{\text{SB-SLe}} + N_{\text{SB-SL}\mu}/\varepsilon_{\text{SB-SL}\mu}} \cdot (N_{\text{SB}}/\varepsilon_{\text{SB}} - N_{\text{SB}}^{Z \rightarrow \nu\bar{\nu}} - N_{\text{SB}}^{\text{QCD}} - N_{\text{SB}}^{\text{other}}), \quad (5.14)$$

where SB-SLe (SB-SL μ) denotes the events in the SB-SL region that have one electron (one muon). In the above equation, the data-driven $Z \rightarrow \nu\bar{\nu}$ and QCD estimates are already corrected for the trigger efficiency, so that they reflect the

number of events that would have been observed with a fully efficient trigger. The prediction of the top + W background, using Equation 5.14, in the data is given in Table 5.19.

Table 5.19: Predicted top + W background yields for each search selection. $N_{\text{SIG}}^{\text{top+W}}$ is corrected for the trigger efficiency in the SIG region. Errors shown are statistical only.

Selection	$N_{\text{SIG-SL}}$	$N_{\text{SB-SL}}$	N_{SB}	$N_{\text{SB}}^{\text{non-(top+W)}}$	$N_{\text{SIG}}^{\text{top+W}}$
1BL	222	965	2087	990 ± 114	321 ± 37
1BT	4	468	1105	510 ± 63	6 ± 3
2BL	85	404	680	217 ± 43	117 ± 18
2BT	15	95	177	63 ± 16	22 ± 7
3B	7	56	79	16 ± 6	9 ± 4

5.8 Results and interpretation

In this section, we summarize the SM background predictions and compare the predictions with the number of events observed in the data. We then describe a global likelihood function that we use to simultaneously fit to the expected background and signal contributions. Since we do not observe a significant excess in the data over the expected SM background, we discuss briefly the statistical method used to test the hypothesis of a given signal model and interpret the results in terms of 95% confidence level (C.L.) upper limits on the signal cross sections for the $\tilde{g}\tilde{g} \rightarrow bbbb$, $\tilde{g}\tilde{g} \rightarrow tttt$, and $\tilde{t}\tilde{t} \rightarrow tt$ models.

5.8.1 Summary of background estimates

Table 5.20 summarizes the SM background predictions described in Secs. 5.5 to 5.7. In general, we find good agreement between the data and the sum of the SM background predictions. However, we observe a slight excess in the data for the 2BT and 3B selections. Assuming a normal distribution with a mean equal to the SM background prediction and a standard deviation equal to the total uncertainty on the prediction, we find that the probability of obtaining at least the observed number of events is 6.9% (3.6%) for the 2BT (3B) selection, corresponding to a one-sided z -score of 1.5 (1.8). Since these deviations are not significant, we proceed with setting 95% C.L. upper limit cross sections for the SUSY signal models of interest.

To compare the distribution of E_T^{miss} between the data and the SM background predictions in the various search selections, we split the signal region

Table 5.20: Summary of the SM background estimates and observed data yields. The first (second) error gives the statistical (systematic) uncertainty.

Sel.	QCD	$Z \rightarrow \nu\nu$	Top+W	Total SM	Data
1BL	$28 \pm 3 \pm 12$	$184 \pm 35 \pm 65$	$321 \pm 37 \pm 66$	$533 \pm 51 \pm 94$	478
1BT	$0.0 \pm 0.2 \pm 0.3$	$6.2 \pm 4.0 \pm 2.0$	$6.4 \pm 3.3 \pm 1.9$	$13 \pm 5 \pm 3$	11
2BL	$4.7 \pm 1.3 \pm 2.8$	$47 \pm 14 \pm 21$	$117 \pm 17.6 \pm 19$	$169 \pm 22 \pm 29$	146
2BT	$0.8 \pm 0.4 \pm 1.2$	$6.8 \pm 3.0 \pm 4.7$	$22 \pm 7 \pm 6$	$29 \pm 8 \pm 8$	45
3B	$1.0 \pm 0.5 \pm 0.5$	$2.5 \pm 1.7 \pm 2.3$	$9.2 \pm 3.9 \pm 1.4$	$13 \pm 4 \pm 3$	22

for each selection into several bins of E_T^{miss} and derive the background prediction for each bin separately. Fig 5.20 shows the resulting comparison. We find good agreement in the shape of the E_T^{miss} distribution.

5.8.2 Signal efficiency

To compute a 95% C.L. upper limit on the cross section of a b -enriched SUSY model, we first measure with the MC the selection efficiency at each mass point ($m_{\tilde{g}}, m_{\text{LSP}}$) (or ($m_{\tilde{t}}, m_{\text{LSP}}$)) in the model spectrum. We refer to this quantity as the signal efficiency. The signal efficiency is shown in Fig. 5.21, 5.22, and 5.23 for each mass point in the $\tilde{g}\tilde{g} \rightarrow bbbb$, $\tilde{g}\tilde{g} \rightarrow tttt$, and $\tilde{t}\tilde{t} \rightarrow tt$ models, respectively. The signal efficiency of the $\tilde{g}\tilde{g} \rightarrow bbbb$ model in the 3B selection can be as high as 25% in the region with large values of $\Delta m = m_{\tilde{g}} - m_{\text{LSP}}$, which give, on average, events with larger values of H_T and E_T^{miss} .

At mass points in the $\tilde{g}\tilde{g} \rightarrow bbbb$ and $\tilde{t}\tilde{t} \rightarrow tt$ models with small values of Δm , we expect the majority of events to fail the H_T requirement of the selection, since

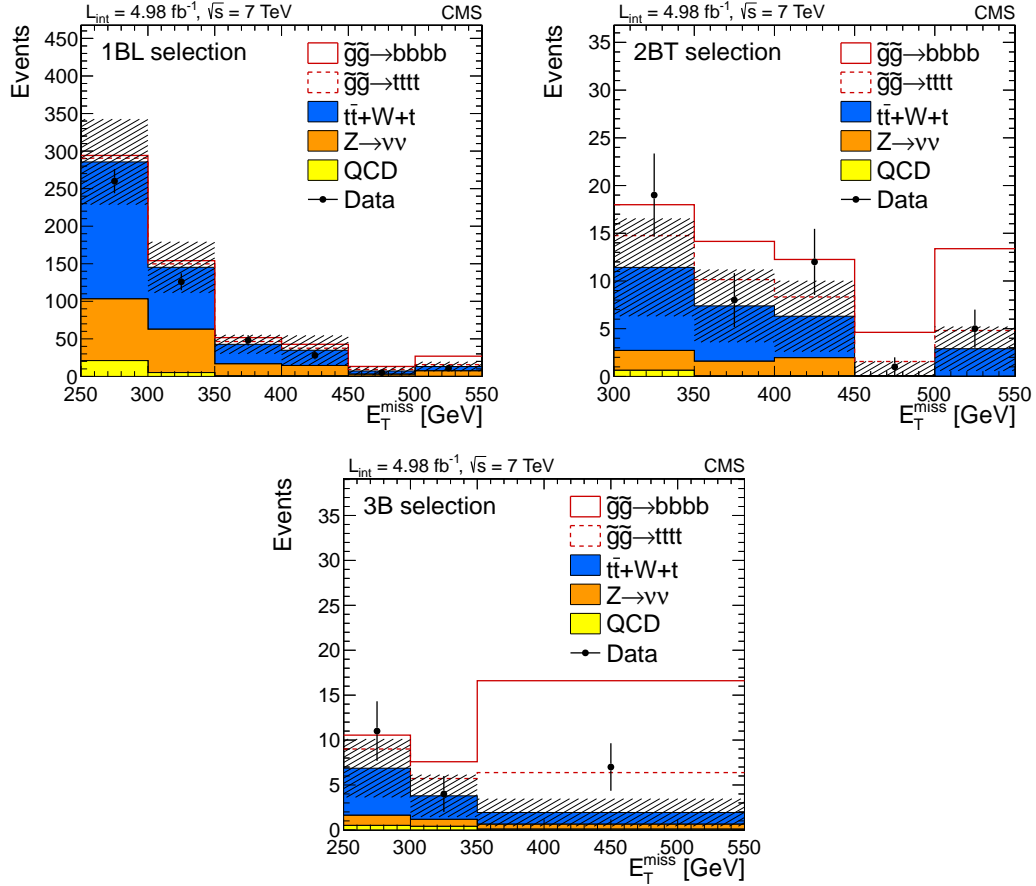


Figure 5.20: Comparison of the E_T^{miss} distribution between the data and the SM background predictions for the 1BL (top-left), 2BT (top-right), and 3B (bottom) selections. The background predictions are estimated in each bin of E_T^{miss} . The hashed area gives the total uncertainty on the predictions, which is correlated between bins. The open histograms give the expected yield from the $\tilde{g}\tilde{g} \rightarrow bbbb$ and $\tilde{g}\tilde{g} \rightarrow tttt$ models with $m_{\tilde{g}} = 925 \text{ GeV}$ and $m_{\text{LSP}} = 100 \text{ GeV}$, normalized to the reference cross section.

most of the energy of the gluino/top-squark will have gone into producing the LSP. Thus, an event that does survive the H_T requirement will likely have a large component of its visible energy arising from initial-state radiation (ISR). Since uncertainties on the simulation of ISR in PYTHIA are not evaluated, we apply the following procedure to exclude from consideration mass points whose signal efficiencies are overly sensitive to ISR. For each mass point, we re-evaluate

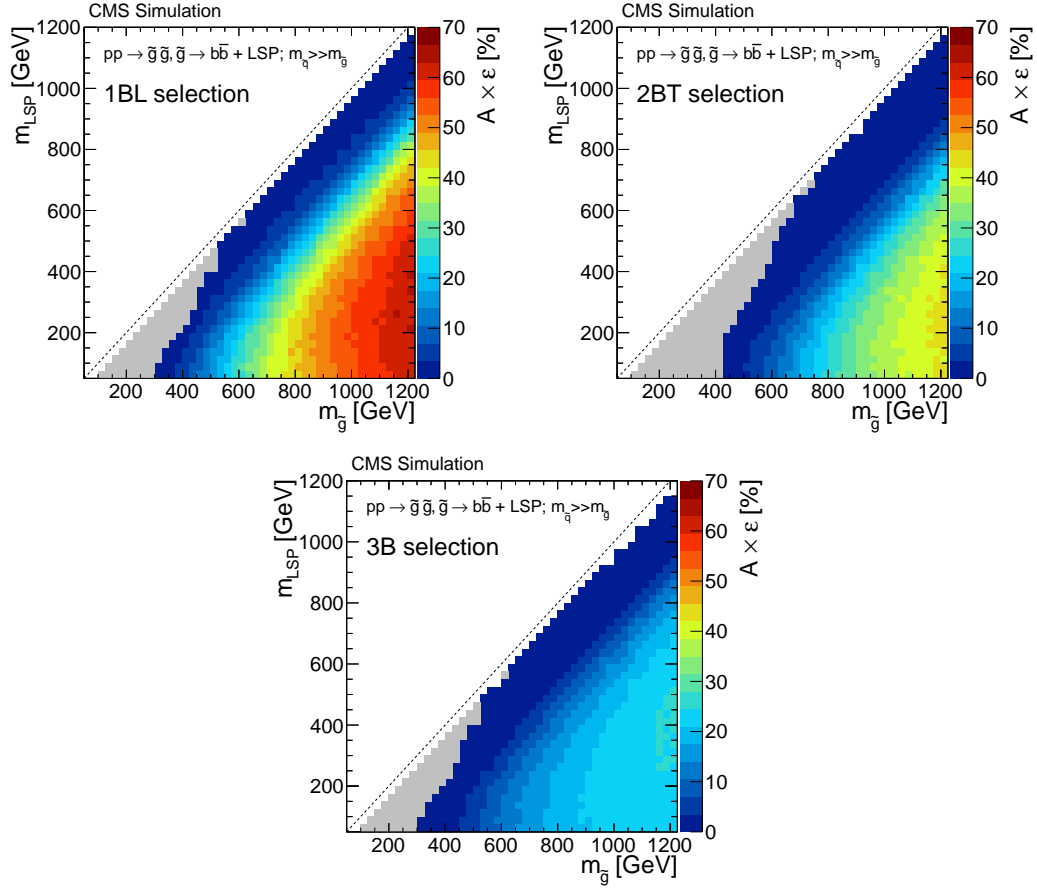


Figure 5.21: Signal efficiency (in %) for the $\tilde{g}\tilde{g} \rightarrow bbbb$ model in the 1BL (top-left), 2BT (top-right), and 3B (bottom) selections. The gray cells indicate mass points that are not considered due to their sensitivity to ISR.

the signal efficiency using a corresponding signal sample with ISR effectively removed from the event generation. If the difference in signal efficiency relative to that of the ordinary signal sample is larger than 50%, we remove the mass point from consideration. Points which are removed by this procedure are shown in gray in Fig. 5.21 to 5.23.

We evaluate the following systematic uncertainties on the signal efficiency:

- The uncertainty due to the energy scale of jets is evaluated by varying the

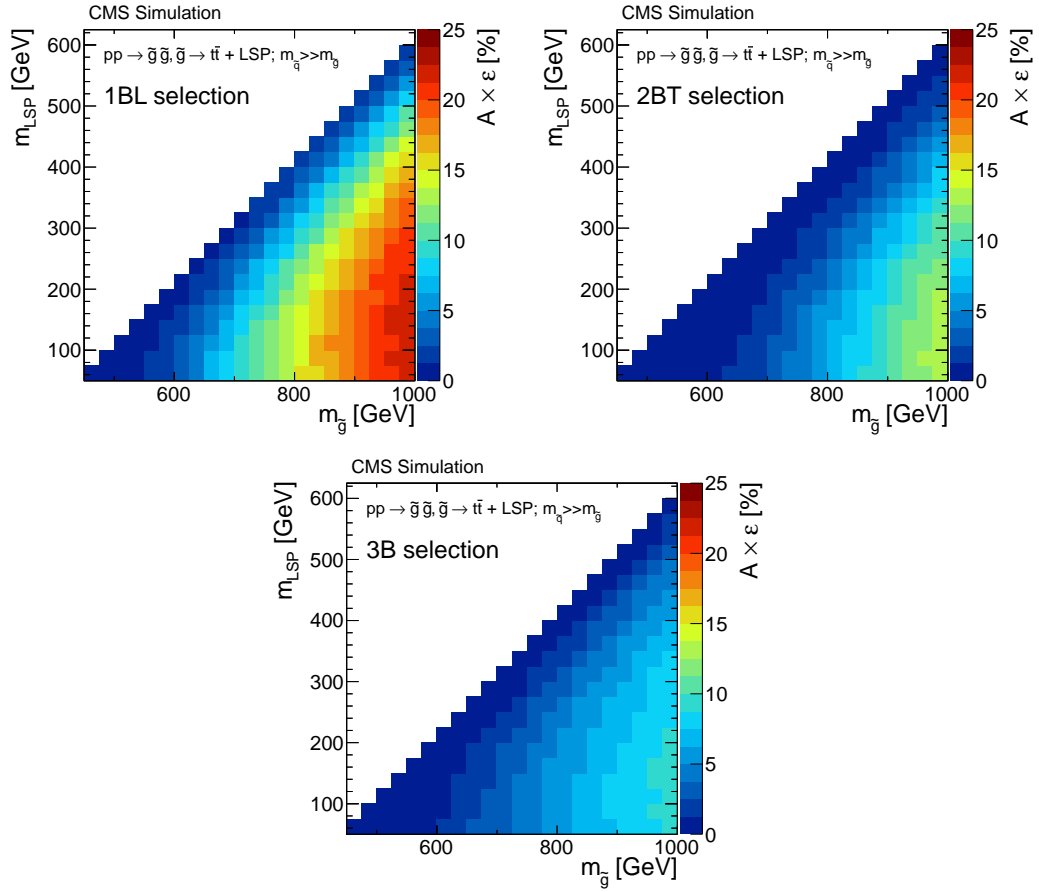


Figure 5.22: Signal efficiency (in %) for the $\tilde{g}\tilde{g} \rightarrow ttt$ model in the 1BL (top-left), 2BT (top-right), and 3B (bottom) selections.

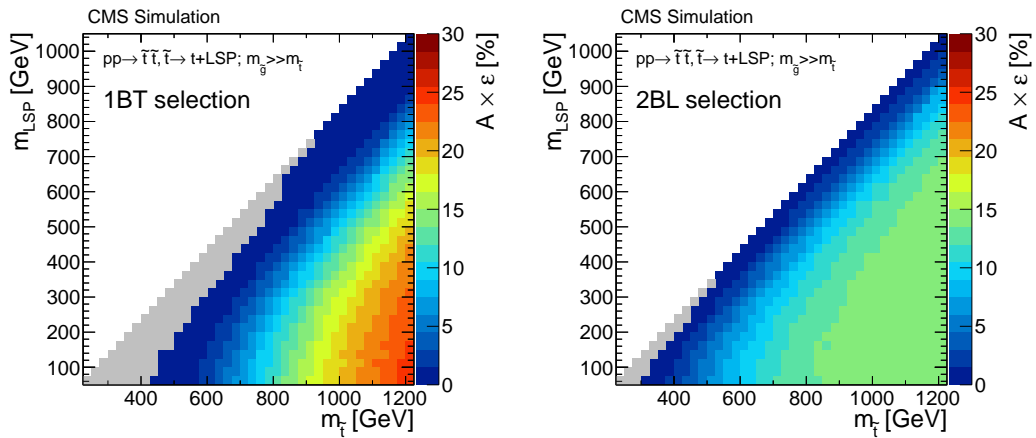


Figure 5.23: Signal efficiency (in %) for the $\tilde{t}\tilde{t} \rightarrow tt$ model in the 1BT (left) and 2BL (right) selections. The gray cells indicate mass points that are not considered due to their sensitivity to ISR.

p_T of all jets by their uncertainty prior to computing the efficiency. The E_T^{miss} in the event is also corrected for any changes in the p_T of the jets.

- The uncertainty due to the jet energy resolution of the MC (Appendix B) is estimated by varying the resolution by the uncertainties given in Reference [48].
- The uncertainty on the E_T^{miss} scale due to the contribution from unclustered energy (energy deposits not associated with any leptons or jets) is assessed by varying the size of this component by 10%.
- We estimate the uncertainty from the efficiency to identify true b jets and to mis-identify non- b jets as b jets by propagating their uncertainties with the procedure described in Appendix B. The uncertainties are a combination of the differences in the efficiencies between the data and MC (given in Reference [34]) and the differences in the efficiencies between the full simulation and the Fast Simulation (Sec. 5.2).
- The uncertainty due to the parton distribution function (PDF) is evaluated by varying each of the parameters used in the global fit of the PDF by their uncertainties, as outlined in References [49] and [50]. We assign as the systematic uncertainty the maximum observed variation in the signal efficiency from each of the CTEQ6.6 [36], MSTW2008 [51], and NNPDF2.0 [52] PDF sets.
- The uncertainty on the simulation of pile-up interactions in the MC is assessed by varying the total inelastic cross section by its uncertainty (8%).
- We assign a 3.5% uncertainty due to the statistical uncertainty in the measurement of the trigger efficiency.
- An uncertainty of 1% is assigned to the efficiency of the anomalous E_T^{miss} filters based on the full inefficiency of the filters as evaluated from the MC.

- We apply a 3% uncertainty on the efficiency of the lepton veto selection based on studies done in a $Z \rightarrow l^+l^-$ sample.
- The uncertainty on the value of the integrated luminosity is 2.2% [53].

Table 5.21 summarizes the contributions to the total systematic uncertainty for a representative $\tilde{g}\tilde{g} \rightarrow bbbb$ model with parameters $m_{\tilde{g}} = 925$ GeV and $m_{\text{LSP}} = 100$ GeV. We attribute the relatively large uncertainty in the jet energy scale for the 1BT and 2BT selections to the relatively low MC statistics available in those regions. The uncertainty due to the b jet tagging efficiency increases with the increasing requirement on the number of b jets. This is attributed to the probability of identifying an event as having a given number of b jets, as described in Appendix B. Overall, we find similar uncertainties for mass points in the $\tilde{g}\tilde{g} \rightarrow tttt$ model.

In Fig 5.24, 5.25, and 5.26, we show the total signal efficiency uncertainty per mass point in the $\tilde{g}\tilde{g} \rightarrow bbbb$, $\tilde{g}\tilde{g} \rightarrow tttt$, and $\tilde{t}\tilde{t} \rightarrow tt$ models, respectively. We evaluate the systematic uncertainties due to the jet energy scale, unclustered energy, b jet efficiency, and PDF uncertainties separately for each mass point in the models. For the remaining sources of uncertainty, we use the representative values of Table 5.21. In general, the relative systematic uncertainty increases with decreasing Δm (i.e. as the peak of the H_T and E_T^{miss} distributions for the model nears the H_T and E_T^{miss} threshold requirement of the selection).

Table 5.21: Summary of the systematic uncertainties (in %) on the signal efficiency for the $\tilde{g}\tilde{g} \rightarrow bbbb$ model with $m_{\tilde{g}} = 925 \text{ GeV}$ and $m_{\text{LSP}} = 100 \text{ GeV}$.

	1BL	1BT	2BL	2BT	3B
Jet energy scale	2.1	11	1.9	3.5	1.7
Jet energy resolution	1.0	1.0	1.0	1.0	1.0
Unclustered energy	0.2	0.8	0.2	0.3	0.2
b jet tagging efficiency	1.0	1.1	4.4	4.5	10
Parton distribution functions	0.4	1.6	0.4	0.7	0.6
Pile-up	1.0	1.0	1.0	1.0	1.0
Trigger efficiency	3.6	3.6	3.6	3.6	3.6
Anomalous $E_{\text{T}}^{\text{miss}}$	1.0	1.0	1.0	1.0	1.0
Lepton veto	3.0	3.0	3.0	3.0	3.0
Luminosity	2.2	2.2	2.2	2.2	2.2
Total systematic uncertainty	6.0	13	7.3	7.9	12

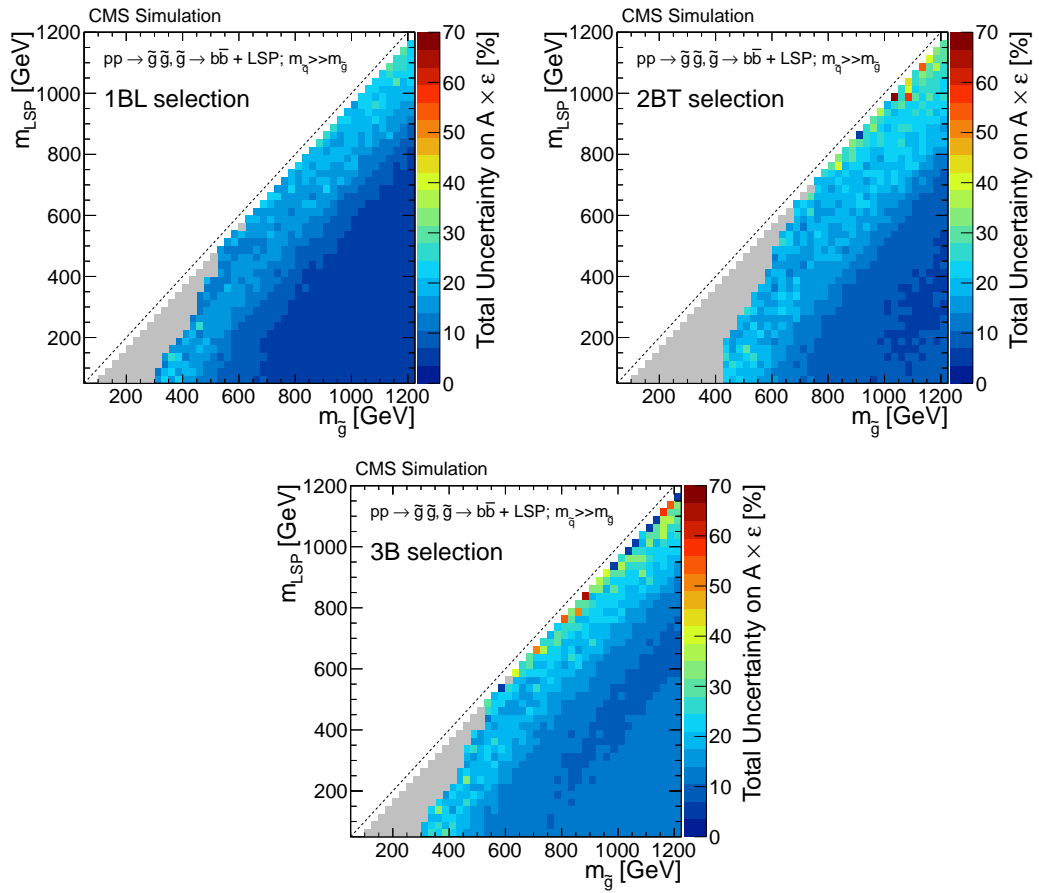


Figure 5.24: Relative systematic uncertainty (in %) on the signal efficiency in the 1BL (top-left), 2BT (top-right), and 3B (bottom) selections for the $\tilde{g}\tilde{g} \rightarrow bbbb$ model. The gray cells indicate mass points that are not considered due to their sensitivity to ISR.

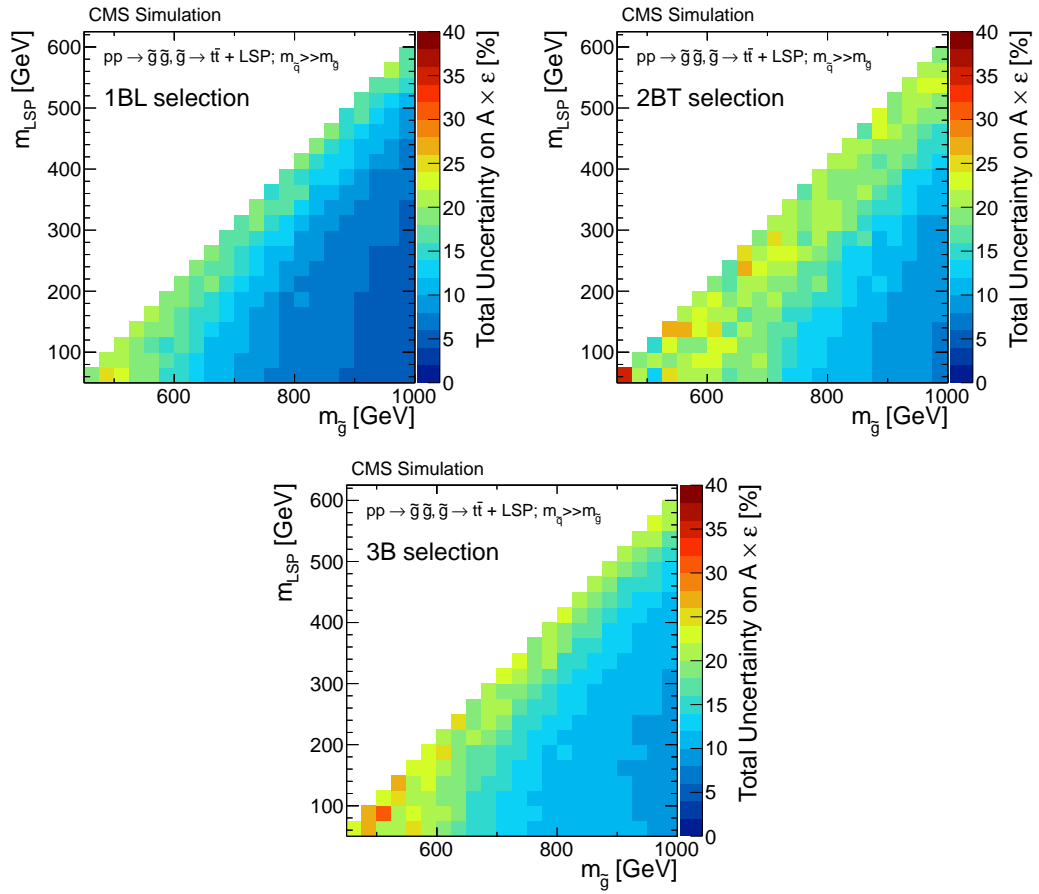


Figure 5.25: Relative systematic uncertainty (in %) on the signal efficiency in the 1BL (top-left), 2BT (top-right), and 3B (bottom) selections for the $\tilde{g}\tilde{g} \rightarrow t\bar{t}t$ model.

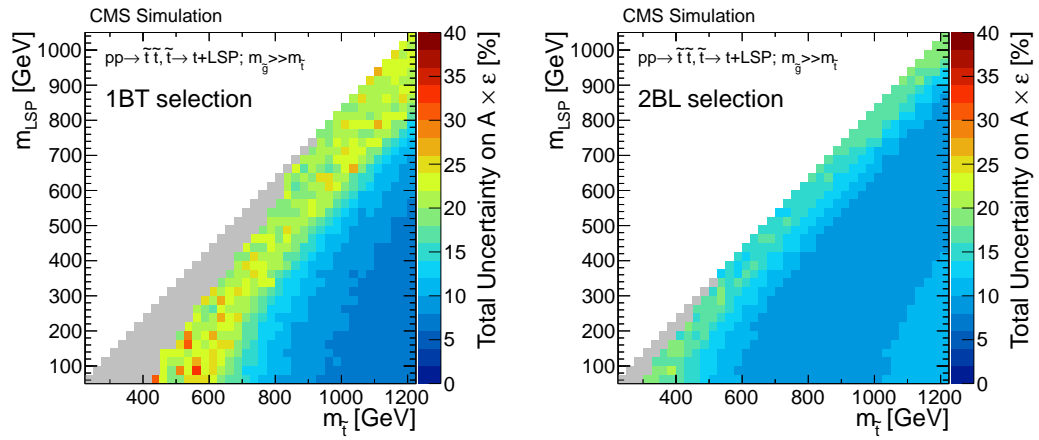


Figure 5.26: Relative systematic uncertainty (in %) on the signal efficiency in the 1BT (left) and 2BL (right) selections for the $\tilde{t}\tilde{t} \rightarrow tt$ model. The gray cells indicate mass points that are not considered due to their sensitivity to ISR.

5.8.3 Global likelihood

We combine the background methods described in the previous sections into a global likelihood function. This allows us to account for correlations among the different background predictions and for the contribution of potential SUSY signal events to the various control samples in a coherent fashion. The size of the signal contribution can be non-negligible in the SB, LDP, and SL control regions.

The observables in the likelihood are the number of events in the signal and control regions listed in Table 5.5. To properly account for differences in the trigger efficiencies (Sec. 5.4), we separate the SB-SL region into the single-electron (SB-SL e) and single-muon (SB-SL μ) components. Similarly, the SIG-DL and SB-DL regions are separated into the $Z \rightarrow e^+e^-$ (SIG-DL e) and $Z \rightarrow \mu^+\mu^-$ (SIG-DL μ) components. This gives a total of 11 mutually exclusive observables, which we denote by N_i ($i = 1, \dots, 11$). We occasionally refer to these 11 observables as “bins” in the likelihood. For each observable N_i , we define n_i as the parameter corresponding to the expected number of events. We constrain these parameters with a Poisson distribution $\mathcal{P}(N_i|n_i)$ with mean n_i . Each parameter n_i can be expressed as a sum of the expected number of events from SM background (μ_i^X , where $X = \text{QCD}, Z \rightarrow \nu\nu$, or top + W) and from the SUSY signal (μ_i^{SUSY}). The relations are given in Table 5.22, where we also introduce several auxiliary parameters. The parameter ε_i denotes the trigger efficiency in region i , while the parameters \mathcal{P}_i denote the measured $Z \rightarrow l^+l^-$ purities in the DL control regions. Each of the parameters ε_i and \mathcal{P}_i is constrained by a β -distribution [54], with a mode set to its measured value and a variance set to the squared uncertainty on the measured value. The parameters C_i^X account for the systematic uncertainty on the contribution from process X in region i , and are each constrained by a

Table 5.22: Expected number of events n_i for each of the 11 observables, expressed in terms of the expected yield μ_i^X from each process X . The parameter ε_i is the trigger efficiency in region i . The parameters C_i^X are included to account for the systematic uncertainty on the yield for process X in region i . The factor \mathcal{P}_l ($l = e, \mu$) denotes the $Z \rightarrow l^+l^-$ purity of the sample.

Parameter	Relation
n_{SIG}	$\varepsilon_{\text{SIG}} \cdot \left(\mu_{\text{SIG}}^{\text{top+W}} + \mu_{\text{SIG}}^{\text{QCD}} + \mu_{\text{SIG}}^{Z \rightarrow \nu\nu} + C_{\text{SIG}}^{\text{SUSY}} \cdot \mu_{\text{SIG}}^{\text{SUSY}} \right)$
n_{SB}	$\varepsilon_{\text{SB}} \cdot \left(\mu_{\text{SB}}^{\text{top+W}} + \mu_{\text{SB}}^{\text{QCD}} + \mu_{\text{SB}}^{Z \rightarrow \nu\nu} + C_{\text{SB}}^{\text{SUSY}} \cdot \mu_{\text{SB}}^{\text{SUSY}} \right)$
$n_{\text{SIG-LDP}}$	$\varepsilon_{\text{SIG-LDP}} \cdot \left(\mu_{\text{SIG-LDP}}^{\text{QCD}} + C_{\text{SIG-LDP}}^{\text{top+EW}} \cdot \mu_{\text{SIG-LDP}}^{\text{top+EW}} + C_{\text{SIG-LDP}}^{\text{SUSY}} \cdot \mu_{\text{SIG-LDP}}^{\text{SUSY}} \right)$
$n_{\text{SB-LDP}}$	$\varepsilon_{\text{SB-LDP}} \cdot \left(\mu_{\text{SB-LDP}}^{\text{QCD}} + C_{\text{SB-LDP}}^{\text{top+EW}} \cdot \mu_{\text{SB-LDP}}^{\text{top+EW}} + C_{\text{SB-LDP}}^{\text{SUSY}} \cdot \mu_{\text{SB-LDP}}^{\text{SUSY}} \right)$
$n_{\text{SIG-SL}}$	$\varepsilon_{\text{SIG-SL}} \cdot \left(\mu_{\text{SIG-SL}}^{\text{top+W}} + C_{\text{SIG-SL}}^{\text{SUSY}} \cdot \mu_{\text{SIG-SL}}^{\text{SUSY}} \right)$
$n_{\text{SB-SL}e}$	$\varepsilon_{\text{SB-SL}e} \cdot \left(\mu_{\text{SB-SL}e}^{\text{top+W}} + C_{\text{SB-SL}e}^{\text{SUSY}} \cdot \mu_{\text{SB-SL}e}^{\text{SUSY}} \right)$
$n_{\text{SB-SL}\mu}$	$\varepsilon_{\text{SB-SL}\mu} \cdot \left(\mu_{\text{SB-SL}\mu}^{\text{top+W}} + C_{\text{SB-SL}\mu}^{\text{SUSY}} \cdot \mu_{\text{SB-SL}\mu}^{\text{SUSY}} \right)$
$n_{\text{SIG-DL}e}$	$\mu_{\text{SIG-DL}e}^{Z \rightarrow e^+e^-} / \mathcal{P}_e$
$n_{\text{SB-DL}e}$	$\mu_{\text{SB-DL}e}^{Z \rightarrow e^+e^-} / \mathcal{P}_e$
$n_{\text{SIG-DL}\mu}$	$\mu_{\text{SIG-DL}\mu}^{Z \rightarrow \mu^+\mu^-} / \mathcal{P}_\mu$
$n_{\text{SB-DL}\mu}$	$\mu_{\text{SB-DL}\mu}^{Z \rightarrow \mu^+\mu^-} / \mathcal{P}_\mu$

β' -distribution [54] with a mode of 1 and a variance set to the square of the systematic uncertainty. We use β and β' distributions to constrain these parameters as they have the desirable vanishing boundary condition at 0 (and at 1, for the case of the β distribution). The systematic uncertainties on the other parameters in Table 5.22 are incorporated in the relations described below and are also constrained by β' distributions.

As shown in Table 5.22, we allow for the the presence of a non-zero SUSY signal in all bins except the $Z \rightarrow l^+l^-$ control regions. For a given SUSY model, we fix the relative proportions of the parameters μ_i^{SUSY} in each bin using the MC.

To incorporate the background prediction methods described in Secs. 5.5 to 5.7, we define the following relations. First, the parameters determining the contributions from the QCD background are constrained by the relation of Eq. 5.7:

$$\mu_{\text{SIG}}^{\text{QCD}} = \mu_{\text{SIG-LDP}}^{\text{QCD}} \cdot R^{\text{QCD}} \cdot C^{\text{QCD}}. \quad (5.15)$$

In this case, R^{QCD} is a parameter constrained by a β' distribution whose mode and width are set by the measured central value and statistical uncertainty reported in Table 5.9. The additional parameter C^{QCD} accounts for all systematic uncertainties on the QCD prediction not related to the non-QCD subtraction in the LDP regions, which is already accounted for by $C_{\text{SIG-LDP}}^{\text{top+EW}}$ above. An analogous relation is defined for the SB region. Second, the parameters determining the contribution from the $Z \rightarrow \nu\nu$ background are constrained by the relation in Eq. 5.11:

$$\mu_{\text{SIG}}^{Z \rightarrow \nu\nu} = \mu_{\text{SIG-DLl}} \cdot \frac{\mathcal{R} \cdot \mathcal{F}_{ll}}{\mathcal{A}_{ll} \cdot \varepsilon_{ll}} \cdot C_{ll}^{Z \rightarrow \nu\nu}, \quad (5.16)$$

where $l = e, \mu$ (and similarly for the SB region). As in the case of the QCD relation above, the parameters \mathcal{F}_{ll} , \mathcal{A}_{ll} , and ε_{ll} are constrained by their measured values and statistical uncertainties as reported in Table 5.14. The parameter $C_{ll}^{Z \rightarrow \nu\nu}$ accounts for the systematic uncertainty on the $Z \rightarrow \nu\bar{\nu}$ background prediction. Finally, the parameters defining the contributions from the top + W background are constrained by the same relation as in Eq. 5.12, namely:

$$\mu_{\text{SIG}}^{\text{top+W}} = \mu_{\text{SB}}^{\text{top+W}} \cdot \frac{\mu_{\text{SIG-SL}}^{\text{top+W}}}{\mu_{\text{SB-SLe}}^{\text{top+W}} + \mu_{\text{SB-SL}e}^{\text{top+W}}} \cdot C^{\text{top+W}}, \quad (5.17)$$

where the parameter $C^{\text{top+W}}$ accounts for the systematic uncertainty due to the closure of the top + W background method.

We define the full likelihood function as

$$\mathcal{L} = \mathcal{P}_{\text{QCD}} \cdot \mathcal{P}_{Z \rightarrow \nu\nu} \cdot \prod_Y \beta'(C^Y) \cdot \prod_{i=1}^{11} \mathcal{P}(N_i | n_i) \cdot \beta(\varepsilon_i), \quad (5.18)$$

where the first product runs over all systematic uncertainty parameters C^Y defined above, and where we make the short-hand notation:

$$\mathcal{P}_{\text{QCD}} = \beta'(R^{\text{QCD}}), \quad \mathcal{P}_{Z \rightarrow \nu\nu} = \prod_{l=e,\mu} \beta'(\mathcal{F}_{ll}) \cdot \beta(\mathcal{A}_{ll}) \cdot \beta(\varepsilon_{ll}) \cdot \beta(\mathcal{P}_{ll}). \quad (5.19)$$

5.8.4 Hypothesis testing

We perform a hypothesis test of a given SUSY model using the test statistic of the generic form

$$t_{\mu_0} = -2 \ln \left(\frac{\mathcal{L}_{\max}(\mu_{\text{SIG}}^{\text{SUSY}} = \mu_0)}{\mathcal{L}_{\max}} \right), \quad (5.20)$$

where \mathcal{L}_{\max} is the likelihood \mathcal{L} obtained after maximizing over all parameters described in the previous section (given the observed counts N_i), and $\mathcal{L}_{\max}(\mu_{\text{SIG}}^{\text{SUSY}} = \mu_0)$ is the corresponding maximum obtained from varying all parameters except $\mu_{\text{SIG}}^{\text{SUSY}}$, which is fixed to the value μ_0 set by the signal hypothesis. The ratio of the likelihoods is bounded (by construction) between 0 and 1. Thus, the range of the test statistic is $0 \leq t_{\mu_0} < \infty$. The general characteristic of the test statistic is that the more likely the hypothesis of a signal with yield μ_0 given the observed yields, the closer the ratio of likelihoods in the above expression is to 1, and the smaller the value of t_{μ_0} .

We denote the hypothesis of a SUSY signal existing in addition to the SM background as the ‘‘S+B’’ hypothesis, and the alternative hypothesis (that there is no SUSY signal) as the ‘‘B-only’’ hypothesis. For a given SUSY signal, $\mu_{\text{SIG}}^{\text{SUSY}} = \mu_0$, we define $\text{CL}_{s+b} = P(t_{\mu_0} \geq t_{\mu_0, \text{obs}} | \text{S+B})$ as the probability of obtaining a value of the test statistic at least as large as the observed value under the S+B hypothesis, and $\text{CL}_b = P(t_{\mu_0} \geq t_{\mu_0, \text{obs}} | \text{B-only})$ as the corresponding quantity under the B-only hypothesis. We then use the ratio $\text{CL}_s = \text{CL}_{s+b} / \text{CL}_b$ as a measure of the

compatibility of the SUSY signal hypothesis with the observed data [55]. We reject the hypothesis of a SUSY signal at the 95% confidence level if $CL_s < 0.05$.

In order to compute the above probabilities, we need to know the probability density functions $f(t_{\mu_0} | \mu = \mu_0)$ and $f(t_{\mu_0} | \mu = 0)$, which correspond to the probability density functions of t_{μ_0} under the S+B and B-only hypotheses, respectively. One method of obtaining these distributions is to generate two ensembles of pseudo-experiments. One ensemble is generated by sampling the likelihood $\mathcal{L}_{max}(\mu_{SIG}^{SUSY} = \mu_0)$, while the other is generated using the likelihood $\mathcal{L}_{max}(\mu_{SIG}^{SUSY} = 0)$. We then compute the value of t_{μ_0} for each pseudo-experiment, thus obtaining the distribution of $f(t_{\mu_0} | \mu = \mu_0)$ from one ensemble, and the distribution of $f(t_{\mu_0} | \mu = 0)$ from the other. However, since the above procedure requires generating a large number of pseudo-experiments, which is computationally prohibitive, we employ an alternative method for obtaining the probability density functions. We assume approximate analytic expressions for $f(t_{\mu_0} | \mu = \mu_0)$ and $f(t_{\mu_0} | \mu = 0)$, following the derivation in Reference [56]. For example, by the result of Wilks [57], $f(t_{\mu_0} | \mu = \mu_0)$ is approximately a χ^2 distribution with one degree of freedom. To validate this alternative method, we compare for a subset of mass points the 95% C.L. upper limit obtained with this method with the corresponding value obtained by generating ensembles of pseudo-experiments. In most cases, the results agree to within a few percent. In the cases where the differences are non-negligible ($> 10\%$), we apply a uniform scale-factor to the results obtained with the alternative method for each search selection across all mass points of a given signal model. The value of the scale-factor ranges from 1 to 1.25.

At each SUSY mass point, we compute the values of CL_s over a range of

μ_0 values. We then interpolate between the computed CL_s values to obtain the value of μ_0 at which $CL_s < 0.05$. The corresponding upper limit on the cross-section is obtained by using the value of the signal efficiency at the given mass point, as determined in Sec. 5.8.2.

5.8.5 Likelihood results

For each SUSY model, we calculate at each mass point and for each search selection the 95% C.L. upper limit on the cross section under the assumption that the observed yield N_{SIG} is exactly equal to the SM background prediction given in Table 5.20. We refer to this value as the expected upper limit. The selection that gives the lowest expected upper limit is shown in Fig. 5.27. For the $\tilde{g}\tilde{g} \rightarrow bbbb$ model, the 3B selection provides the best sensitivity in the bulk of the $m_{\tilde{g}}$ vs. m_{LSP} parameter space, except at very high values of Δm , where the 1BT selection is most sensitive. For the $\tilde{g}\tilde{g} \rightarrow tttt$ model, we find that the 3B selection gives the best sensitivity across the entire parameter space. For the $\tilde{t}\tilde{t} \rightarrow tt$ model, we find that the 1BT selection gives the lowest expected upper limit across most of the $m_{\tilde{t}}$ vs. m_{LSP} parameter space, except at lower values of Δm , where the 2BL and 2BT selection provide better sensitivity.

Based on these results, we compute the observed 95% C.L. upper limit cross section at each mass point using the selection given in Fig. 5.27. In this manner, the best search selection at a given mass point is chosen in a way that is unbiased by what is observed in the signal region. Fig. 5.28 and 5.29 show the observed upper limits for the $\tilde{g}\tilde{g} \rightarrow bbbb$ and $\tilde{g}\tilde{g} \rightarrow tttt$ models, respectively. Using the reference MSSM cross section for gluino-pair production, we exclude $\tilde{g}\tilde{g} \rightarrow bbbb$

scenarios with gluino masses up to 850 GeV for LSP masses up to 400 GeV and $\tilde{g}\tilde{g} \rightarrow tttt$ scenarios with gluino masses up to 700 GeV for LSP masses up to 150 GeV. Fig. 5.30 shows the upper limit results for the $\tilde{t}\tilde{t} \rightarrow tt$ model. Using the reference MSSM cross section for top-squark-pair production, we do not exclude any mass points in the given region. To illustrate the sensitivity of the observed results in this model, we show in Fig. 5.31 the observed upper limits together with the reference cross section as a function of $m_{\tilde{t}}$, assuming an LSP mass of 50 GeV.

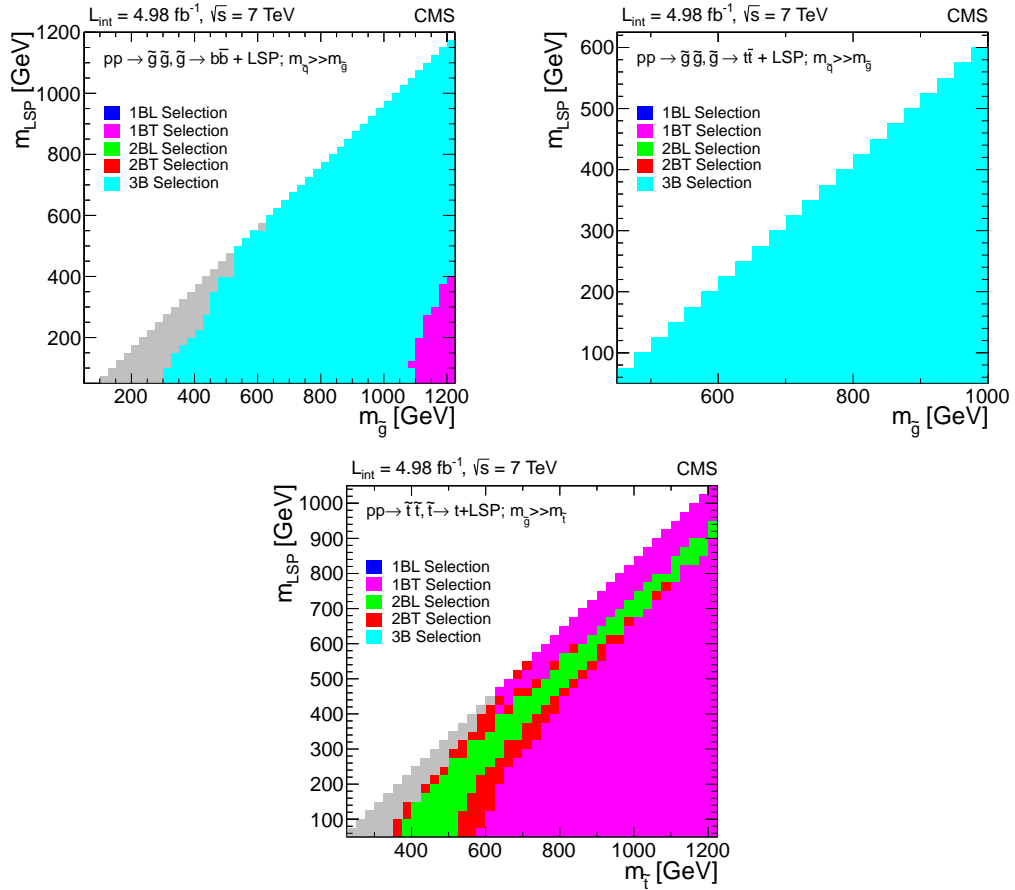


Figure 5.27: The selection that gives the lowest expected upper limit at each mass point in the $\tilde{g}\tilde{g} \rightarrow bbbb$ (top-left), $\tilde{g}\tilde{g} \rightarrow tttt$ (top-right), and $\tilde{t}\tilde{t} \rightarrow tt$ (bottom) models. The gray cells indicate mass points that are not considered due to their sensitivity to ISR.

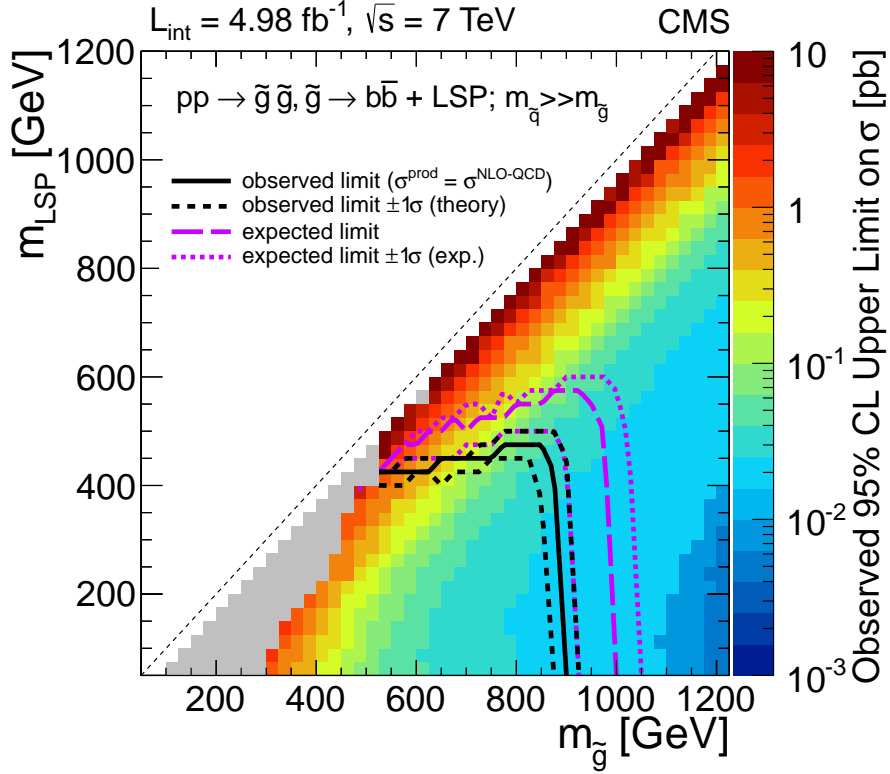


Figure 5.28: Observed 95% C.L. upper limit on the cross section for the $\tilde{g}\tilde{g} \rightarrow b\bar{b}b\bar{b}$ model with the selection at each mass point given in Fig. 5.27. The black (violet) curve shows the observed (expected) exclusion region using the reference $\tilde{g}\tilde{g}$ production cross section. Mass points below the curve are excluded. The experimental uncertainty on the expected limit corresponds to the total uncertainty on the background estimate, while the theory uncertainty on the observed limit is the uncertainty on the reference cross section.

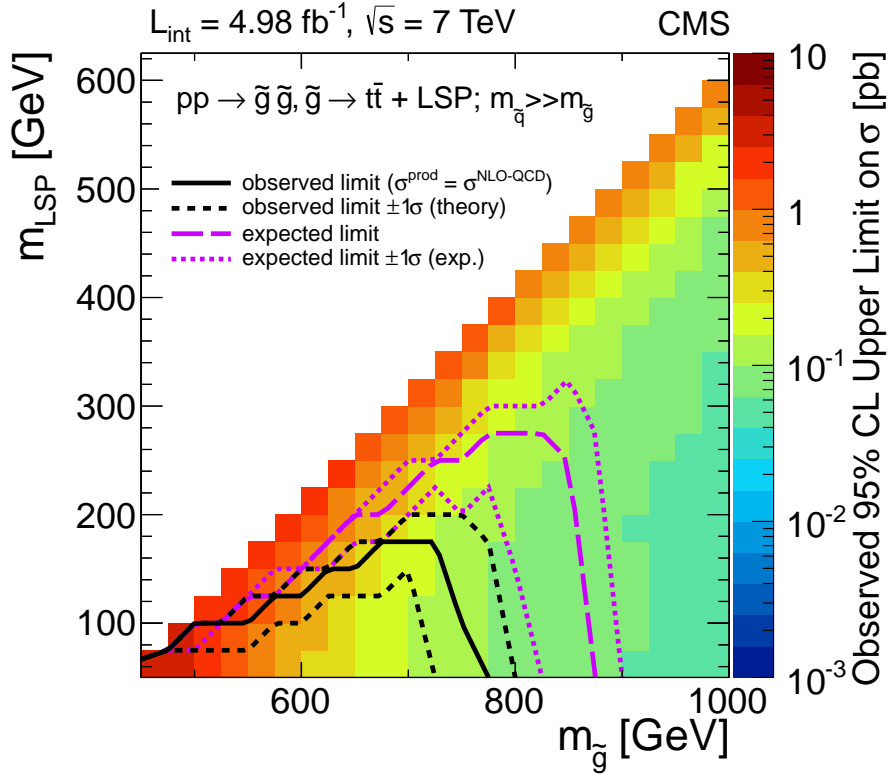


Figure 5.29: Observed 95% C.L. upper limit on the cross section for the $\tilde{g}\tilde{g} \rightarrow t\bar{t}t\bar{t}$ model with the selection at each mass point given in Fig. 5.27. The black (violet) curve shows the observed (expected) exclusion region using the reference $\tilde{g}\tilde{g}$ production cross section. Mass points below the curve are excluded. The experimental uncertainty on the expected limit corresponds to the total uncertainty on the background estimate, while the theory uncertainty on the observed limit is the uncertainty on the reference cross section.

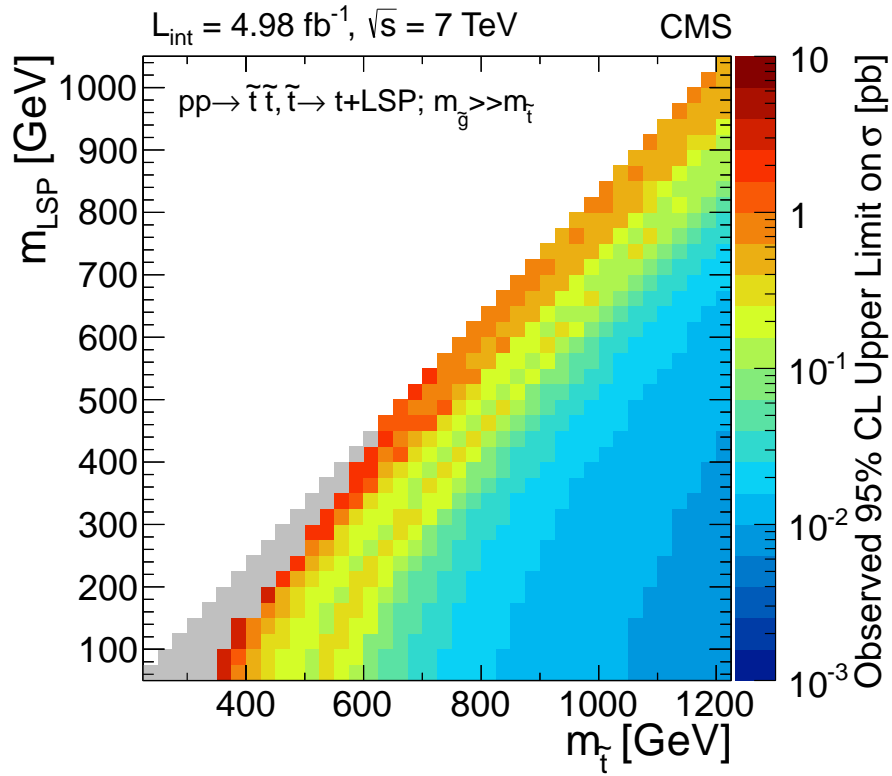


Figure 5.30: Observed 95% C.L. upper limit on the cross section for the $\tilde{t}\tilde{t} \rightarrow tt$ model with the selection at each mass point given in Fig. 5.27. We do not exclude any mass points using the reference $\tilde{t}\tilde{t}$ production cross section.

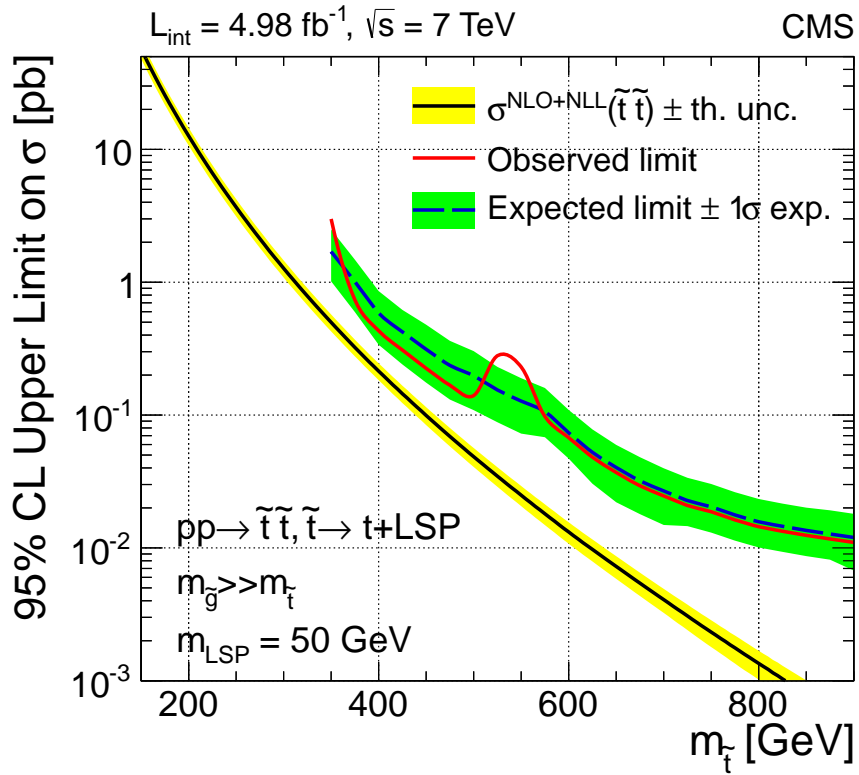


Figure 5.31: Observed (solid red curve) and expected (dashed blue curve) 95% C.L. upper limit on the cross section for the $\tilde{t}\tilde{t} \rightarrow tt$ model at $m_{\text{LSP}} = 50 \text{ GeV}$ with the 1BT selection. The experimental uncertainty on the expected limit corresponds to the total uncertainty on the background estimate. The black curve gives the reference $\tilde{t}\tilde{t}$ production cross section, with its associated uncertainty in the yellow band.

5.8.6 Event display of highest- E_T^{miss} 3B event

For illustration, we show in Fig. 5.32 and 5.33 two-dimensional displays of the event with the highest value of E_T^{miss} in the 3B selection. The event has an H_T of 1060 GeV and a E_T^{miss} of 478 GeV. A total of six jets are reconstructed, three of which are identified as b jets.

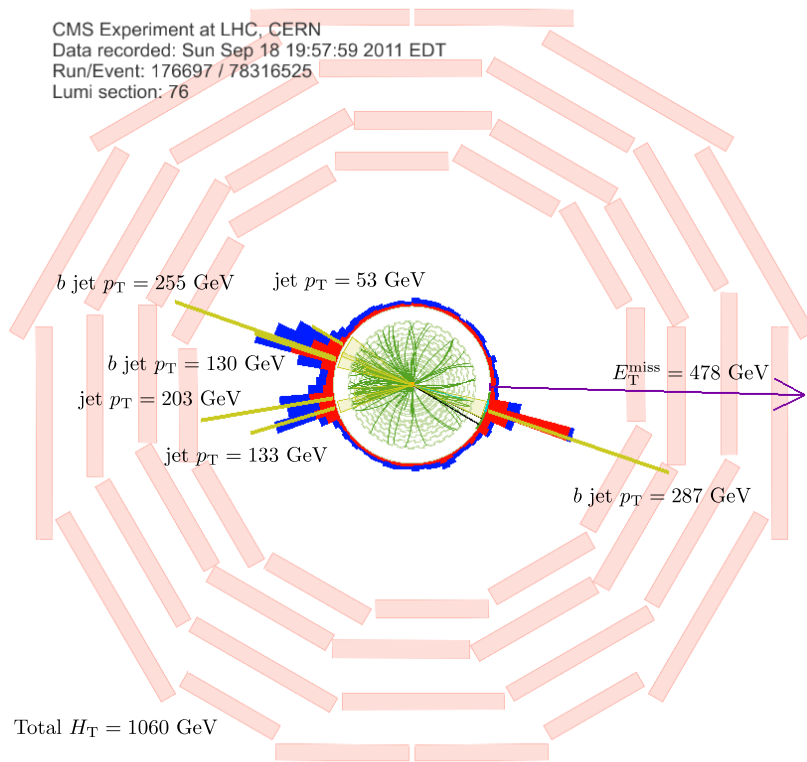


Figure 5.32: A $\rho - \phi$ view of the event with the highest value of E_T^{miss} in 3B selection. The inner green lines show the reconstructed tracks, while the red (blue) bars emanating from the central circle show the size of the ECAL (HCAL) deposits. The yellow lines give the direction of each reconstructed jet.

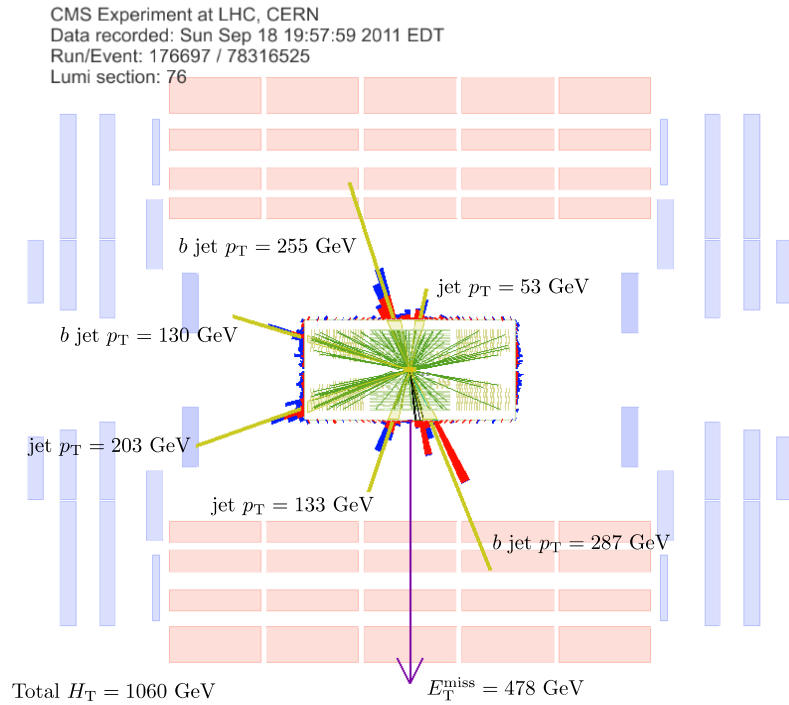


Figure 5.33: A $\rho - z$ view of the event with highest value of E_T^{miss} in 3B selection. The inner green lines show the reconstructed tracks, while the red (blue) bars emanating from the central rectangle show the size of the ECAL (HCAL) deposits. The yellow lines give the direction of each reconstructed jet.

CHAPTER 6

CONCLUSION

We have presented a search for top and bottom squarks through gluino-pair and top-squark-pair production in events with large E_T^{miss} , no leptons, at least three jets, and one or more b jets. We used a data sample corresponding to 4.98 fb^{-1} of proton-proton collisions at $\sqrt{s} = 7 \text{ TeV}$ collected by the CMS experiment in 2011. The primary sources of standard model background were evaluated using data-driven techniques. We found good agreement between the data and the sum of the background predictions. Using a global likelihood function, we have set 95% C.L. upper limits on the cross sections of b -quark-enriched SUSY models, in particular the $\tilde{g}\tilde{g} \rightarrow bbbb$, $\tilde{g}\tilde{g} \rightarrow tttt$, and $\tilde{t}\tilde{t} \rightarrow tt$ models. Using a reference MSSM scenario, we have excluded $\tilde{g}\tilde{g} \rightarrow bbbb$ models with gluino masses up to 850 GeV for LSP masses up to 400 GeV.

The LHC is currently operating at a slightly higher center-of-mass energy of 8 TeV. The CMS and ATLAS experiments are expected to each collect roughly 20 fb^{-1} of data in 2012. Moreover, the search presented here is currently being extended to incorporate a simultaneous fit to the distributions of E_T^{miss} , H_T , and $N_{b \text{ jets}}$. With the increase in luminosity and collision energy, together with the improvement in sensitivity of the analysis, we will soon be able to make a much stronger statement about the presence (or lack thereof) of natural SUSY in nature.

APPENDIX A
DATASET, TRIGGER, AND EVENT SELECTION DETAILS

A.1 List of datasets

Events were reconstructed with version 4.2.X of the official CMS software framework. The HT dataset is used to collect the main sample of events. Other datasets, including the DoubleElectron, DoubleMu, SingleMu, MuHad, and EleHad datasets are used to collect control samples for background estimates and for the measurement of trigger efficiencies.

Table A.1: Breakdown of the HT dataset used in the analysis, along with the corresponding run ranges and integrated luminosities. A similar breakdown applies for other datasets used in the analysis for background estimation and efficiency measurements.

Dataset	Run range	Luminosity (pb^{-1})
Run2011A-May10ReReco-v1	160404-163869	216
Run2011A-PromptReco-v4	165088-168437	955
Run2011A-05Aug2011-v1	170053-172619	390
Run2011A-PromptReco-v6	172620-175770	707
Run2011B-PromptReco-v1	175832-180252	2714
	Total	4982

A.2 List of triggers

Table A.2 gives a breakdown by run number of the main trigger used in the collection of the search region.

Table A.2: Triggers for signal event selection, along with the total integrated luminosity collected with each trigger.

Run range	Trigger	Integrated Luminosity (fb^{-1})
160431-161204	HLT_HT260_MHT60_v2	0.0063
161205-163268	HLT_HT250_MHT60_v2	0.0407
163269-164923	HLT_HT250_MHT60_v3	0.1687
164924-165921	HLT_HT250_MHT70_v1	0.1364
165922-166300	HLT_HT300_MHT75_v7	0.1005
166301-166373	HLT_HT300_MHT75_v8	0.0044
166374-166978	HLT_HT300_MHT75_v7	0.4366
166979-170064	HLT_HT300_MHT80_v1	0.2773
170065-173211	HLT_HT300_MHT80_v2	0.8313
173212-176544	HLT_HT300_MHT90_v2	0.6522
176545-178410	HLT_HT350_MHT90_v1	1.4421
178411-180252	HLT_HT350_MHT110_v3	0.8855

The list of triggers used in for the collection of the $Z \rightarrow l^+l^-$ control samples are given in Tables A.3 and A.4.

Table A.3: Triggers for the collection of the $Z \rightarrow e^+e^-$ control sample.

Run range	Trigger
160431-161204	HLT_Ele17_CalIdL_CaloIsoVL_Ele8_CalIdL_CaloIsoVL_v1
161205-163268	HLT_Ele17_CalIdL_CaloIsoVL_Ele8_CalIdL_CaloIsoVL_v2
163269-164923	HLT_Ele17_CalIdT_TrkIdVL_CaloIsoVL_TrkIsoVL_Ele8_CalIdT_TrkIdVL_CaloIsoVL_TrkIsoVL_v3
164924-165921	HLT_Ele17_CalIdT_TrkIdVL_CaloIsoVL_TrkIsoVL_Ele8_CalIdT_TrkIdVL_CaloIsoVL_TrkIsoVL_v4
165922-166978	HLT_Ele17_CalIdT_TrkIdVL_CaloIsoVL_TrkIsoVL_Ele8_CalIdT_TrkIdVL_CaloIsoVL_TrkIsoVL_v5
166979-170064	HLT_Ele17_CalIdT_CaloIsoVL_TrkIdVL_TrkIsoVL_Ele8_CalIdT_CaloIsoVL_TrkIdVL_TrkIsoVL_v5
170065-170825	HLT_Ele17_CalIdT_CaloIsoVL_TrkIdVL_TrkIsoVL_Ele8_CalIdT_CaloIsoVL_TrkIdVL_TrkIsoVL_v6
170826-173211	HLT_Ele17_CalIdT_CaloIsoVL_TrkIdVL_TrkIsoVL_Ele8_CalIdT_CaloIsoVL_TrkIdVL_TrkIsoVL_v7
173212-178410	HLT_Ele17_CalIdT_CaloIsoVL_TrkIdVL_TrkIsoVL_Ele8_CalIdT_CaloIsoVL_TrkIdVL_TrkIsoVL_v8
178411-179941	HLT_Ele17_CalIdT_CaloIsoVL_TrkIdVL_TrkIsoVL_Ele8_CalIdT_CaloIsoVL_TrkIdVL_TrkIsoVL_v9
179942-180252	HLT_Ele17_CalIdT_CaloIsoVL_TrkIdVL_TrkIsoVL_Ele8_CalIdT_CaloIsoVL_TrkIdVL_TrkIsoVL_v10

Table A.4: Triggers used for the collection of the $Z \rightarrow \mu^+ \mu^-$ control sample

Run range	Trigger
160431-163268	HLT_DoubleMu7_v1
163269-164923	HLT_DoubleMu7_v2
164924-166300	HLT_Mu13_Mu8_v2
166301-166373	HLT_Mu13_Mu8_v3
166374-167077	HLT_Mu13_Mu8_v2
167078-170064	HLT_Mu13_Mu8_v4
170065-173211	HLT_Mu13_Mu8_v6
173212-178410	HLT_Mu13_Mu8_v7
178411-179941	HLT_Mu17_Mu8_v10
179942-180252	HLT_Mu17_Mu8_v11

A.3 Systematic uncertainty on trigger efficiency

The efficiency of the H_T^{miss} component of the trigger, given in Table 5.7, is measured using offline selection criteria that are similar to the criteria of the search regions in which the efficiencies are applied. Due to a lack of statistics (and in order to be statistically independent from the search region), the efficiencies cannot be measured using completely identical selection criteria as the requirements for the search region. The most significant difference is the use of a zero b jet requirement for the efficiency measurements. Therefore, the sample composition between the regions where the efficiencies are measured and where the efficiencies are applied will be different. We study in this section the effect of such differences on the H_T^{miss} efficiency for the case of the SB and SB-LDP regions.

Table A.5 shows the sample composition (from MC) of the 0-lepton regions where the efficiencies are measured ¹. Both regions are dominated by QCD events. Table A.6 shows the sample composition of the regions where the efficiencies are used. The SB regions are dominated by $t\bar{t}$ events, while the SB-LDP regions are dominated by QCD events. Thus, there is a large difference in the sample composition for the case of the SB region, and a small difference for the case of the SB-LDP region.

To estimate the impact of such differences in the sample composition on the H_T^{miss} efficiencies, we measure from the data the H_T^{miss} efficiencies for each of the top, V+jets, and QCD processes separately. This is done by selecting a control sample that is enriched in each process. The selection choice and the measured efficiencies are given in Table A.7. Using these efficiencies, we compute the “process-weighted” H_T^{miss} efficiency of each of the regions in Tables A.5 and A.6:

$$\epsilon = f_{\text{top}} \cdot \epsilon_{\text{top}} + f_{\text{V+jets}} \cdot \epsilon_{\text{V+jets}} + f_{\text{QCD}} \cdot \epsilon_{\text{QCD}}, \quad (\text{A.1})$$

where f_{top} , $f_{\text{V+jets}}$, and f_{QCD} are the corresponding fractional contributions of each process, and ϵ_{top} , $\epsilon_{\text{V+jets}}$, and ϵ_{QCD} are the efficiencies in Table A.7. We compute a value of 92.9% for the SB region where the efficiency is measured and range of 87.7-89.8% for the analysis SB (1BL to 3B) selections. The maximum difference observed is 5.6%. Similarly, we compute a value of 91.4% for the SB-LDP region where the efficiency is measured and 90.0%-90.8% for the analysis SB-LDP regions, which gives a maximum difference of 1.5%. The values 5.6% and 1.5% are treated as systematic errors to the efficiency measurements of the SB and SB-LDP regions, respectively.

The effect of sample composition is expected to be negligible for the SIG and

¹In this section, “top” is the sum of $t\bar{t}$ and single-top events, and “V+jets” is the sum of $W \rightarrow l\nu, Z/\gamma^* \rightarrow l^+l^-, Z \rightarrow \nu\bar{\nu}$, and diboson events.

Table A.5: Fractional sample composition of two regions in which the H_T^{miss} efficiencies are measured. The efficiencies measured in these regions are used in the SB and SB-LDP regions of the analysis.

Selection	top	V+jets	QCD
$\Delta\hat{\phi}_{\text{min}} > 4$	2%	40%	58%
$\Delta\hat{\phi}_{\text{min}} \leq 4$	1%	8%	91%

Table A.6: Fractional sample composition of the regions in which the H_T^{miss} efficiencies are used. The E_T^{miss} and $\Delta\hat{\phi}_{\text{min}}$ cuts are specified by the first column, while all other offline cuts correspond to the selections denoted in the second column.

Region	Other Selection	top	V+jets	QCD
SB	1BL	60%	21%	19%
	1BT	55%	20%	25%
	2BL	78%	7%	15%
	2BT	71%	7%	22%
	3B	88%	4%	8%
SB-LDP	1BL	12%	4%	84%
	1BT	11%	4%	85%
	2BL	18%	2%	80%
	2BT	18%	1%	81%
	3B	27%	1%	72%

SL regions, where the difference in sample composition is less severe, and where the overall H_T^{miss} efficiency is nearly 100%.

Table A.7: H_T^{miss} efficiency measured in control samples enriched in either top, V+jets, or QCD events. A common selection criteria of $\{150 < E_T^{\text{miss}} < 250, H_T \geq 400 \text{ GeV, no leptons}\}$ is applied.

Process	Selection	Efficiency (%)
top	$\geq 1 b, \Delta\hat{\phi}_{\text{min}} > 8$	87^{+5}_{-10}
V+jets	$0b, \Delta\hat{\phi}_{\text{min}} > 8$	96^{+2}_{-5}
QCD	$0b, \Delta\hat{\phi}_{\text{min}} < 4$	91^{+3}_{-6}

A.4 Anomalous E_T^{miss} filters

In a small class of events, a large value of E_T^{miss} can be induced if (a) an energetic particle or jet strikes an inactive region of the detector, or (b) if the reconstruction algorithm fails to assign the appropriate momentum to the object. Such sources of E_T^{miss} tend to be difficult to model in the simulation. Therefore, to reduce the likelihood of events with fake, anomalous sources of E_T^{miss} from entering the search, we apply the following filters:

- **Scraping veto filter:** For events with 10 or more tracks, at least 25% of the tracks must satisfy the high-purity track requirements (Section 4.1). This filter reduces the contribution from beam scraping events.
- **HB/HE noise filter:** Anomalous noise from the HCAL barrel and endcap regions can arise from the underlying behavior of the HPD's and their readout boxes. The identification of this source of noise is based on unique characteristics of the signal, including the hit multiplicity, isolation, and the shape of the pulse across time-slices [58].
- **CSC beam-halo filter:** Events with E_T^{miss} arising from the production of muons due to proton collisions upstream of the detector ("beam-halo" muons) are identified through the reconstruction of muons in the CSC detectors with trajectories mostly parallel to the beam-line [59].
- **Tracking failure filter:** Fake E_T^{miss} can occur in events for which either the tracking algorithm fails during one of the tracking iterations due to an excessively large number of clusters, or the event consisted of a collision with a satellite bunch displaced from the nominal interaction region. To reject such events, we require that the ratio of the sum- p_T of tracks near

the nominal interaction point and the sum- p_T of all reconstructed jets be larger than 0.1.

- **ECAL dead-cell filter:** Crystals for which the Very Front End and Front End boards are known to have no data link are masked during reconstruction. Energetic particles or jets that strike such crystals will not be reconstructed, thereby inducing large E_T^{miss} in the event. Such events are rejected by checking for large energy deposits in these crystals using information from the trigger primitives, which do contain hit information on these crystals.
- **EE noise filter:** Events in which an excessively large number of energy deposits across the entire ECAL endcap detector is found are removed by requiring that the maximum number of hits in the endcap regions not exceed 2000.
- **Greedy/Inconsistent muon filter:** In rare instances, a muon can inherit an excessive amount of calorimeter energy during its reconstruction. We reject events with muons that have a calorimeter energy larger than its track momentum. In addition, events in which a muon with $p_T > 100 \text{ GeV}$ has inner-track and global-track momentum measurements that differ by more than 10% are discarded.

We find the rejection rate of the E_T^{miss} tail-cleaning filters on SUSY signal events to be $< 1\%$.

APPENDIX B

DATA-BASED CORRECTIONS TO THE MC SIMULATION

We apply a series of corrections to the MC samples to improve the agreement of the simulation with the data.

The energy resolution of jets is found to differ slightly between the data and the MC. We apply the correction factors measured in Reference [48] by scaling the difference in p_T with respect to the corresponding matched generator-level jet of each reconstructed jet. The corrections to the resolution are on the order of 5% to 10%. The corrections to the jet p_T are propagated into the computation of the E_T^{miss} for all jets with $p_T > 10$ GeV. We evaluate a systematic uncertainty on this procedure by varying the corrections by their uncertainties [48].

The MC samples were produced with an average of roughly 6 pile-up interactions per event. Due to the rapidly evolving luminosity of the LHC, it was not possible to know the precise pile-up distribution of the data at the time when the MC samples were produced. Therefore, we apply a weight to the events in the MC based on the final observed distribution of the number of pile-up interactions in the data. We compute the weights using an inelastic pp scattering cross-section of 68 mb. We assign an uncertainty of 8% on this value when computing the uncertainty on these weights.

The efficiency to identify true b jets (b -tag efficiency) and the probability of mis-identifying non- b jets as b jets (mis-tag rate) has been found to differ slightly between the data and simulation [34]. We correct for this difference using the following procedure. Instead of requiring explicitly in the MC that events have a particular number of b jets, we evaluate the probability for each event to have

a given number of b jets as:

$$P(0 \text{ } b \text{ jets}) = \prod_i (1 - \varepsilon_i), \quad (\text{B.1})$$

$$P(1 \text{ } b \text{ jet}) = \sum_i \varepsilon_i \left(\prod_{j \neq i} (1 - \varepsilon_j) \right), \quad (\text{B.2})$$

$$P(2 \text{ } b \text{ jets}) = \sum_i \varepsilon_i \left(\sum_{j > i} \varepsilon_j \left(\prod_{k \neq i, j} (1 - \varepsilon_k) \right) \right), \quad (\text{B.3})$$

where ε_i is the probability for jet i to be identified as a b jet, and where the sums are over all jets in the event satisfying the requirements of Sec. 5.3. The value of ε_i depends on the flavor of the jet (b , c , or light-flavored) and on the jet p_T . The efficiencies are determined with each MC sample separately. We can then compute the probability of an event passing a $\geq 1b$, $\geq 2b$, or $\geq 3b$ requirement as:

$$P(\geq 1 \text{ } b \text{ jet}) = 1 - P(0 \text{ } b \text{ jets}) \quad (\text{B.4})$$

$$P(\geq 2 \text{ } b \text{ jets}) = 1 - P(0 \text{ } b \text{ jets}) - P(1 \text{ } b \text{ jet}) \quad (\text{B.5})$$

$$P(\geq 3 \text{ } b \text{ jets}) = 1 - P(0 \text{ } b \text{ jets}) - P(1 \text{ } b \text{ jet}) - P(2 \text{ } b \text{ jets}). \quad (\text{B.6})$$

If we denote the set of events satisfying all selection criteria except for the requirement on the number of b jets as the “pre- b ” sample, then the sum of probabilities over all events in the pre- b sample gives the expected number of events passing the given b jet requirement. For example, we have $N(\geq 2 \text{ } b \text{ jets}) = \sum_{\text{events}}^{N_{\text{pre-}b}} P(\geq 2 \text{ } b \text{ jets})$.

One advantage of using this method to impose the b jet condition is that one can make use of the full statistics of the MC sample available in the pre- b sample, whereas explicitly requiring a b jet requirement can significantly reduce the size of the MC statistics. This is particularly true for QCD-background processes, where a relatively small fraction of the total MC sample contain events with

true b jets. Another advantage is the ability to directly apply a correction factor to the b -tag and mistag efficiencies. Indeed, we simply make the replacement $\varepsilon_i \rightarrow SF_i \cdot \varepsilon_i$, where SF_i is the “scale-factor” correcting the MC efficiency. The scale-factor for the b -tag (mis-tag) efficiency is about 0.95 (1.10) over a large jet- p_T range. Moreover, we evaluate an uncertainty due to this correction by varying SF_i by its systematic uncertainty [34].

A final correction that we apply to the MC is the efficiency of the trigger. These correspond both to the H_T and H_T^{miss} components, as described in Sec. 5.4. We apply as a systematic uncertainty to this correction the combination of the statistical uncertainty on the efficiency measurement and the uncertainty described in App. A.3.

APPENDIX C

BACKGROUND ESTIMATE DETAILS

C.1 QCD SB estimate

We show here the corresponding information for the prediction of the QCD background in the SB region. Table C.1 shows the results of the closure test. Table C.2 gives the background predictions from the data. The systematic uncertainties on the estimates are summarized in Table C.3.

Table C.1: Closure test of the QCD background method in QCD MC for the SB region. Closure results are reported in %.

Selection	R^{QCD}	$N_{\text{SB-LDP}}$	$N_{\text{SB}}^{\text{QCD}}(\text{pred})$	$N_{\text{SB}}^{\text{QCD}}(\text{true})$	Closure
1BL	0.131 ± 0.002	3174 ± 134	417 ± 19	392 ± 65	6 ± 16
1BT	0.092 ± 0.002	2523 ± 96	232 ± 10	293 ± 44	-26 ± 20
2BL	0.131 ± 0.002	876 ± 60	115 ± 8	103 ± 23	11 ± 21
2BT	0.067 ± 0.001	494 ± 34	33 ± 2	48 ± 14	-44 ± 44
3B	0.131 ± 0.002	70 ± 16	9 ± 2	6 ± 1	34 ± 20

Table C.2: QCD-background prediction in the SB region. $N_{\text{SB-LDP}}^{\text{top+W}}$ is the total non-QCD contamination in the SB-LDP region. Errors are statistical only.

Selection	R^{QCD}	$N_{\text{SB-LDP}}$	$N_{\text{SB-LDP}}^{\text{top+EW}}$	$N_{\text{SIG}}^{\text{QCD}}$
1BL	0.170 ± 0.004	4098	599 ± 3	564 ± 17
1BT	0.117 ± 0.005	3294	453 ± 3	314 ± 13
2BL	0.170 ± 0.004	925	213 ± 1	116 ± 5
2BT	0.083 ± 0.005	578	120 ± 1	36 ± 3
3B	0.170 ± 0.004	86	26.3 ± 0.3	10 ± 1

Table C.3: Systematic uncertainties (in %) on the QCD prediction in the SB region.

Selection	Non-QCD	Closure	LSB range	LSB PV	Trigger	Total
1BL	6.2	27	0.3	7.9	9.5	30
1BT	5.7	40	1.1	9.0	9.5	42
2BL	11	34	0.3	7.9	9.9	38
2BT	9.4	69	5.8	9.8	9.8	71
3B	16	45	0.3	7.9	10	50

C.2 $Z \rightarrow \nu\bar{\nu}$ SB estimate

We show here the corresponding information for the prediction of the $Z \rightarrow \nu\nu$ background in the SB region. Table C.4 gives the systematic uncertainties to the $Z \rightarrow \nu\nu$ prediction. The predictions from each of the $Z \rightarrow e^+e^-$ and $Z \rightarrow \mu^+\mu^-$ control samples are shown in Table C.5. The combined prediction is given in Table C.6.

Table C.4: Systematic uncertainties (in %) for $Z \rightarrow \nu\bar{\nu}$ background prediction in SB region.

Selection	\mathcal{P}	ε_{trig}	ε_{sel}^2	Closure	\mathcal{F}	Total
$Z \rightarrow e^+e^-$						
1BL	10	4	20	25	11	36
1BT	10	4	20	22	52	61
2BL	10	4	20	29	83	90
2BT	10	4	20	48	77	93
3B	10	4	20	218	100	241
$Z \rightarrow \mu^+\mu^-$						
1BL	10	4	14	37	34	53
1BT	10	4	14	37	13	43
2BL	10	4	14	38	23	48
2BT	10	4	14	53	73	91
3B	10	4	14	87	100	134

Table C.5: Results for the $Z \rightarrow \nu\bar{\nu}$ background prediction in the SB region. Errors are statistical only.

Selection	$N_{\text{SB-DL}}$	\mathcal{F}	\mathcal{A}	ε	$N_{\text{SB}}^{Z \rightarrow \nu\bar{\nu}}$
$Z \rightarrow e^+e^-$					
1BL	48 ± 7	0.45 ± 0.06	0.597 ± 0.004	0.59 ± 0.08	332 ± 83
1BT	21 ± 5	0.42 ± 0.10	0.600 ± 0.006	0.59 ± 0.08	133 ± 48
2BL	48 ± 7	0.11 ± 0.04	0.597 ± 0.004	0.59 ± 0.08	81 ± 34
2BT	11 ± 3	0.11 ± 0.04	0.600 ± 0.009	0.59 ± 0.08	19 ± 10
3B	48 ± 7	0.006 ± 0.006	0.597 ± 0.004	0.59 ± 0.08	4 ± 4
$Z \rightarrow \mu^+\mu^-$					
1BL	44 ± 7	0.43 ± 0.05	0.611 ± 0.004	0.55 ± 0.05	289 ± 94
1BT	24 ± 5	0.38 ± 0.08	0.629 ± 0.006	0.55 ± 0.05	136 ± 54
2BL	44 ± 7	0.12 ± 0.04	0.611 ± 0.004	0.55 ± 0.05	78 ± 34
2BT	13 ± 4	0.12 ± 0.04	0.631 ± 0.009	0.55 ± 0.05	22 ± 12
3B	44 ± 7	0.006 ± 0.005	0.611 ± 0.004	0.55 ± 0.05	4 ± 4

Table C.6: Combined prediction for the $Z \rightarrow \nu\bar{\nu}$ background in the SB region. Both statistical and systematic errors are included.

	$N_{\text{SB}}^{Z \rightarrow \nu\bar{\nu}}$ (from $Z \rightarrow e^+e^-$)	$N_{\text{SB}}^{Z \rightarrow \nu\bar{\nu}}$ (from $Z \rightarrow \mu^+\mu^-$)	$N_{\text{SB}}^{Z \rightarrow \nu\bar{\nu}}$ (average)
1BL	332 ± 144	289 ± 180	315 ± 113
1BT	133 ± 94	136 ± 79	135 ± 61
2BL	81 ± 80	78 ± 51	79 ± 43
2BT	19 ± 20	22 ± 24	20 ± 15
3B	4 ± 12	4 ± 7	4 ± 6

APPENDIX D

DIFFERENCES WITH RESPECT TO PUBLISHED RESULT

This section outlines the major differences between the results presented in this thesis and in the publication [60]. The differences arise primarily in (a) the estimation of the $Z \rightarrow \nu\nu$ background and (b) the method used to estimate the top + W background for the interpretation of the results with the $\tilde{g}\tilde{g} \rightarrow bbbb$ signal model.

The $Z \rightarrow l^+l^-$ MC sample used in the thesis corresponds to one with a higher equivalent luminosity relative to the sample used for the published result. The higher statistics sample provides a more precise evaluation of the level of closure in the $Z \rightarrow \nu\nu$ background prediction technique.

A second difference arises in the measurement of the lepton selection efficiency of the $Z \rightarrow l^+l^-$ control sample. While the overall procedure of obtaining these quantities is identical to that of the publication, a slightly different choice of signal and background shapes were chosen for the fit to the invariant mass distributions, leading to a difference of about 5% in the measured values.

The most significant difference in the $Z \rightarrow l^+l^-$ background prediction method arises from the treatment of the extrapolation factor \mathcal{F} . Firstly, the definition of a loose b jet in this thesis is one that satisfies the requirement $d_{CSV} \geq 0.244$ (Sec. 5.6.1). An alternate b jet identification algorithm, based only on the impact parameter significance of associated tracks (Sec. 4.7), was chosen for the publication. The two choices of algorithms and discriminant values turn out to have comparable b -tag efficiencies and mis-tag rates. Indeed, the size of the SIG-DL and SB-DL samples (Table 5.5) is similar between these two defi-

nitions. Secondly, the value of \mathcal{F} is measured in a different control sample in the publication. Instead of extracting \mathcal{F} from a low E_T^{miss} /low H_T region of the $Z \rightarrow l^+l^-$ control sample, a sample obtained by inverting the nominal requirement on $\Delta\hat{\phi}_{\text{min}}$ (i.e. requiring a $\Delta\hat{\phi}_{\text{min}} < 4$ cut) is used in the publication. This results in a different treatment of the systematic uncertainty on \mathcal{F} .

The items mentioned above lead to a difference in the total expected SM background of $\sim 30\%$ for the 1BT selection, $\sim 10\%$ for the 3B selection, and a few percent for the other selections, relative to the predictions in this thesis. The difference is largest for the 1BT selection due to the relatively large contribution of the $Z \rightarrow \nu\nu$ background for that selection. Consequently, the exclusion limit obtained for the $\tilde{g}\tilde{g} \rightarrow tttt$ model is larger in this thesis by about 50 GeV for $m_{\text{LSP}} = 50$ GeV.

Finally, the cross-section upper limits reported in the publication for the $\tilde{g}\tilde{g} \rightarrow bbbb$ model are obtained with an alternate method for estimating the top + W background. This results in exclusion limits that are about 50 GeV higher (at $m_{\text{LSP}} = 50$ GeV) relative to the exclusion limits presented in this thesis.

APPENDIX E

DATA QUALITY MONITORING FOR THE DRIFT TUBE TRACK FINDER

The optimal performance of the Drift Tube Track Finder (DTTF), which is responsible for the reconstruction of muon tracks in the drift-tube chambers at the L1 trigger, is crucial in ensuring a high quality of the collected data. This appendix describes the tools developed within the central data-quality-monitoring (DQM) framework to provide prompt feedback on the health of the DTTF system.

E.1 Drift Tube Track Finder system

A description of the CMS drift-tube system is given in Sec. 3.2. The task of the DTTF is to reconstruct muon candidates using track segments made from the local trigger of the DT chamber electronics. A track segment is constructed if at least three out of the four planes of drift cells within a superlayer have aligning hits. For each chamber, a maximum of two segments with the smallest bending angles (i.e. highest momenta) are sent to the DTTF.

A schematic of the DTTF system is shown in Fig. E.1. The joining of track segments in the ϕ -projection within each of the 12 DT sectors of a wheel is performed by a Phi Track Finder (PHTF). The track momentum is inferred from the bending induced by the B -field in the return yoke. The central wheel of the DT system is split into two logical units, with the half in the positive z coordinate responsible for tracks that remain in the central wheel and for tracks that exit the positive side, and the other half responsible only for the scenario in which tracks exit the negative side. The sector boundaries must communicate

with each other in the case where a muon crosses multiple sectors. The determination of the track η is accomplished with the Eta Track Finders (ETTF), each covering one of the 12 DT wedges.

The tracks from each of the wedges are sent to a wedge sorter, which selects the two highest-rank muons in the wedge. The ranking is based on the quality and p_T of the reconstructed tracks. Finally, a barrel sorter receives the candidates from each of the wedges and forwards the four best muons of the entire muon barrel system to the Global Muon Trigger.

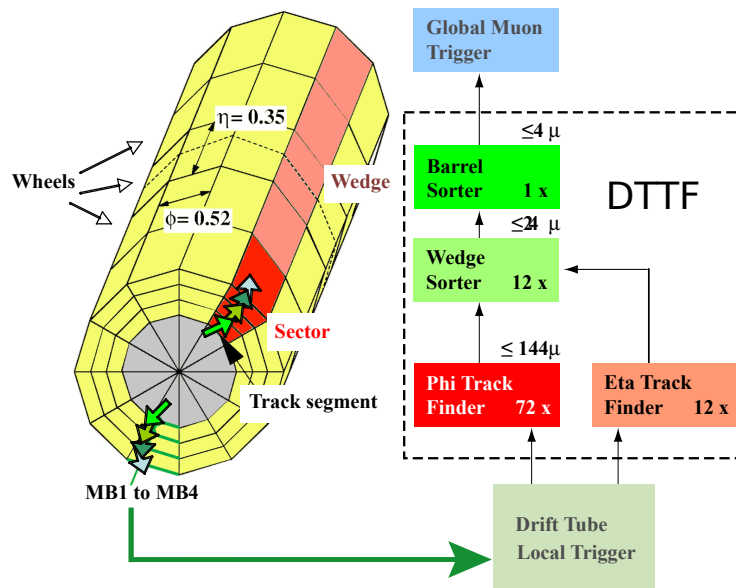


Figure E.1: Schematic of the DTF system [61]. For the purposes of track-finding, the central wheel is logically divided into two halves.

E.2 Data Quality Monitoring system

To ensure that all detectors and trigger systems are operating as expected and collecting good quality data, a data quality monitoring (DQM) system has been

developed. An illustration of the DQM workflow is shown in Fig. E.2. The system comprises of a set of tools for creating, filling, and archiving information collected by the detectors in the form of histograms and scalars. In addition, automated quality tests can be implemented on the histograms. The first stage of monitoring, called *online* monitoring, occurs during data-taking, where a subset of the accepted events are read from the storage manager at a rate of 10-15 Hz. At this stage, histograms are filled in real-time and available for visual inspection via a web-based GUI. A second monitoring stage, *offline* monitoring, occurs with a latency of a few days. At this stage, one can check the quality of the data on tape under various reconstruction configurations, calibration and alignment settings, and software releases. The results of this monitoring stage are also available on the web-based GUI.

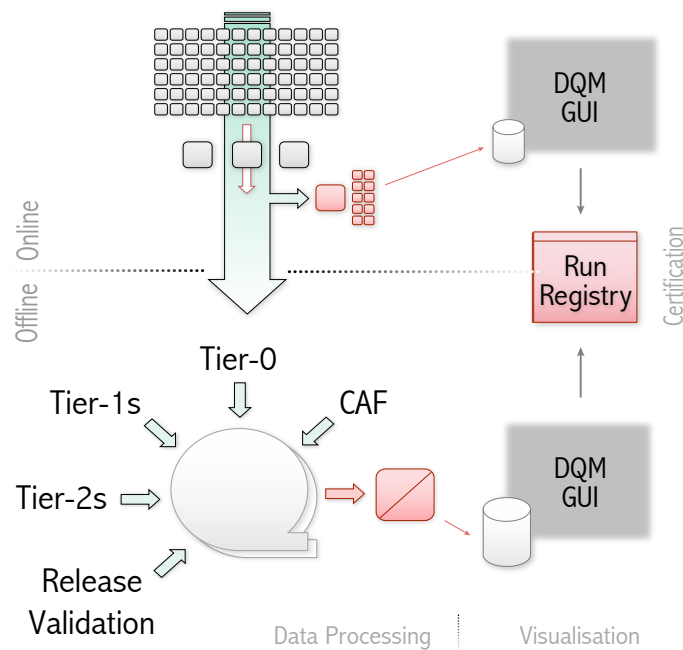


Figure E.2: Schematic of the two stages of the DQM workflow [62].

E.3 DTTF DQM

The online monitoring application of the DTTF is organized to give a hierarchical view of the system. A set of top-level plots provide a quick summary of the data collected from the system. This allows easy identification of obvious problems with the DTTF. Examples of top-level plots taken from collision run #180250 are shown in Fig. E.3 to E.6. Fig. E.3 shows the integrated occupancy of tracks in both physical (η, ϕ) coordinates and in terms of the DT sectors of each wheel. The latter display shows, for example, that the wheel labeled N0 registers only a small number of hits compared to the other wheels. This is due to the logical configuration of the negative-central wheel, as explained above, and is an expected behavior. Fig. E.4 shows the kinematics of all reconstructed tracks. Fig. E.5 shows the quality code of the tracks. The lower quality of tracks in the outer wheels, due to the lower geometrical acceptance in those regions, can be clearly seen. Fig. E.6 shows the bunch crossing assignment of the tracks. This plot alerts shifters of potential issues in which tracks are assigned the incorrect bunch crossing, which, in the case of an early bunch crossing assignment, causes a loss of data.

The directory structure of the plots are organized in the DQM GUI for optimal browsing. For a more detailed assessment of the DTTF, plots can be viewed for each wheel and each sector separately. In addition, plots of only the second-rank muon of each wedge sorter are displayed. This allows the viewer to disentangle effects arising only from these tracks.

Finally, we include plots that monitor the communication between the DTTF and the Global Muon Trigger (GMT). Tracks from the DTTF may be deleted

by the algorithms in the wedge and barrel sorters, which may classify certain tracks as “fake” muons. One such example is a duplicated track between η -adjacent PHTF’s caused by a muon crossing a wheel boundary. Fake muons will therefore fail to appear in the GMT. Fig. E.7 shows example displays of the DTF-GMT matching information.

The online DTF DQM application has been operational since the beginning of the cosmic-ray data-taking era in 2008. They continue to the present day to be an instrumental part of the real-time monitoring of the health of the DT system at the L1 trigger.

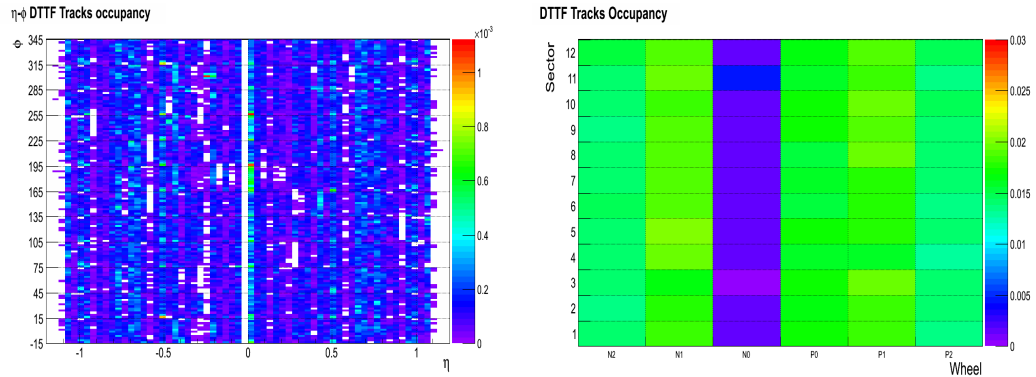


Figure E.3: Distribution of the track occupancy in $\eta - \phi$ space (left) and divided into the DT sectors vs. wheels (right). The low occupancy of wheel N0 is visible and arises from the fact that the wheel is responsible only for reconstructing tracks that exit the central wheel from the negative side.

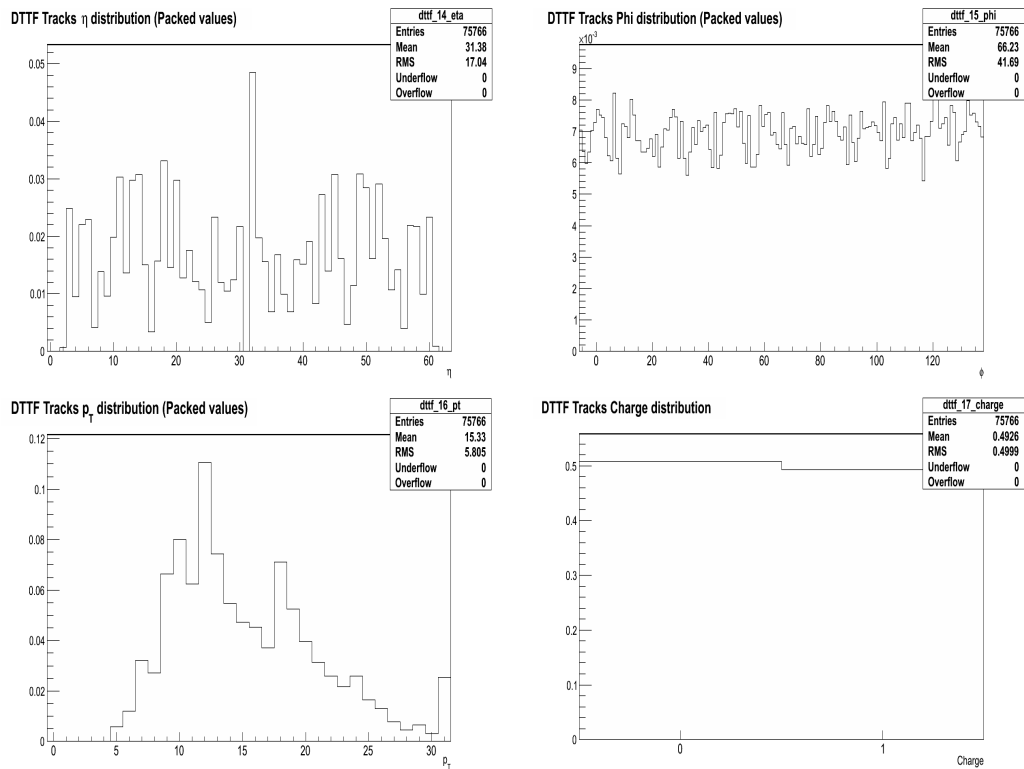


Figure E.4: Distributions of track η (top-left), ϕ (top-right), p_T (bottom-left), and charge (bottom-right). The cracks between DT sectors can be seen in the track- ϕ distribution.

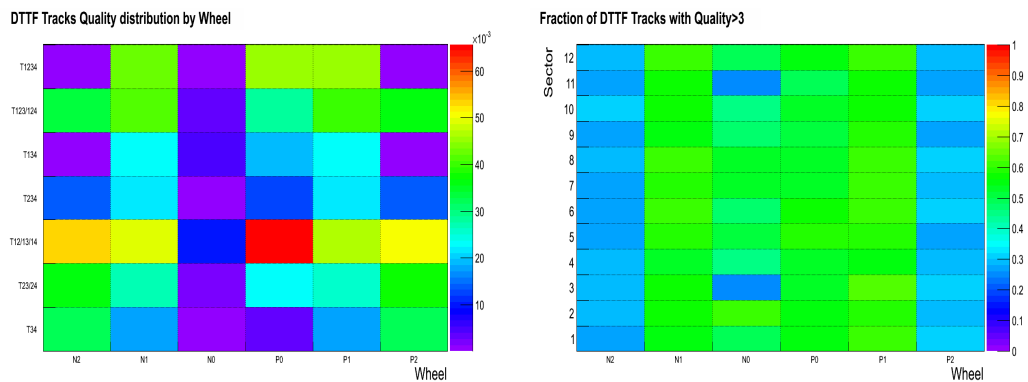


Figure E.5: Track quality information. The left plot gives the distribution of track quality codes in each wheel. The seven quality codes on the y-axis are arranged in order of increasing quality. The right plot gives the fraction of tracks with quality code > 3 (corresponding to “T12/13/14” on the left plot) for each sector of each wheel.

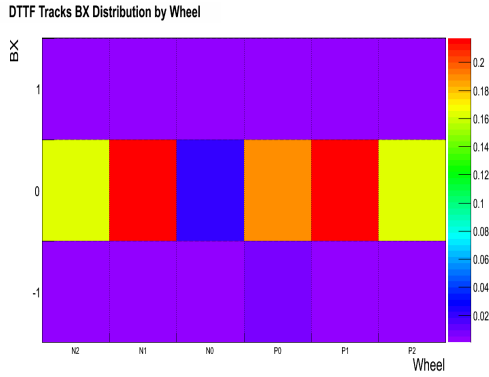


Figure E.6: Distribution of the bunch crossing assignment of tracks for each wheel. In this run, most tracks are assigned the correct bunch crossing (BX=0).

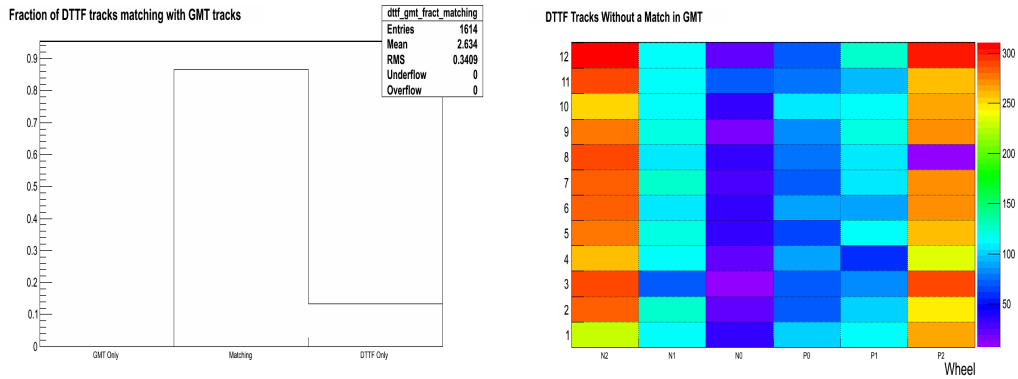


Figure E.7: Information on the communication between the DTF and GMT. The left plot shows the fraction of tracks that have matching GMT tracks. The right plot gives the fraction of DTF tracks without a GMT match per sector and wheel. The increase in deleted tracks in the external wheels is clearly visible.

BIBLIOGRAPHY

- [1] The Particle Data Group, "Review of Particle Physics," *Phys. Rev. D* **86** (2012) 010001.
- [2] H. Baer and X. Tata, *Weak Scale Supersymmetry: From Superfields to Scattering Events*. Cambridge University Press, 2006.
- [3] S. P. Martin, "A Supersymmetry primer," (1997) ,
arXiv:hep-ph/9709356.
- [4] M. Papucci, J. T. Ruderman, and A. Weiler, "Natural SUSY Endures," *J. High Energy Phys.* **1209** (2012) 035.
- [5] C. Brust, A. Katz, S. Lawrence, and R. Sundrum, "SUSY, the Third Generation and the LHC," *J. High Energy Phys.* **2012** (2012) 1–33.
- [6] Y. Kats, P. Meade, M. Reece, and D. Shih, "The status of GMSB after 1/fb at the LHC," *J. High Energy Phys.* **2012** (2012) 1–41.
- [7] M. Krämer, A. Kulesza, R. van der Leeuw, M. Mangano, S. Padhi, T. Plehn, and X. Portell, "Supersymmetry production cross sections in pp collisions at $\sqrt{s} = 7$ TeV," (2012) , arXiv:1206.2892.
- [8] D. Alves *et al.*, "Simplified models for LHC new physics searches," *J. Phys. G* **39** no. 10, (2012) 105005.
- [9] The CMS collaboration, "Interpretation of searches for supersymmetry," CMS Physics Analysis Summary Report No. CMS-PAS-SUS-11-016, 2012.
<http://cds.cern.ch/record/1445580>.
- [10] L. Evans and P. Bryant, "LHC Machine," *J. Instrum.* **3** no. 08, (2008) S08001.

- [11] The CMS collaboration, "The CMS experiment at the CERN LHC," *J. Instrum.* **3** (2008) S08004.
- [12] Forthommel, Used under Creative Commons Attribution-Share Alike 3.0 Unported License, Retrieved 24, May 2011, from <http://upload.wikimedia.org/wikipedia/commons/b/ba/Cern-accelerator-complex.svg>.
- [13] The CMS collaboration, *CMS Physics Technical Design Report Volume I: Detector Performance and Software*. Technical Design Report CMS. CERN/LHCC, Geneva, 2006. <http://cds.cern.ch/record/922757>.
- [14] The CMS collaboration, "Commissioning and performance of the CMS pixel tracker with cosmic ray muons," *J. Instrum.* **5** (2010) T03007.
- [15] The CMS collaboration, "Commissioning and performance of the CMS silicon strip tracker with cosmic ray muons," *J. Instrum.* **5** (2010) T03008.
- [16] The CMS collaboration, "Performance and operation of the CMS electromagnetic calorimeter," *J. Instrum.* **5** (2010) T03010.
- [17] P. Adzic *et al.*, "Energy resolution of the barrel of the CMS Electromagnetic Calorimeter," *J. Instrum.* **2** no. 04, (2007) P04004.
- [18] The CMS collaboration, "Performance of the CMS hadron calorimeter with cosmic ray muons and LHC beam data," *J. Instrum.* **5** (2010) T03012.
- [19] S. Abdullin *et al.*, "Design, performance, and calibration of CMS hadron-barrel calorimeter wedges," *Eur. Phys. Journal C* **55** (2008) 159–171.
- [20] S. Abdullin *et al.*, "Design, performance, and calibration of CMS forward calorimeter wedges," *Eur. Phys. Journal C* **53** (2008) 139–166.

- [21] The CMS collaboration, "Performance of muon identification in pp collisions at $\sqrt{s} = 7$ TeV," CMS Physics Analysis Summary Report No. CMS-PAS-MUO-10-002, 2010.
<http://cdsweb.cern.ch/record/1279140>.
- [22] The CMS collaboration, "Commissioning of the CMS High-Level Trigger with cosmic rays," *J. Instrum.* **5** no. 03, (2010) T03005.
- [23] R. Fruhwirth, "Application of Kalman filtering to track and vertex fitting," *Nucl. Instrum. Meth.* **A262** (1987) 444–450.
- [24] K. Rose, "Deterministic annealing for clustering, compression, classification, regression, and related optimization problems," *Proceedings of the IEEE* **86** no. 11, (1998) 2210–2239.
- [25] W. Waltenberger, R. Frühwirth, and P. Vanlaer, "Adaptive vertex fitting," *J. Phys. G* **34** no. 12, (2007) N343.
- [26] W. Adam, R. Frühwirth, A. Strandlie, and T. Todorov, "Reconstruction of electrons with the Gaussian-sum filter in the CMS tracker at the LHC," *J. Phys. G* **31** no. 9, (2005) N9.
- [27] The CMS collaboration, "Particle-Flow Event Reconstruction in CMS and Performance for Jets, Taus, and MET," CMS Physics Analysis Summary Report No. CMS-PAS-PFT-09-001, 2009.
<http://cds.cern.ch/record/1194487>.
- [28] M. Cacciari, G. P. Salam, and G. Soyez, "The anti- k_r jet clustering algorithm," *J. High Energy Phys.* **2008** no. 04, (2008) 063.
- [29] The CMS collaboration, "Commissioning of the particle-flow event reconstruction with the first LHC collisions recorded in the CMS

- detector," CMS Physics Analysis Summary Report No. CMS-PAS-PFT-10-001, 2010. <http://cds.cern.ch/record/1247373>.
- [30] The CMS collaboration, "Determination of the jet energy scale in CMS with pp collisions at $\sqrt{s} = 7$ TeV," CMS Physics Analysis Summary Report No. CMS-PAS-JME-10-010, 2010. <http://cds.cern.ch/record/1308178>.
- [31] M. Cacciari and G. P. Salam, "Pileup subtraction using jet areas," *Phys. Lett. B* **659** no. 1-2, (2008) .
- [32] The CMS collaboration, "Determination of jet energy calibration and transverse momentum resolution in CMS," *J. Instrum.* **6** no. 11, (2011) .
- [33] The CMS collaboration, "Measurement of the $t\bar{t}$ production cross section in pp collisions at 7 TeV in lepton + jets events using b -quark jet identification," *Phys. Rev. D* **84** (2011) 092004.
- [34] The CMS collaboration, "b-Jet Identification in the CMS Experiment," CMS Physics Analysis Summary Report No. CMS-PAS-BTV-11-004, 2012. <https://cdsweb.cern.ch/record/1427247>.
- [35] The CMS collaboration, "CMS Luminosity Collision Data,". <https://twiki.cern.ch/twiki/bin/view/CMSPublic/LumiPublicResults2011>. Accessed November 20, 2012.
- [36] J. Pumplin, D. R. Stump, J. Huston, H.-L. Lai, P. Nadolsky, and W.-K. Tung, "New generation of parton distributions with uncertainties from global QCD analysis," *J. High Energy Phys.* **07** (2002) 12.
- [37] P. Golonka, B. Kersevan, T. Pierzchala, E. Richter-Was, Z. Was, and M. Worek, "The tauola-photos-F environment for the TAUOLA and

- PHOTOS packages, release II," *Computer Physics Communications* **174** no. 10, (2006) 818 – 835.
- [38] S. Agostinelli *et al.*, "GEANT4—a simulation toolkit," *Nucl. Instr. and Meth. A* **506** (2003) 250.
- [39] The CMS collaboration, "Combination of top pair production cross sections in pp collisions at $\sqrt{s} = 7$ TeV and comparisons with theory," CMS Physics Analysis Summary Report No. CMS-PAS-TOP-11-001, 2011. <https://cds.cern.ch/record/1336491>.
- [40] N. Kidonakis, "Next-to-next-to-leading logarithm resummation for s -channel single top quark production," *Phys. Rev. D* **81** (2010) 054028.
- [41] N. Kidonakis, "Next-to-next-to-leading-order collinear and soft gluon corrections for t -channel single top quark production," *Phys. Rev. D* **83** (2011) 091503.
- [42] N. Kidonakis, "Two-loop soft anomalous dimensions for single top quark associated production with a W^- or H^- ," *Phys. Rev. D* **82** (2010) 054018.
- [43] The CMS collaboration, "Comparison of the fast simulation of CMS with the first LHC data," CMS Detector Performance Summary Report No. CMS-DP-2010-039, 2010. <http://cdsweb.cern.ch/record/1309890>.
- [44] The CMS collaboration, "Performance of CMS muon reconstruction in pp collision events at $\sqrt{s} = 7$ TeV," *J. Instrum.* **7** no. 10, (2012) .
- [45] The CMS collaboration, "Electron reconstruction and identification at $\sqrt{s} = 7$ TeV," CMS Physics Analysis Summary Report No.

CMS-PAS-EGM-10-004, 2010.

<http://cds.cern.ch/record/1299116>.

- [46] The CMS collaboration, "Measurement of tracking efficiency," CMS Physics Analysis Summary Report No. CMS-PAS-TRK-10-002, 2010.
<http://cds.cern.ch/record/1279139>.
- [47] J. E. Gaiser, "Charmonium Spectroscopy from Radiative Decays of the J/Ψ and Ψ -prime," PhD thesis SLAC-R-255, 1982.
- [48] The CMS collaboration, "Jet Energy Resolution in CMS at $\sqrt{s} = 7$ TeV," CMS Physics Analysis Summary Report No. CMS-PAS-JME-10-014, 2011.
<http://cds.cern.ch/record/1339945>.
- [49] D. Bourilkov, R. C. Group, and M. R. Whalley, "LHAPDF: PDF use from the Tevatron to the LHC," (2006), [arXiv:hep-ph/0605240](https://arxiv.org/abs/hep-ph/0605240).
- [50] M. Botje, J. Butterworth, A. Cooper-Sarkar, A. de Roeck, J. Feltesse, S. Forte, A. Glazov, J. Huston, R. McNulty, and T. Sjöstrand, "The PDF4LHC working group interim recommendations," (2011), [arXiv:1101.0538](https://arxiv.org/abs/1101.0538).
- [51] A. D. Martin, W. J. Stirling, R. S. Thorne, and G. Watt, "Parton Distribution Functions for the LHC," *Eur. Phys. Journal C* **63** no. 2, (2009) .
- [52] R. D. Ball, L. D. Debbio, S. Forte, A. Guffanti, J. I. Latorre, J. Rojo, and M. Ubiali, "A first unbiased global NLO determination of parton distributions and their uncertainties," *Nucl. Phys. B* **838** no. 1-2, (2010) .
- [53] The CMS collaboration, "Absolute calibration of the luminosity measurement at CMS: winter 2012 update," CMS Physics Analysis

Summary Report No. CMS-PAS-SMP-12-008, 2012.

<http://cdsweb.cern.ch/record/1434360>.

- [54] M. Evans, N. Hastings, and B. Peacock, "Statistical distributions, third edition," *Measurement Science and Technology* **12** no. 1, (2001) 117.
- [55] A. L. Read, "Presentation of search results: the CL_s technique," *J. Phys. G* **28** (2002) 2693.
- [56] G. Cowan, K. Cranmer, E. Gross, and O. Vitells, "Asymptotic formulae for likelihood-based tests of new physics," *Eur. Phys. Journal C* **71** no. 1554, (2011) .
- [57] S. S. Wilks, "The large-sample distribution of the likelihood ratio for testing composite hypotheses," *Ann. Math. Statist.* **9** no. 60-62, (1938) .
- [58] The CMS collaboration, "Anomalous HB/HE noise at startup: characteristics and rejection algorithms," CMS Internal Note Report No. CMS-IN-10-006, 2010.
- [59] The CMS collaboration, "Missing transverse energy performance of the CMS detector," *J. Instrum.* **6** no. 09, (2011) P09001.
- [60] The CMS collaboration, "Search for supersymmetry in events with b -quark jets and missing transverse energy in pp collisions at 7 TeV," *Phys. Rev. D* **86** (2012) 072010.
- [61] J. Erö *et al.*, "The CMS Drift Tube Trigger Track Finder," *J. Instrum.* **3** no. 08, (2008) P08006.
- [62] The CMS collaboration, "CMS data processing workflows during an extended cosmic ray run," *J. Instrum.* **5** no. 03, (2010) T03006.